Summer 8-15-2021

Method Development for Enhancing Sensitivity of Dynamic Nuclear Polarization Nuclear Magnetic Resonance Spectroscopy for Structural Studies of PKC-Drug Interactions

Patrick Terrence Judge
Washington University in St. Louis

WASHINGTON UNIVERSITY IN ST. LOUIS

Division of Biology and Biomedical Sciences
Biochemistry, Biophysics & Structural Biology

Dissertation Examination Committee:
Paul Schlesinger, Chair
Gaya Amarasinghe
Alexander Barnes
Gregory Bowman
Sophia Hayes

Method Development for Enhancing Sensitivity of Dynamic Nuclear Polarization Nuclear Magnetic Resonance Spectroscopy for Structural Studies of PKC-Drug Interactions

by

Patrick Terrence Judge

A dissertation presented to
The Graduate School
of Washington University in
partial fulfillment of the
requirements for the degree
of Doctor of Philosophy

August 2021
St. Louis, Missouri

Table of Contents

List of Figures

List of Tables

Acknowledgements

I would like to thank my family first and foremost: My mother, father, and Celynda, who have always been loving, encouraging, and supportive throughout this journey, and my sister who has been a consistent source of sound advice and comic relief.

I would of course like to thank Dr. Alexander Barnes for providing me the opportunity to advance my career and for facilitating my growth as a scientist. He always led by example, and even after moving to a different continent was able to dedicate valuable time to guide me through the final stages of my graduate work.

I would like to thank my colleagues for making my time in lab productive and enjoyable. Drs. Nicholas Alaniva and Edward Saliba always made the long hours in Louderman feel less like work and made the traditionally taxing aspects of research very enjoyable. Dr. Sarah Overall, while only here for a short time has provided invaluable guidance and has helped me over several hurdles at the end of my graduate work. And Dr. Erika Sesti served as a wonderful mentor in and out of lab, helping me grow not only as a scientist, but as a person as well.

I would like to thank the rest of my Thesis Committee: Dr. Gaya Amarasinghe, Dr. Gregory Bowman, Dr. Paul Schlesinger, and Dr. Sophia Hayes. Their time and effort in assisting my thesis and helping to guide the trajectory of my graduate work is greatly appreciated.

Finally, I would like to thank my fiancé, Dr. Brooke Taylor. Living with a graduate student is certainly not the easiest thing in life, but the positive effect of her love and support throughout all the highs and lows cannot be understated and is very much appreciated.

Patrick Judge

Washington University

August 2021

ABSTRACT OF THE DISSERTATION

Method Development for Enhancing Sensitivity of Dynamic Nuclear Polarization Nuclear Magnetic Resonance Spectroscopy for Structural Studies of PKC-Drug Interactions

by

Patrick Terrence Judge

Doctor of Philosophy in Biochemistry, Biophysics, & Structural Biology

Washington University in St. Louis, 2021

Paul Schlesinger, Chair

To perform the most relevant structural studies on biological systems, experiments need to be carried out when the target proteins are in their endogenous cellular environment. Nuclear magnetic resonance (NMR) is well-suited to probe the structure and dynamics of a wide variety of systems, including biologically relevant proteins. However, NMR suffers from an inherent lack of sensitivity. Dynamic nuclear polarization (DNP) NMR is a powerful technique that is used to enhance NMR sensitivity by transferring the greater polarization of exogenously doped electron spins to nuclear spins of interest though the use of a high-power microwave source. Solid effect radicals offer the advantage of being able to be decoupled from nuclear spins with current frequency-agility technology with a technique known as electron decoupling, improving the sensitivity and resolution of DNP NMR. Similarly, frequency-chirped microwaves over the polarization period are shown to enhance the sensitivity of cross effect radicals beyond that which is achievable with conventional continuous wave DNP. Both of these new techniques are shown to be applicable in biologically relevant environments such as intact human cells and cellular lysates. Improving even further upon these sensitivity enhancements will advance the experimental studies of protein kinase c-δ (PKC-δ). Molecular dynamics simulations of the C1b regulatory domain of PKC-δ complexed with various

modulators suggest protein-cholesterol interactions play an important role in differentiating the effect of two PKC modulators: phorbol 13-acetate and bryostatin-1. With improved DNP NMR sensitivity, these preliminary *in silico* results can be tested *in vivo*.

Chapter 1: Introduction

1.1 Nuclear Magnetic Resonance

Nuclear magnetic resonance (NMR) is a widely used technique with applications to the study of molecular structure and dynamics in many fields, including pharmacology, materials, and biology[1–4]. NMR relies on the manipulation and detection of nuclear spins as they interact with each other and with external magnetic fields. The external magnetic field imposes a net spin polarization, and applied magnetic fields with radio-frequency irradiation can manipulate the spins further[2,5]. Interactions of the nuclei with their chemical environment will influence how they respond to the applied RF irradiation, and thus provide information about the system.

1.2 Solid State Nuclear Magnetic Resonance

1.2.1 Magic Angle Spinning

Solution NMR utilizes natural molecular tumbling to average out anisotropic interactions between atoms to produce narrow resonances. However, samples in the solid state do not have molecular tumbling to the extent of solution samples, and thus the anisotropic interactions lead to broad resonances. To average out these anisotropic interactions in the solid state, magic angle spinning (MAS) is employed. For this technique, the samples are spun rapidly at the "magic angle" of 54.74° relative to the external magnetic field. This "magic" number is used because anisotropic terms an angular dependence proportional to $(1\text{-}3\cos^2\theta)$, where θ is the angle between the rotor axis and the external magnetic field. When $\theta = 54.74°$, this term becomes 0 and thus the anisotropic terms are averaged out[6,7]. The higher the spinning frequency, the narrower the resonances become[8–10]. While MAS does help to improve spectral resolution, NMR still suffers from a distinct lack of sensitivity[11–15].

1.2.2 Equilibrium Polarization from Boltzmann Statistics

Unfortunately, the major drawback for NMR is its inherently low sensitivity. This deficiency is brought about by the fact that the nuclear spin energy splitting in an external magnetic field are relatively small when compared to the thermal energy that is typically present[16,17]. One method for improving sensitivity is to decrease the sample temperature. The polarization of spins in a magnetic field is described by Boltzmann statistics with the following equation:

$$P = \tanh(\gamma\hbar B_0/2Tk_B)$$

Where P denotes the polarization, γ is the gyromagnetic ratio of the nucleus, $\hbar$ is the reduced Planck's constant, B_0 is the external magnetic field, T is the temperature, and k_B is Boltzmann's constant[18]. As can be seen, the polarization is inversely related to the temperature, so decreasing the temperature will increase the polarization of the nuclei, garnering more sensitivity. To put this into perspective, decreasing the temperature form 300 K (room temperature) to 6 K improves sensitivity by a factor of 42.

Along with an inverse relationship with sample temperature, the polarization is also directly related to the external magnetic field and the gyromagnetic ratio of the particles. As such, another method for increasing the polarization, and thus the resolution, is performing the experiments at a higher magnetic field. The sensitivity can also be improved by using higher γ spins. For instance, protons have a gyromagnetic ratio four times greater than carbon, so polarization from the proton spins are commonly transferred to the carbon spins via cross polarization to improve the sensitivity of ^{13}C NMR. Similarly, a mechanism for transferring polarization from electron spins, which have a gyromagnetic ration 657 times greater than protons, known as dynamic nuclear polarization (DNP) is described below[1,13,19].

1.2.3 Dynamic Nuclear Polarization

Another technique capable of overcoming this poor sensitivity is dynamic nuclear polarization (DNP). For DNP, a stable radical known as a polarizing agent is exogenously doped into the sample[12,15,20,21]. When the sample is irradiated with the correct frequency of microwaves, the strong electron-nuclear hyperfine interactions enable the transfer of the highly-polarized electron spins to the nuclear spins of interest. This polarization transfer greatly increases the sensitivity of NMR[9]. Since the electron gyromagnetic ratio is 657 times greater than that for protons, the maximum theoretical increase in sensitivity is an enhancement of 657[1,13,19].

1.2.3.1 DNP Mechanisms

Two DNP transfer mechanisms used in this dissertation are the solid effect, utilizing a "narrow-line radical", and the cross effect, using a "broad-line radical". In the solid effect, the microwave frequency is set to a "matching condition" that is one nuclear Larmor frequency (γB_0) away from the electron's resonance frequency. These microwaves then facilitate polarization transfer via a forbidden transition that causes the electron and nucleus to flip simultaneously, leading to increased nuclear polarization. The enhancement afforded by the solid effect scales with $1/B_0^2$. In the cross effect, DNP transfer is facilitated by saturating a spin packet of electrons. An electron in this spin packet will then undergo spin transitions along with one nuclear spin and an electron spin from another spin packet[1,22]. One advantage the cross effect has over the solid effect is that the enhancement it yields is predicted to only scale with $1/B_0$, and is thus more applicable at higher fields.

1.2.3.2 DNP Polarizing Agents

Different types of polarizing agents are used to optimally utilize the DNP mechanisms described above. The solid effect relies on so-called "narrow line" radicals whose EPR linewidths are narrower than the Larmor frequency of the nuclei that are intended to be polarized. One commonly

used solid effect radical is known as the trityl Finland radical[11,12,19]. This thesis also uses a newly synthesized methylated trityl radical: Trityl-Me_3N[21]. "Broad line" radicals, which have EPR linewidths greater than the nuclear Larmor frequency, are used to facilitate DNP transfer via the cross effect mechanism[11]. Cross effect radicals used in this dissertation include AMUPol, a biradical that contains two tethered nitroxide radicals, and TEMTriPol-1, which contains a nitroxide radical tethered to a trityl radical.

1.2.4 Electron Decoupling

Polarizing agents are necessary and effective for enhancing nuclear polarization via DNP. However, the strong hyperfine electron-nuclear interactions that make the transfer of polarization possible also lead to detrimental paramagnetic effects that broaden the nuclear resonances, decreasing spectral resolution[1,12,13,19]. This situation is similar to one encountered when there are ^{1}H nuclei are present. Proton decoupling methods such as continuous wave (CW) and two pulse phase modulation (TPPM) are commonly used to attenuate the strong interactions between the ^{1}H nuclei, resulting in narrower resonances and improved spectral resolution[23]. Similarly, electron decoupling can also be used to alleviate the electron-nuclear hyperfine interactions[12,19].

Electron decoupling has been shown to work on narrow-line radicals such as trityl Finland radical[1,12,19,21]. To do this, the microwave frequency is "chirped" over the electron paramagnetic resonance (EPR) linewidth of the radical, effectively decoupling the electrons from the nuclei and improving the resolution and intensity of the resonance. Here, a frequency "chirp" describes the sweeping of the microwave frequency across all or part of the ERP lineshape throughout the course of the experiment. These frequency chirps are strong enough to decouple nuclei that are in close proximity to the radical, as shown when short polarization times of just 5 ms are used on model systems[12].

1.2.5 MAS DNP NMR Spectrometer

1.2.5.1 Cryogenic System for 90 K and 6 K Experiments

A cryogenic heat exchanger is used to cool gas for drive and bearing gas lines used to spin the NMR rotor, and a variable temperature line used for regulating sample temperature using a counterflow coil system[24]. To achieve sample temperatures below 6 K, the variable temperature line is replaced by a new one that carries liquid helium, allowing the line to blow liquid helium straight on rotor. For these low temperature experiments, helium gas used for spinning[11,13,21].

1.2.5.2 Frequency-agile Gyrotron

A gyrotron is a vacuum tube that is placed in a large magnetic field. An electron gun consisting of an anode and cathode sits at the base of the gyrotron, and a large potential of around -15 kV DC is pulled cross the anode and cathode[13,19,25]. This potential pulls electrons off of the cathode, and the large external magnetic field causes the electrons to gyrate. These gyrating electrons resonate with the interaction cavity, generating microwaves. A mode converter consisting of a copper tube and mirrors converts the microwaves into a Gaussian mode. The microwaves then travel out of the window, through a corrugated waveguide, into the NMR sample.

1.3 In Cell NMR

The structure-function relationship has long been an accepted avenue for elucidating the role that biomolecules play. That is to say, determining the structure of these molecules points toward the function of that molecule in the cell. This is especially important in the area of drug discovery. Generally, structural characterization of biological molecules with NMR is performed *in vitro*[26,27]. *In vitro* NMR studies have several advantages: improved resolution through the elimination of background signals make the resulting spectra easier to interpret; it simplifies the comparison of apo and holo protein structures; the ability to use higher protein concentrations provides greater sensitivity, greatly decreasing the time required to perform experiments; and sample homogeneity

is much better compared to in cell NMR, further improving sensitivity and resolution. *In vitro* methods do come with some disadvantages, though. For example, the protein of interest must be recombinantly expressed to a high degree of purity, which is not always straightforward or possible. Due to the lack of molecular tumbling, membrane proteins are even more difficult to study, especially for larger multi-domain and multi-protein complexes. Further, *in vitro* results may ultimately be misleading due to the removal of the natural heterogeneity of membranes and of other proteins found in cells. Thus, there has been a recent push to attempt to study biomolecules in their natural environment via in-cell NMR. This is an important step, as biological processes occur in naturally complex environments that contain a wide array of potential interactors with target proteins. This is partially to validate structures previously determined in vitro, and also to explore new structures of proteins and protein/ligand complexes that have not yet been determined via any method.

There are limitations to being able to perform in cell NMR. Most notably is the need to overcome the abundance of background signal. To do so, there it is important to be able to improve the sensitivity of NMR for the desired target. In cell NMR has slowly developed improved techniques to do this over the past decade, including the labeling (uniform or specific amino acids) and overexpression of proteins in E. coli cells[28]. One clever method is the introduction of the 100% naturally abundant, bio-orthoganal ^{19}F[29,30]. Exogenous isotope labelling with these recombinant methods followed by transfer of the labelled target protein into unlabelled cells is a widely successful technique. By adding the labelled protein to an unlabelled cell, the relative sensitivity and resolution of the target protein is greatly enhanced as the percentage of labelled nuclei in the target is enhanced without increasing the percentage of the background cellular signals.

A typical technique used to deliver the labelled proteins into unlabelled cells is electroporation[31,32]. This method relieves a lot of the restrictions placed on the characteristics of the protein that is being delivered into the cells while still allowing for the advantages of introducing labelled protein into naturally abundant cells. Further developments have allowed for intracellular expression of proteins in yeast, insect, and mammalian cell lines[33–35]. Compared with previous protein delivery methods, intracellular expression enables the proteins to be studied in the cells in which they are produced without the need to exert undue stress on the cells via the delivery methods. Even with improved methods to deliver purified proteins to cells, it must be considered that added stress to the cells could affect their behavior, giving antifactual results for NMR studies performed on them.

Performing in-cell NMR becomes increasingly difficult when utilizing solid-state methods necessary for studying membrane proteins. To overcome the abundance of background cellular signals, selective labelling and overall signal enhancement techniques become vitally important. Clever labelling methods and even membrane extraction have been used to successfully study proteins in their native environments using solid-state NMR and dynamic nuclear polarization (DNP)[36–38]. Even with the added benefit of DNP, membrane proteins are still difficult to work with as their concentration is limited by a two-dimensional membrane space, and even further limited by cellular localization. Thus, even greater improvements in sensitivity are required to sufficiently enhance the NMR signal from membrane proteins. In this thesis, new DNP techniques such as electron decoupling and frequency-chirped DNP are developed and explored in intact human cells in order to improve sensitivity of the NMR signal.

1.4 Protein Kinase C-δ

Membrane proteins, including peripheral membrane proteins that dynamically interact with phospholipid bilayers, are difficult targets for structural studies[39]. Due to their association with the

membrane, there is not enough molecular tumbling to average out anisotropic interactions, negatively affecting the sensitivity of NMR experiments. Further, the local concentration of membrane proteins is limited by the available space in the membrane and by the cellular localization of the protein. One such protein, protein kinase C (PKC), plays a central role in cell signaling pathways via phosphorylation of a variety of targets involved in cell growth, differentiation, proliferation, and apoptosis[40–42]. As such, they are the targets for new therapeutic interventions of diseases such as Alzheimer's disease, cancer, and HIV/AIDS[43–46]. However, information regarding the effects of modulators on the structure and dynamics of PKC is limited, with even less information on how the drug/ligand complexes affect the immediate membrane environment surrounding them. There are three classes of PKC isoforms: conventional, novel, and atypical. Conventional PKCs require both calcium and diacylglycerol (DAG) to activate, with the C2 domain playing a major role in the initial association with the membrane. Novel PKCs, on the other hand, require only DAG, and the C1a and C1b domains are more important for membrane association. Atypical PKCs require neither calcium nor DAG, and have an overall simpler domain structure. PKC-δ, the isoform of interest in this thesis, belongs to the class of novel PKC isoforms.

1.4.1 Activation

In the first step of activation, the C2 domain of PKC translocates to the cellular membrane. In novel PKCs like PKC-δ, this domain is Ca^{2+} independent, and thus the interaction with the membrane is relatively weaker. After C2 domain translocation, the C1a and C1b domains move to the membrane, interacting with modulating ligands and, importantly, phosphatidylserine[47]. In novel PKCs, these are the primary interactions anchoring the protein to the membrane[48,49]. The dissociation of the C1 regulatory domains from the kinase domain frees the pseudosubstrate region blocking the active site of the protein on the kinase domain. This pseudosubstrate region, when no longer occluding the active site, disrupts interactions between the C1a and C2 domains[50]. PKC

isoforms will then translocate along the membrane to specialized compartments such as lipid rafts or caveolae[51]. PKC-δ specifically promotes local ceramide accumulation and drives raft fusion, which promotes cellular signaling in a nonspecific fashion[52]. To fully activate, PKC will undergo several priming phosphorylation events, followed by several autophosphorylations on the Kinase and V5 domains to lock it into a catalytically competent conformation.

1.4.2 Structural Biology Overview

1.4.2.1 C1 and C2 Domain Structure

The twin C1 domains contain a characteristic repeated zinc finger motif that is integral to the proper folding of the domain. These domains function as "hydrophobic switches" that anchor proteins to membranes. The upper third is largely hydrophobic and in generally embedded in the membrane bilayer for a stable membrane interaction. The location of ligand binding, the "binding loops", do have hydrophilic components, but these components get covered by the bound ligand, strengthening the association with the membrane. The middle third is positively charged, allowing it to form stronger interactions with negatively charged lipid headgroups, such as those present on phosphatidylserine lipids. The bottom third contains the aforementioned zinc binding residues. The binding loops contain a hydrophilic section that gets covered up through interactions with modulating ligands to stabilize their interactions in the membrane[53–55].

In novel PKCs, the C2 domain forms calcium-independent interactions with the membrane to initiate activation of the protein. Since they are calcium-independent interactions, they are generally relatively weak interactions, and thus the actions of the twin C1 domains are more important for anchoring the protein in the membrane. In fact, deletion of the C2 domain of PKC-d does not lead to any membrane targeting defects[48,49].

1.4.2.2 The Kinase Domain

Crystal structures of the kinase domains of isoforms from all three classes currently exist[56–58]. They contain a smaller NH2 lobe that consists mostly of beta sheets containing the characteristic glycine-rich ATP-binding loop with a GXGXXt sequence. There is a "gatekeeper" residue that links these two nodes, which modulates substrate accessibility to the active site[59,60]. Priming phosphorylations at serine/threonine residues are necessary to lock the enzyme in a stable, catalytically competent conformation[61–63]. These phosphorylations are followed by autophosphorylation of activation loop residues[64–67]. Novel and conventional PKCs then undergo two more phosphorylations in the V5 domain[64].

1.4.3 Modulators of PKC-δ

Two exogenous ligands that are a common subject of study with PKC-d are bryostatin and phorbol. Bryostatin is currently under clinical trials for Alzheimer's and HIV/AIDS eradication[68–70]. Currently, more tolerated and more synthetically accessible ligands are being developed, but they rely on computational ligand comparisons and models as opposed to experimental determinations of structure and dynamics of the PKC-bound complex.

Phorbol is a drug that binds to the same area of the C1b regulatory domain with the same affinity, yet is known to be a tumor promoter[42]. The reasons for these disparities in cellular responses is not yet known.

1.5 Scope of Thesis

The goal of this dissertation is to begin advancing techniques for improving DNP NMR sensitivity in intact human cells for the ultimate purpose of testing a hypothesis generated from molecular dynamics simulations on the C1b regulatory domain of PKC-δ to determine why phorbol and bryostatin elicit different cellular responses. I analyze the sensitivity of DNP radicals in the regime at cryogenic temperatures below 6 K. I also extend the electron decoupling described above to

biologically relevant systems of intact human cells and human and bacteria cell lysates. Further, I use the frequency-chips that have proven effective at decoupling electron-nuclear hyperfine interactions and employ them during the polarization period for experiments with TEMTriPol-1 to demonstrate the feasibility of performing frequency-chirped DNP on tethered biradicals to improve NMR sensitivity beyond that achievable with continuous wave cross-effect DNP. In addition, I show results from molecular dynamics simulations on the PKCd-C1b regulatory domain in order to determine how phorbol and bryostatin elicit vastly different cellular responses despite binding to the same region of the C1b domain with the same affinity.

1.6 References

1. Saliba EP, Sesti EL, Alaniva N, Barnes AB. Pulsed Electron Decoupling and Strategies for Time Domain Dynamic Nuclear Polarization with Magic Angle Spinning. *J Phys Chem Lett*. 2018;9(18):5539-5547. doi:10.1021/acs.jpclett.8b01695
2. Hayes S, Van Wüllen L, Eckert H, Even WR, Crocker RW, Zhang Z. Solid-State NMR Strategies for the Structural Investigation of Carbon-Based Anode Materials. *Chem Mater*. 1997;9(4):901-911. doi:10.1021/cm960389i
3. Yang H, Staveness D, Ryckbosch SM, et al. REDOR NMR Reveals Multiple Conformers for a Protein Kinase C Ligand in a Membrane Environment. *ACS Cent Sci*. 2018:acscentsci.7b00475. doi:10.1021/acscentsci.7b00475
4. Rossini AJ, Widdifield CM, Zagdoun A, et al. Dynamic nuclear polarization enhanced NMR spectroscopy for pharmaceutical formulations. *J Am Chem Soc*. 2014;136(6):2324-2334. doi:10.1021/ja4092038
5. Kaplan M, Narasimhan S, de Heus C, et al. EGFR Dynamics Change during Activation in Native Membranes as Revealed by NMR. *Cell*. 2016;167(5):1241-1251.e11. doi:10.1016/j.cell.2016.10.038
6. Herzfeld J, Berger AE. Sideband intensities in NMR spectra of samples spinning at the magic angle. *J Chem Phys*. 1980;73(12):6021-6030. doi:10.1063/1.440136
7. Mueller DJ. Tensors and Rotations in NMR. *Concepts Magn Reson Part A*. 2011;38(5):221-235. doi:10.1002/cmr.a
8. Andrew ER. Magic angle spinning in solid state n.m.r. spectroscopy. *Philos Trans R Soc London Ser A, Math Phys Sci*. 1981;299(1452):505-520. doi:10.1098/rsta.1981.0032
9. Stejskal EO, Schaefer J, Waugh JS. Magic-angle spinning and polarization transfer in proton-enhanced NMR. *J Magn Reson*. 1977;28(1):105-112. doi:10.1016/0022-2364(77)90260-8

10. Ernst M, Verhoeven A, Meier BH. High-Speed Magic-Angle Spinning 13C MAS NMR Spectra of Adamantane: Self-Decoupling of the Heteronuclear Scalar Interaction and Proton Spin Diffusion. *J Magn Reson*. 1998;130(2):176-185. doi:10.1006/jmre.1997.1311

11. Judge PT, Sesti EL, Saliba EP, et al. Sensitivity analysis of magic angle spinning dynamic nuclear polarization below 6 K. *J Magn Reson*. 2019;305:51-57. doi:10.1016/j.jmr.2019.05.011

12. Alaniva N, Saliba EP, Sesti EL, Judge PT, Barnes AB. Electron Decoupling with Chirped Microwave Pulses for Rapid Signal Acquisition and Electron Saturation Recovery. *Angew Chemie - Int Ed*. 2019;58(22). doi:10.1002/anie.201900139

13. Sesti EL, Saliba EP, Alaniva N, Barnes AB. Electron Decoupling with Cross Polarization and Dynamic Nuclear Polrization Below 6 K. *J Magn Reson*. 2018;295:1-5. doi:10.1016/J.JMR.2018.07.016

14. Saliba EP, Sesti EL, Scott FJ, et al. Electron Decoupling with Dynamic Nuclear Polarization in Rotating Solids. *J Am Chem Soc*. 2017;139(18). doi:10.1021/jacs.7b02714

15. Albert BJ, Gao C, Sesti EL, et al. Dynamic Nuclear Polarization Nuclear Magnetic Resonance in Human Cells Using Fluorescent Polarizing Agents. *Biochemistry*. 2018;57(31):4741-4746. doi:10.1021/acs.biochem.8b00257

16. Traficante DD. Imepedance: What It Is, and Why It Must Be Matched. *Concepts Magn Reson*. 1989;1:73-92.

17. Barnes AB, Mak-Jurkauskas ML, Matsuki Y, et al. Cryogenic sample exchange NMR probe for magic angle spinning dynamic nuclear polarization. *J Magn Reson*. 2009;198(2):261-270. doi:10.1016/j.jmr.2009.03.003

18. Carver TR, Slichter CP. Polarization of nuclear spins in metals. *Phys Rev*. 1953;92(1):212-213. doi:10.1103/PhysRev.92.212.2

19. Saliba EP, Sesti EL, Scott FJ, et al. Electron Decoupling with Dynamic Nuclear Polarization in Rotating Solids. *J Am Chem Soc*. 2017;139(18):6310-6313. doi:10.1021/jacs.7b02714

20. Judge PT, Sesti EL, Saliba EP, et al. Sensitivity analysis of magic angle spinning dynamic nuclear polarization below 6 K. *J Magn Reson*. 2019;305. doi:10.1016/j.jmr.2019.05.011

21. Judge PT, Sesti EL, Price LE, et al. Dynamic Nuclear Polarization with Electron Decoupling in Intact Human Cells and Cell Lysates. *J Phys Chem B*. 2020;124(12). doi:10.1021/acs.jpcb.9b10494

22. Barnes AB, Nanni EA, Herzfeld J, Griffin RG, Temkin RJ. A 250 GHz Gyrotron With a 3 GHz Tuning Bandwidth for Dynamic Nuclear Polarization. *J Magn Reson*. 2012;221:147-153. doi:10.1016/j.jmr.2012.03.014.A

23. Rienstra CM, Bennett AE, Griffin RG, Lakshmi K V., Auger M. Heteronuclear decoupling in rotating solids. *J Chem Phys*. 2002;103(16):6951-6958. doi:10.1063/1.470372

24. Albert BJ, Pahng SH, Alaniva N, et al. Instrumentation for cryogenic magic angle spinning dynamic nuclear polarization using 90 L of liquid nitrogen per day. *J Magn Reson*.

2017;283:71-78. doi:10.1016/j.jmr.2017.08.014

25. Scott FJ, Saliba EP, Albert BJ, et al. Frequency-agile gyrotron for electron decoupling and pulsed dynamic nuclear polarization. *J Magn Reson*. 2018;289:45-54. doi:10.1016/j.jmr.2018.02.010

26. Shcherbakov AA, Hisao G, Mandala VS, et al. Structure and dynamics of the drug-bound bacterial transporter EmrE in lipid bilayers. *Nat Commun*. 2021;12(1):1-13. doi:10.1038/s41467-020-20468-7

27. Chen H, Pan J, Gandhi DM, et al. NMR Structural Analysis of Isolated Shaker Voltage-Sensing Domain in LPPG Micelles. *Biophys J*. 2019;117(2):388-398. doi:10.1016/j.bpj.2019.06.020

28. Serber Z, Straub W, Corsini L, et al. Methyl groups as probes for proteins and complexes in in-cell NMR experiments. *J Am Chem Soc*. 2004;126(22):7119-7125. doi:10.1021/ja049977k

29. Ye Y, Liu X, Zhang Z, et al. 19F NMR spectroscopy as a probe of cytoplasmic viscosity and weak protein interactions in living cells. *Chem - A Eur J*. 2013;19(38):12705-12710. doi:10.1002/chem.201301657

30. Li C, Wang G, Wang Y, et al. Protein 19F NMR in Escherichia coli. *J Am Chem Soc*. 2013;132(1):321. doi:10.1021/ja907966n.Protein

31. Binolfi A, Limatola A, Verzini S, et al. Intracellular repair of oxidation-damaged α-synuclein fails to target C-terminal modification sites. *Nat Commun*. 2016;7:1-10. doi:10.1038/ncomms10251

32. Theillet FX, Binolfi A, Bekei B, et al. Structural disorder of monomeric α-synuclein persists in mammalian cells. *Nature*. 2016;530(7588):45-50. doi:10.1038/nature16531

33. Bertrand K, Reverdatto S, Burz DS, Zitomer R, Shekhtman A. Structure of proteins in eukaryotic compartments. *J Am Chem Soc*. 2012;134(30):12798-12806. doi:10.1021/ja304809s

34. Hamatsu J, O'Donovan D, Tanaka T, et al. High-resolution heteronuclear multidimensional NMR of proteins in living insect cells using a baculovirus protein expression system. *J Am Chem Soc*. 2013;135(5):1688-1691. doi:10.1021/ja310928u

35. Aricescu AR, Lu W, Jones EY. A time- and cost-efficient system for high-level protein production in mammalian cells. *Acta Crystallogr Sect D Biol Crystallogr*. 2006;62(10):1243-1250. doi:10.1107/S0907444906029799

36. Reckel S, Lopez JJ, Löhr F, Glaubitz C, Dötsch V. In-Cell Solid-State NMR as a Tool to Study Proteins in Large Complexes. *ChemBioChem*. 2012;13(4):534-537. doi:10.1002/cbic.201100721

37. Renault M, Boxtel RT, Bos MP, Andries J, Tommassen J, Baldus M. Cellular solid-state nuclear magnetic resonance spectroscopy. 2012;109(13):4863-4868. doi:10.1073/pnas.1116478109

38. Renault M, Pawsey S, Bos MP, et al. Solid-state NMR spectroscopy on cellular preparations enhanced by dynamic nuclear polarization. *Angew Chemie - Int Ed*. 2012;51(12):2998-3001. doi:10.1002/anie.201105984

39. Chen Y, Zhang Z, Tang X, Li J, Glaubitz C, Yang J. Conformation and topology of diacylglycerol kinase in E.coli membranes revealed by solid-state NMR spectroscopy. *Angew Chemie - Int Ed*. 2014;53(22):5624-5628. doi:10.1002/anie.201311203

40. Nishizuka Y. The role of protein kinase C in cell surface signal transduction and tumour promotion. *Nature*. 1984;308(5961):693-698. doi:10.1038/308693a0

41. Newton AC. Protein kinase C: Poised to signal. *Am J Physiol - Endocrinol Metab*. 2010;298(3). doi:10.1152/ajpendo.00477.2009

42. Thangsunan P, Tateing S, Hannongbua S, Suree N. Structural insights into the interactions of phorbol ester and bryostatin complexed with protein kinase C: a comparative molecular dynamics simulation study. *J Biomol Struct Dyn*. 2015;1102(August). doi:10.1080/07391102.2015.1084479

43. Wender PA, Kee J-M, Warrington JM. Practical Synthesis of Prostratin, DPP, and Their Analogs, Adjuvant Leads Against Latent HIV. *Science (80-)*. 2008;320(5876):649-652. doi:10.1126/science.1154690.Practical

44. DeChristopher BA, Loy BA, Marsden MD, Schrier AJ, Zack JA, Wender PA. Designed, Synthetially Accessible Bryostatin Analogues Potently Induce Activation of Latent HIV Reservoirs in vitro. *Nat Chem*. 2012;4:705-710. doi:10.1038/nchem.1395.Designed

45. Mehla R, Bivalkar-Mehla S, Zhang R, et al. Bryostatin modulates latent HIV-1 infection via PKC and AMPK signaling but inhibits acute infection in a receptor independent manner. *PLoS One*. 2010;5(6). doi:10.1371/journal.pone.0011160

46. Alkon DL, Sun MK, Nelson TJ. PKC signaling deficits: a mechanistic hypothesis for the origins of Alzheimer's disease. *Trends Pharmacol Sci*. 2007;28(2):51-60. doi:10.1016/j.tips.2006.12.002

47. Stahelin R V., Wang J, Blatner NR, Rafter JD, Murray D, Cho W. The origin of C1A-C2 interdomain interactions in protein kinase Cα. *J Biol Chem*. 2005;280(43):36452-36463. doi:10.1074/jbc.M506224200

48. Giorgione JR, Lin JH, McCammon JA, Newton AC. Increased membrane affinity of the C1 domain of protein kinase Cδ compensates for the lack of involvement of its C2 domain in membrane recruitment. *J Biol Chem*. 2006;281(3):1660-1669. doi:10.1074/jbc.M510251200

49. Stahelin R V., Digman MA, Medkova M, et al. Mechanism of diacylglycerol-induced membrane targeting and activation of protein kinase Cδ. *J Biol Chem*. 2004;279(28):29501-29512. doi:10.1074/jbc.M403191200

50. Leonard TA, Róycki B, Saidi LF, Hummer G, Hurley JH. Crystal structure and allosteric activation of protein kinase C βiI. *Cell*. 2011;144(1):55-66. doi:10.1016/j.cell.2010.12.013

51. Parton RG, Simons K. The multiple faces of caveolae. *Nat Rev Mol Cell Biol*.

2007;8(3):185-194. doi:10.1038/nrm2122

52. Zeidan YH, Hannun YA. Activation of acid sphingomyelinase by protein kinase Cδ-mediated phosphorylation. *J Biol Chem*. 2007;282(15):11549-11561. doi:10.1074/jbc.M609424200

53. Xu RX, Pawelczyk T, Xia T, et al. NMR Structure of a Protein Kinase C- γ Phorbol-Binding Domain and Study of Protein - Lipid Micelle Interactions ‡. 1997;2960(97):10709-10717.

54. Zhang G, Kazanietz MG, Blumberg PM, Hurley JH. Crystal structure of the Cys2 activator-binding domain of protein kinase Cδ in complex with phorbol ester. *Cell*. 1995;81(6):917-924. doi:10.1016/0092-8674(95)90011-X

55. Hommel U, Zurini M, Luyten M. Solution structure of a cysteine rich domain of rat protein kinase C. *Nat Struct Biol*. 1994;1(6):383-387. doi:10.1038/nsb0694-383

56. Hamaguchi A, Suzuki E, Murayama K, et al. Sphingosine-dependent Protein Kinase-1, Directed to 14-3-3, Is Identified as the Kinase Domain of Protein Kinase Cδ. *J Biol Chem*. 2003;278(42):41557-41565. doi:10.1074/jbc.M305294200

57. Grodsky N, Li Y, Bouzida D, et al. Structure of the catalytic domain of human protein kinase C β II complexed with a bisindolylmaleimide inhibitor. *Biochemistry*. 2006;45(47):13970-13981. doi:10.1021/bi061128h

58. Messerschmidt A, Macieira S, Velarde M, et al. Crystal structure of the catalytic domain of human atypical protein kinase C-iota reveals interaction mode of phosphorylation site in turn motif. *J Mol Biol*. 2005;352(4):918-931. doi:10.1016/j.jmb.2005.07.060

59. Denzel A, Hare KJ, Zhang C, et al. Cutting Edge: A Chemical Genetic System for the Analysis of Kinases Regulating T Cell Development. *J Immunol*. 2003;171(2):519-523. doi:10.4049/jimmunol.171.2.519

60. Emirick MA, Lee T, Starkey PJ, Mumby MC, Resing KA, Ahn NG. The gatekeeper residue controls autoactivation of ERK2 via a pathway of intramolecular connectivity. *Proc Natl Acad Sci U S A*. 2006;103(48):18101-18106. doi:10.1073/pnas.0608849103

61. Gonfloni S, Williams JC, Hattula K, Weijland A, Wierenga RK, Superti-Furga G. The role of the linker between the SH2 domain and catalytic domain in the regulation and function of Src. *EMBO J*. 1997;16(24):7261-7271. doi:10.1093/emboj/16.24.7261

62. Herberg FW, Zimmermann B, McGlone M, Taylor SS. Importance of the A-helix of the catalytic subunit of cAMP-dependent protein kinase for stability and for orienting subdomains at the cleft interface. *Protein Sci*. 1997;6(3):569-579. doi:10.1002/pro.5560060306

63. Stempka L, Schnölzer M, Radke S, Rincke G, Marks F, Gschwendt M. Requirements of protein kinase Cδ for catalytic function: Role of glutamic acid 500 and autophosphorylation on serine 643. *J Biol Chem*. 1999;274(13):8886-8892. doi:10.1074/jbc.274.13.8886

64. Cenni V, Döppler H, Sonnenburg ED, Maraldi N, Newton AC, Toker A. Regulation of novel protein kinase C ε by phosphorylation. *Biochem J*. 2002;363(3):537-545. doi:10.1042/0264-6021:3630537

65. Le Good JA, Ziegler WH, Parekh DB, Alessi DR, Cohen P, Parker PJ. Protein kinase C isotypes controlled by phosphoinositide 3-kinase through the protein kinase PDK1. *Science (80-).* 1998;281(5385):2042-2045. doi:10.1126/science.281.5385.2042

66. Liu Y, Graham C, Li A, Fisher RJ, Shaw S. Phosphorylation of the protein kinase C-theta activation loop and hydrophobic motif regulates its kinase activity, but only activation loop phosphorylation is critical to in vivo nuclear-factor-κB induction. *Biochem J.* 2002;361(2):255-265. doi:10.1042/bj3610255

67. Rybin VO, Guo J, Gertsberg Z, Elouardighi H, Steinberg SF. Protein Kinase Cε (PKCε) and Src control PKCδ activation loop phosphorylation in cardiomyocytes. *J Biol Chem*. 2007;282(32):23631-23638. doi:10.1074/jbc.M701676200

68. PETTIT GR, DAY JF, HARTWELL JL, WOOD HB. Antineoplastic Components of Marine Animals. *Nature*. 1970;227(5261):962-963. doi:10.1038/227962a0

69. Pettit GR, Herald CL, Doubek DL, Herald DL, Arnold E, Clardy J. Isolation and Structure of Bryostatin 1. *J Am Chem Soc*. 1982;104(24):6846-6848. doi:10.1021/ja00388a092

70. Wender PA, Hardman CT, Ho S, et al. Scalable synthesis of bryostatin 1 and analogs, adjuvant leads against latent HIV. *Science (80-).* 2017;358(6360):218-223. doi:10.1126/science.aan7969

Chapter 2: Sensitivity Analysis of MAS DNP below 6 Kelvin

Forward

This chapter is adapted from the paper "Sensitivity Analysis of Magic Angle Spinning Dynamic Nuclear Polarization below 6 Kelvin" by Patrick T. Judge, Erika L. Sesti, Edward P. Saliba, Nicholas Alaniva, Thomas Halbritter, Snorri Th. Sigurdsson, and Alexander B. Barnes and describes work that analyzes the sensitivity of solid effect and cross effect radicals below 6 K. The goal of these experiments is to determine which radicals provide the greatest sensitivity at temperatures below 6 K at 7 T while considering effects such as depolarization. An important result of this paper is demonstrating the superior sensitivity of the trityl Finland radical, a solid effect radical, at these low temperatures. However, potential advantages of the cross effect radicals, AMUPol and TEMTriPol-1, are also outlined. This knowledge will be important for the ultimate goal of implementing highly sensitive DNP NMR experiments in intact human cells. Citation: Judge, P.T., Sesti, E.L., Saliba, E.P., Alaniva, N., Halbritter, T., Sigurdsson, S.Th., Barnes, A.B. Sensitivity Analysis of Magic Angle Spinning Dynamic Nuclear Polarization below 6 K. *J. Magn. Reson.* 2019, 305, 51-57.

2.1 Overview

Dynamic nuclear polarization (DNP) improves signal-to-noise in nuclear magnetic resonance (NMR) spectroscopy. Signal-to-noise in NMR can be further improved with cryogenic sample cooling. Whereas MAS DNP is commonly performed between 25-110 Kelvin, sample temperatures below 6 K lead to further improvements in sensitivity. Here, we demonstrate that solid effect MAS DNP experiments at 6 K, using trityl, yield 3.2x more sensitivity compared to 90 K. Trityl with solid effect DNP at 6 K yields substantially more signal to noise than biradicals

and cross effect DNP. We also characterize cross effect DNP with AMUPol and TEMTriPol-1 biradicals for DNP magic angle spinning at temperatures below 6 K and 7 Tesla. DNP enhancements determined from microwave on/off intensities are 253 from AMUPol and 49 from TEMTriPol-1. The higher thermal Boltzmann polarization at 6 K compared to 298 K, combined with these enhancements, should result in 10,000x signal gain for AMUPol and 2000x gain for TEMTriPol-1. However, we show that AMUPol reduces signal in the absence of microwaves by 90% compared to 41% by TEMTriPol-1 at 7 Tesla as the result of depolarization and other detrimental paramagnetic effects. AMUPol still yields the highest signal-to-noise improvement per unit time between the cross effect radicals due to faster polarization buildup (T_{1DNP} = 4.3 s and 36 s for AMUPol and TEMTriPol-1, respectively). Overall, AMUPol results in 2.5x better sensitivity compared to TEMTriPol-1 in MAS DNP experiments performed below 6 K at 7 T. Trityl provides 6.0x more sensitivity than TEMTriPol-1 and 1.9x more than AMUPol at 6 K, thus yielding the greatest signal-to-noise per unit time among all three radicals. A DNP enhancement profile of TEMTriPol-1 recorded with a frequency-tunable, custom-built gyrotron oscillator operating at 198 GHz is also included. It is determined that at 7 T below 6 K a microwave power level of 0.6 W incident on the sample is sufficient to saturate the cross effect mechanism using TEMTriPol-1, yet increasing the power level up to 5 W results in higher improvements in DNP sensitivity with AMUPol. These results indicate MAS DNP below 6 K will play a prominent role in ultra-sensitive NMR spectroscopy in the future.

2.2 Introduction

Magic angle spinning (MAS) nuclear magnetic resonance (NMR) spectroscopy is a high-resolution technique capable of providing not only site-specific structural information in biomolecules, pharmaceuticals, and materials, but also information on the dynamics of the system relating to its function.[1–5] However, NMR is typically sensitivity limited due to a weak nuclear

spin Zeeman interaction compared to thermal energy.[6–8] Dynamic nuclear polarization (DNP) can overcome this limitation by transferring large electron spin polarization to nuclear spins of interest.[9–18] At high magnetic fields suitable for site-specific NMR resolution, this transfer is achieved with the use of high frequency microwave sources.[19–25]

The most common mechanism employed in continuous wave DNP with MAS is the cross effect[26,27]. The cross effect is active when the electron paramagnetic resonance (EPR) lineshape of the polarizing agent is dominated by inhomogeneous interactions, and the combined lineshape of all of the radicals that make up the polarizing agent is wider than the Larmor frequency of the nucleus to be polarized.[28–30] However, in the absence of microwave irradiation, level crossings at the cross effect matching conditions are still present and can depolarize nuclei, leading to signal-to-noise ratios considerably lower than the Boltzmann case seen in the absence of radical.[28,29,31,32] Therefore, the large gains in sensitivity from cross effect DNP must often be analyzed in the context of detrimental effects arising from the DNP polarizing agents. The AMUPol binitroxide radical is one of the most common polarizing agents for cross effect DNP, yet has been shown to depolarize as much as 60% under MAS at 100 K.[28,33,34]

Radicals have been developed that avoid depolarization while still allowing for the cross effect, thereby improving overall sensitivity.[29,34,35] One such radical is TEMTriPol-1, which contains a trityl radical tethered to a mononitroxide radical.[29,36] The higher symmetry of the trityl g-tensor results in less inhomogeneous broadening, and attenuates detrimental level crossing which can result in depolarization.[29] The degree of depolarization of TEMTriPol-1 has previously been characterized at 100, 110, and 125 K.[29]

MAS DNP is typically performed at temperatures near 100 K, but there is a large desire to access MAS below 25 K.[19,37,39–43] Among other benefits, DNP-NMR signal-to-noise ratios are improved

at lower temperatures due to higher Boltzmann polarization of the electron spins and longer electron spin relaxation resulting in more efficient DNP transfers.[41,42]

Here, we investigate the behavior of DNP radicals including trityl, TEMTriPol-1 and AMUPol at temperatures below 6 K and at a magnetic field of 7 T. We characterize the sensitivity with respect to signal-to-noise per unit time. For cross effect DNP, we also measure the nuclear longitudinal relaxation times (T_1), polarization build-up times (T_{1DNP}), maximum enhancements, and depolarization effects. The DNP enhancement profile of TEMTriPol-1 is also recorded with MAS at 90 K, as is the microwave power dependence of biradicals with MAS at 6 K and 90 K.

2.3 Methods

2.3.1 Sample Preparation

Samples were prepared with 4M [U-^{13}C,^{15}N] urea (Cambridge Isotope Laboratories, Tewksbury, MA) and 5 mM radical AMUPol (Cortecnet, Voisins-le-Bretonneux, France), 5 mM TEMTriPol-1, or 40 mM Trityl Finland radical (Oxford Instruments, Abingdon, UK) in a d_8-glycerol/D_2O/H_2O mixture at a 60/30/10 volume ratio. An identical radical-free sample was also prepared. Once mixed, approximately 36 μL of each sample was packed into 3.2 mm zirconia rotors, and spun in a custom-built MAS DNP spectrometer.[22,38,44]

2.3.2 MAS DNP NMR Spectroscopy

Electron polarization from biradicals was transferred to nearby protons via the cross effect using continuous wave (CW) microwave irradiation, and the bulk protons were polarized via spin diffusion.[16] The microwave irradiation frequency was 197.670 GHz for TEMTriPol-1, 197.674 GHz for AMUPol, and 197.719 GHz for the Trityl Finland radical. Polarization transfer with cross polarization (CP) was achieved with $\omega_{1H}/2\pi$ = 50 kHz, $\omega_{13C}/2\pi$ = 52 kHz, and a Hartmann-Hahn contact time of 1 ms. The ^{1}H Larmor frequency was 300.179 MHz, and the ^{13}C Larmor frequency was 75.4937 MHz at a B_0 = 7.05 T. All data were recorded with a custom-built, four-channel, 3.2

mm, transmission line MAS-NMR probe using a Redstone spectrometer (Tecmag Inc., Houston, TX).[44] Rotor-synchronized, echo-detected, CPMAS sequences were used to record all data. A nutation of $\omega_{1H}/2\pi$ = 90 kHz was used for $\pi/2$ pulses and TPPM decoupling on ^{1}H.[48] A nutation of $\omega_{13C}/2\pi$ = 100 kHz was used for the ^{13}C refocusing pulse to generate Hahn echoes. Magnetization was saturated with a train of pulses on both ^{1}H and ^{13}C prior to the DNP polarization time (τ_{pol}). The τ_{pol} was 3 s to measure the enhancement profile of TEMTriPol-1. The τ_{pol} for all other experiments was 1.26*T_{1DNP}. A saturation recovery sequence was used to measure the longitudinal nuclear relaxation times with no microwave irradiation (T_1), and also polarization build-up times with microwave irradiation (T_{1DNP}). Spinning frequencies were between 5600 and 5800 Hz with ± 40 Hz stability, and exact details of spinning are described in respective figure captions. Microwave irradiation generated from a custom-built 198 GHz gyrotron was coupled to the sample using corrugated waveguides, tapers, and mirrors[22,44]. The gyrotron output was 40 W, with approximately 7 W incident on the sample[22,23,44].

Enhancements were determined by taking the ratio of signal intensities recorded with microwave irradiation and without microwave irradiation, taking into account scaling required by the number of scans used for each experiment. DMFit was used to fit the peaks and determine the areas and intensites.[45] For power dependence measurements, the microwave power was varied with attenuators placed within the waveguide (Tydex LLC, St. Petersburg, Russia), and microwave power was measured using a custom-built water calorimeter.

To achieve sample temperatures below 6 K, liquid helium was used as a variable temperature (VT) fluid directed at the center of the spinning zirconia rotor.[37] Ultra-high purity helium gas at 80 K was used for bearing and drive. The sample temperature was monitored at the interface of the VT outlet and NMR stator with a calibrated Cernox temperature sensor (Lake Shore Cryotronics, Inc.,

Westerville, OH). This temperature represents the sample temperature as previously described.[13] A Lake Shore temperature controller was used to monitor the temperature of the sample, incoming transfer lines, and exhaust line.

2.4 Results and Discussion

2.4.1 TEMTriPol-1 Enhancement Profile

To determine the microwave frequency for maximal enhancement with TEMTriPol-1, CPMAS experiments were performed at varying gyrotron frequencies to record the ^{1}H Zeeman enhancement profile of the biradical (**Fig. 1a**). For these experiments, a polarization time of 3 s was used, even though it is significantly shorter than the optimal polarization time shown in **Fig. S3b**. At 90 K, 5 mM TEMTriPol-1 yielded a maximum positive enhancement of 76 at a gyrotron frequency of 197.670 GHz with a polarization time of 3 s (**Fig. 1b**). This profile is similar to that reported previously.[29,36]

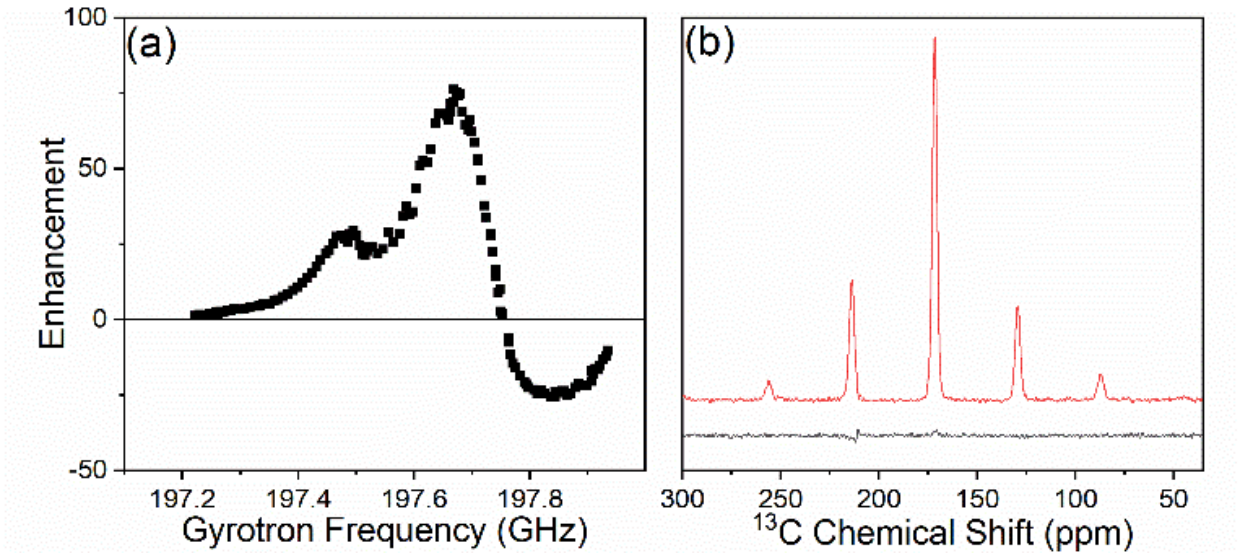

Figure 1. (a) ^{1}H Zeeman enhancement profile of TEMTriPol-1 at varying gyrotron frequencies. **(b)** DNP-enhanced CPMAS spectrum at 90 K of 4 M [U-^{13}C,^{15}N] urea with TEMTriPol-1 at 5 mM, ν_{rot} = 3,200 Hz. Black represents no DNP, red is with DNP at $\nu_{gyrotron}$ = 197.670 GHz.

2.4.2 Sensitivity of Trityl at 6 K

To put in perspective the increase in sensitivity at 6 K compared to more conventional temperatures around 90 K, the sensitivity of cross polarization experiments at both temperatures was compared using the solid effect. **Fig. 2** shows spectra of 4 M [U-^{13}C,^{15}N] urea with 40 mM trityl. The polarization time for each experiment was chosen to be 1.26*T_{1DNP} at their respective temperatures. Since the ^{1}H T_{1DNP} at 90 K was half as long as at 6 K, the number of scans taken at 90 K was doubled to keep the total experimental time the same for both experiments. As can be seen in **Fig. 2**, the spectrum recorded below 6 K shows much improved signal to noise. The intensity of the ^{13}C Urea resonance is 3.2x larger, indicating a significant improvement to NMR sensitivity available at cryogenic temperatures below 6 K by a factor of 3.2x compared to 90 K.

As discussed below, AMUPol and TEMTriPol-1 affect the sample through depolarization and other deleterious effects, such as paramagnetic relaxation. Note that while TEMTriPol-1 has been shown to not depolarize the sample at temperatures near 100 K, this is not necessarily the case below 6 K, as we will show in the following sections. Trityl is a narrow-line monoradical that does not meet the cross effect condition and thus does not cause depolarization. However, other detrimental effects such as paramagnetic relaxation can remain.

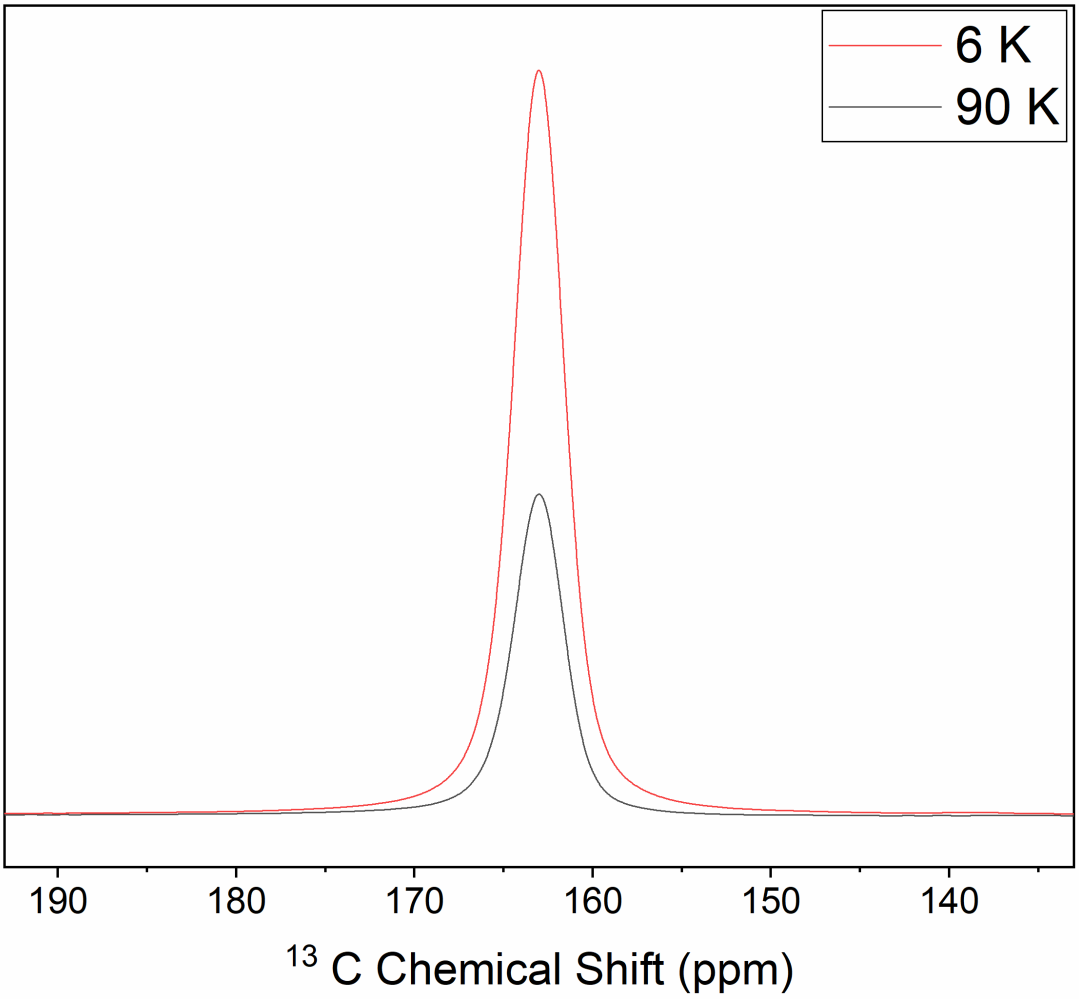

Figure 2. Comparison of the sensitivity of CPMAS experiments on 4 M [U-^{13}C,^{15}N] urea with 40 mM trityl at 90 K (black) and 6 K (red). The total experimental time to acquire both spectra were the same.

2.4.3 Power Dependence Comparison

CPMAS experiments with varying microwave transmission through the waveguide were performed below 6 K to determine dependence of the maximum ^{1}H signal enhancements for TEMTriPol-1 and AMUPol on the incident microwave power (**Fig. 3**). Attenuators were inserted into a 9 mm gap in the middle of the corrugated waveguide to modulate the microwave power on the sample. The microwave power on each sample without any attenuators was estimated to be 7

W at a microwave frequency of 197.670 GHz, resulting in an average electron Rabi frequency of 0.45 MHz.[22,23] Lower microwave powers result in lower cross effect DNP enhancement if on-resonance electron spins are not fully saturated.[46,47] The cross effect becomes saturated at about 0.6 W of microwave power using 5 mM TEMTriPol-1 (**Fig. 3a**). However, in the case of 5 mM AMUPol, increasing microwave power continues to increase NMR signal intensity up to about 5 W of microwave power (**Fig. 3b**). Therefore, we demonstrate that lower microwave sources are fully suitable for cross effect DNP from biradicals containing a slowly relaxing narrow-line radical, yet gyrotron sources capable of producing >10 W are advantageous for bi-nitroxide polarizing agents. We observe similar power dependencies at 90 K for both radicals. The cross effect saturates at higher powers for both radicals at 90 K, but TEMTriPol-1 still saturates at a significantly lower power compared to AMUPol at 90 K.

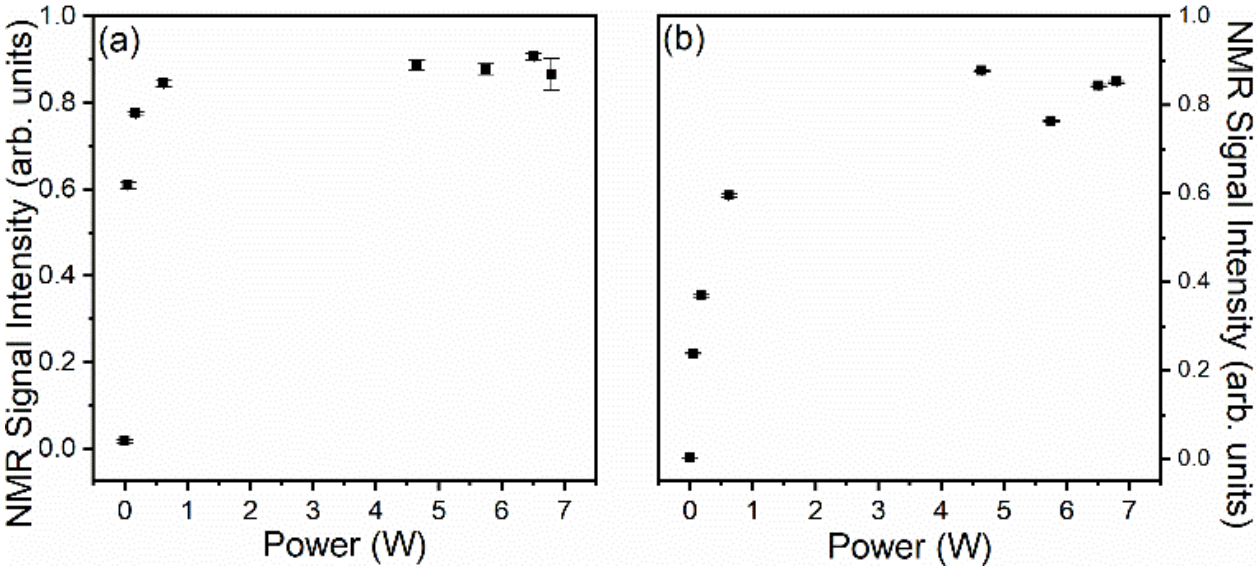

Figure 3. Area of the [U-^{13}C,^{15}N] urea ^{13}C resonance dependence on relative microwave power below 6 K for **(a)** TEMTriPol-1 and **(b)** AMUPol.

2.4.4 Signal-to-Noise and Sensitivity

As described by De Paëpe and colleagues, the signal-to-noise per unit time is the true measure of sensitivity, and depends on many parameters besides DNP enhancement including, but not limited to; temperature, experimental repetition time, noise figures, and signal attenuation due to the presence of radicals.[28,29,34,49,50] Note that, when comparing the sensitivity between two experiments that are not taken over the same amount of time, it is necessary to consider the square root of the polarization time. As such, in our comparison between AMUPol and TEMTriPol-1 in this paper we consider the square root of the polarization time when comparing the sensitivity of both radicals below 6 K. The signal-to-noise per unit time provided by 5 mM AMUPol (**Fig. 4a**) and 5 mM TEMTriPol-1 (**Fig. 4e**) were compared from CPMAS experiments below 6 K (**Fig. 4**). With an incident microwave power of 7 W, 5 mM AMUPol provided an enhancement of 253 at 5.1 K (**Fig. 4b**). 5 mM TEMTriPol-1 provided a smaller enhancement of 49 at 4.2 K (**Fig. 4f**). DNP polarization periods of $1.26*T_{1DNP}$ were used for each radical.

It is important to note that the signal enhancement with TEMTriPol-1 has been shown here to be greater at 90 K than at 6 K. An explanation for the different behavior of the cross effect for different biradicals is that it is dependent on electronic relaxation times.[33] It was demonstrated by Vega and colleagues that at temperatures below 30 K the cross effect starts to become much less efficient.[51] Neither AMUPol nor TEMTriPol-1 were designed for use at such low temperatures and, as such, their performance at 6 K do not mimic the improvement in sensitivity seen with trityl (**Fig. 2**).

While the enhancements from AMUPol were significantly larger than TEMTriPol-1, AMUPol reduces the signal obtained from the nuclear spins in the absence of microwaves more substantially than TEMTriPol-1 due to a combination depolarization and other detrimental effects such as paramagnetic relaxation. The extent of the depolarization of AMUPol has been partially attributed to its longer T_{1e} relaxation times compared to other, non-depolarizing radicals.[29,33] In the case of

narrow-line monoradicals such as trityl, these paramagnetic relaxation effects can be mitigated with electron decoupling.[24,41] However, biradicals with extensive inhomogenous broadening will require much higher electron spin Rabi frequencies to implement electron decoupling.

CPMAS experiments were performed in the absence of microwaves below 6 K at 7 T to determine the extent to which the signal was reduced by 5 mM AMUPol compared to 5 mM TEMTriPol-1, which has been shown to not depolarize at 100 K. Urea with 5 mM AMUPol results in only 10% of the intensity compared to urea without radical (**Fig. 4c**). Markedly, 5 mM TEMTriPol-1 reduces signal to a lesser extent, at 59% of the intensity compared to urea without radical (**Fig. 4g**). Substituting the radical-present microwave-off signal with its no-radical counterpart, the "adjusted enhancements" were 25 for 5 mM AMUPol and 29 for 5 mM TEMTriPol-1 at an incident microwave power of 7 W.[28]

While the adjusted enhancements obtained with 5 mM TEMTriPol-1 and 5 mM AMUPol were more similar in magnitude, the ^{1}H T_1 polarization buildup times (T_{1DNP}) were significantly different. The T_{1DNP} plots for ^{1}H below 6 K are shown in **Fig. 4d,h**. Urea with 5 mM AMUPol had a short T_{1DNP} time of 4.3 ± 0.1 s (**Fig. 4d**). In contrast, 5 mM TEMTriPol-1 exhibited a much longer T_{1DNP} time of 36.2 ± 1.1 s (**Fig. 4h**). Thus, the polarization time required to achieve the maximum enhancement with AMUPol was about 9-times shorter than for TEMTriPol-1. This shorter T_{1DNP} allows AMUPol to provide superior signal-to-noise per unit time. To compare the sensitivity for each radical, the adjusted enhancement was divided by the square root of the corresponding T_{1DNP}. The sensitivity for AMUPol was calculated to be 2.5 times larger than for TEMTriPol-1.

A similar comparison using the signal-to-noise divided by the square root of the polarization time for each radical is shown in **Table 1**. For reference, dividing the signal-to-noise by the square root

of the polarization time shows that AMUPol provides 3.1x more signal-to-noise per unit square root time than TEMTriPol-1 at 6 K. At 90 K, AMUPol provides the greatest sensitivity, yielding 1.4x more signal-to-noise per unit square root time than trityl, and 1.7x more than TEMTriPol-1. However, at 6 K trityl yields 1.9x more signal-to-noise per unite square root time than AMUPol, and 6.0x more than TEMTriPol-1 at 7 T. Thus, at 90 K, AMUPol with the cross effect is preferential for obtaining the greatest sensitivity, while at 6 K, trityl is preferable for more sensitive experiments with the solid effect.

The sensitivity comparison between 90 K and 6 K performed on trityl in section 4 can also be made for the cross effect radicals discussed here. To do so, we compared the signal-to-noise produced by both radicals at each temperature divided by the square root of their respective polarization times (**Table 1**). Surprisingly, neither AMUPol nor TEMTriPol-1 displayed a significant increase in sensitivity when the sample temperature was reduced to 6 K, with TEMTriPol-1 actually decreasing in sensitivity. AMUPol's signal-to-noise per unit time increased by a factor of only 1.2x, while TEMTriPol-1's sensitivity is only 0.6x compared to 90 K. This is in stark contrast to trityl, which increased in sensitivity by 3.2x. As mentioned previously, it has already been observed that the cross effect is less efficient at temperatures below 30 K;[51] this decrease in efficiency may be preventing the increase in sensitivity for AMUPol and TEMTriPol-1 that was observed for trityl.

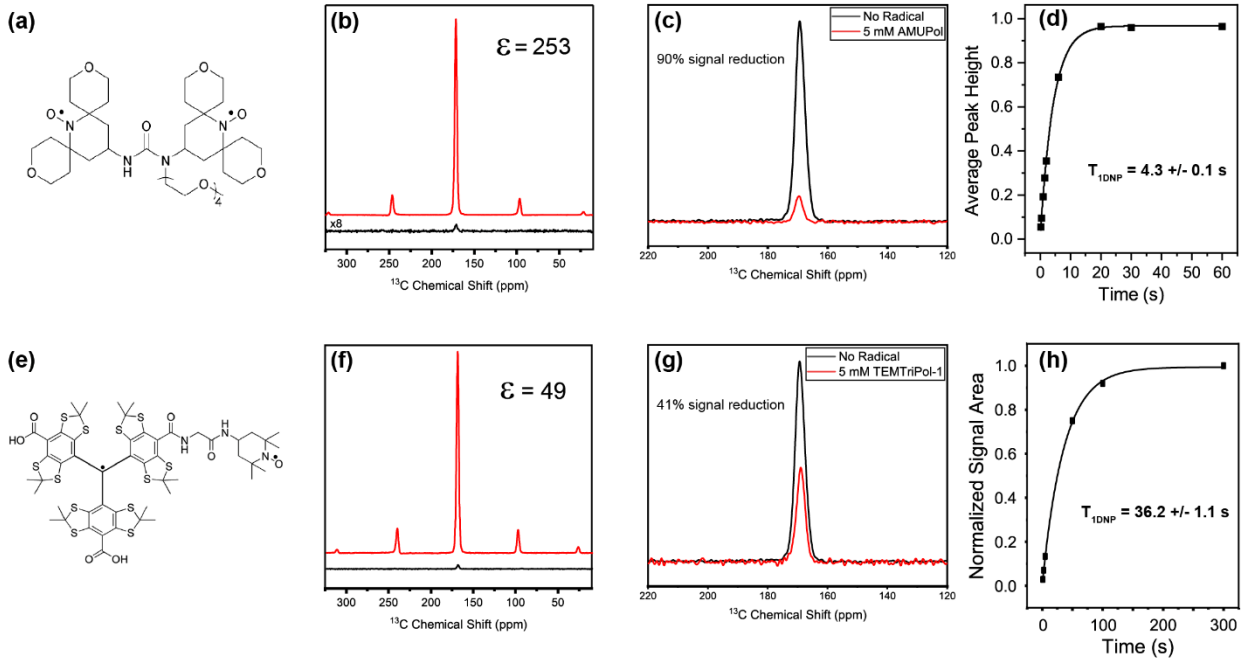

Figure 4. Structures of AMUPol **(a)** and TEMTriPol-1 **(e)** and their corresponding DNP CPMAS spectra of 4 M [U-^{13}C,^{15}N] urea with 5 mM AMUPol (ν_{rot} = 5,700 Hz) **(b)** and 5 mM TEMTriPol-1 (ν_{rot} = 5,700 Hz) **(f)**, with the DNP signal in red and the no DNP signal in black. **(c)** and **(g)** show the signal reduction of the sample caused by the addition of 5 mM AMUPol and TEMTriPol-1, respectively, with the urea signal with no radical in black and the urea signal with radical in red (ν_{rot} = 5,700 Hz). **(d)** and **(h)** show the ^{1}H T_{1DNP} polarization buildup times for AMUPol and TEMTriPol-1, respectively. All data was recorded at a microwave power of 7 W below 6 K.

Radical (Mechanism)	**90 K S/N/sqrt(τ_{pol})**	**6 K S/N/sqrt(τ_{pol})**
AMUPol (CE)	222	261
TEMTriPol-1 (CE)	134	84

Trityl (SE)	156	506

Table 1. Sensitivity comparison of AMUPol, TEMTriPol-1, and trityl at 90 K and 6 K. Columns show the signal-to-noise divided by the square root of the polarization buildup time.

To determine whether the relationship between ^{1}H relaxation times remains the same in the absence of microwaves, we compared the ^{1}H T_1 (without microwaves) of [U-^{13}C,^{15}N] urea with AMUPol and TEMTriPol-1 (**Fig. 5**). It was determined that the ^{1}H T_1 with AMUPol was 9.4 ± 0.7 s (**Fig. 5a**), which is 9 times shorter than the 83.7 ± 3.0 s T_1 we determined for TEMTriPol-1 (**Fig. 5b**). It is noteworthy that the ^{1}H T_1 and the ^{1}H T_{1DNP} times are not equal for either biradical used, which is not typically observed for biradicals and cross effect DNP. The disparity in T_1 and T_{1DNP} indicates that DNP mechanisms at 6 K and 90 K are not identical.[33] This could be partially due to the difference in electron polarization at 6 K compared to 90 K. The increased polarization at 6 K makes electron-electron pairs with opposite spin orientation to participate in the cross effect less common.[56]

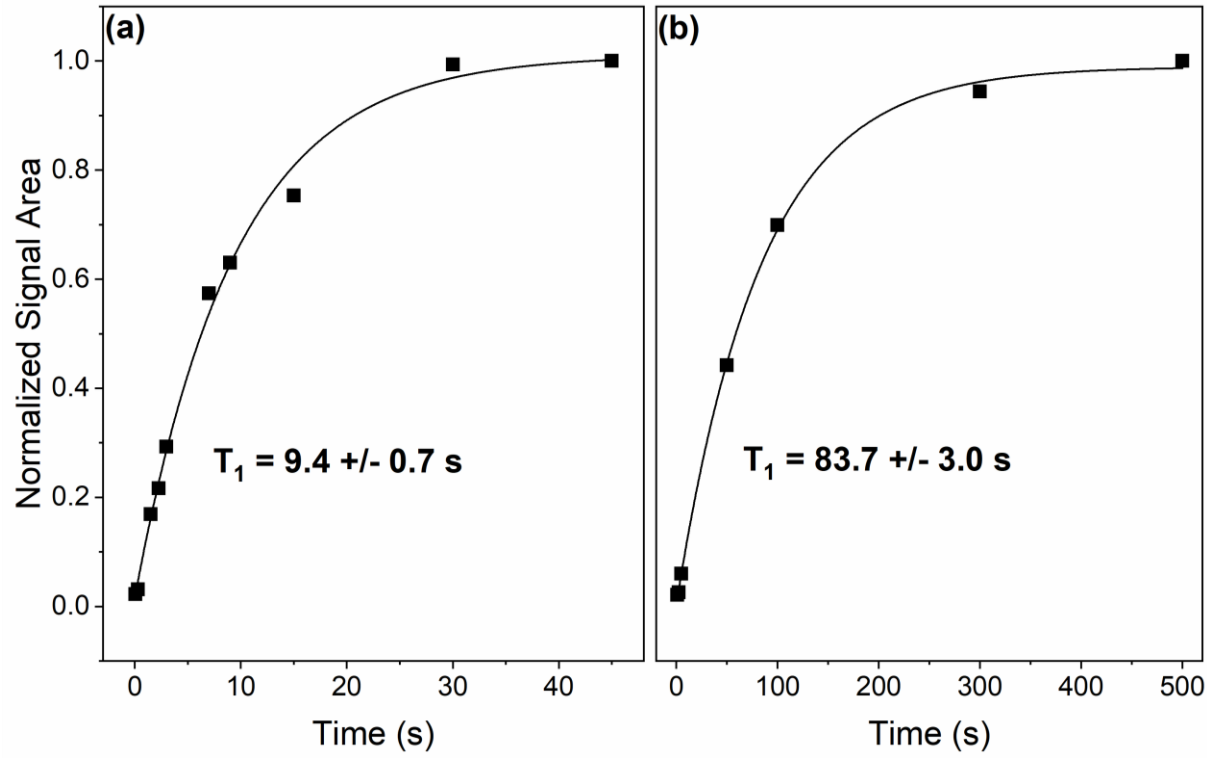

Figure 5. ^{1}H T_1 of [U-^{13}C,^{15}N] urea with **(a)** 5 mM AMUPol and **(b)** 5 mM TEMTriPol-1.

2.5 Conclusions and Outlook

Here, we definitively demonstrate that solid effect DNP is more sensitive below 6 K than at 90 K by performing CPMAS experiments with trityl. The sensitivity at 6 K was determined to be 3.2x greater than at 90 K. We also show that AMUPol offers significant advantages over TEMTriPol-1 for quickly obtaining improved signal-to-noise below 6 K at 7 T. While AMUPol greatly depolarizes nuclear spins, the adjusted enhancement was still of similar magnitude to that of TEMTriPol-1. Furthermore, the polarization time required to achieve these enhancements drastically favored AMUPol, which required only one ninth the time to provide its maximum enhancement. The shorter T_{1DNP} effectively enables AMUPol to provide 2.5 times more signal-to-noise per unit time. While AMUPol exhibited these clear advantages between the two cross effect radicals, TEMTriPol-1 may still offer its own distinct advantages below 6 K at 7 T. For instance, a chelated gadolinium moiety could be covalently attached to trityl-nitroxide radicals to achieve

shorter electron spin relaxation properties.[57] Furthermore, electron decoupling of trityl within TEMTriPol-1 could also mitigate detrimental effects due to the strong hyperfine interactions.[24,41] We have already shown electron decoupling with a trityl radical has the ability to improve the signal intensity while decreasing the linewidth of the signal at temperatures below 6 K.[41] Furthermore, this sensitivity comparison may not scale up to larger magnetic fields (> 18 T), where TEMTriPol-1 is known to provide more efficient DNP transfer than at 7 T.[29,36]

Trityl yielded the highest sensitivity between all three radicals studied. Using the solid effect, trityl yielded 1.9x and 6.0x more signal-to-noise per unit square root time than the cross effect radicals AMUPol and TEMTriPol-1, respectively, at 6 K and 7 T. Furthermore, we demonstrated that at 6 K the cross effect is saturated at about 5 W of microwave power with 5 mM AMUPol, and at 0.6 W with 5 mM TEMTriPol-1. Since trityl uses the solid effect as its primary DNP mechanism, we do not expect DNP enhancements to diminish with stronger microwave fields, opening the possibility for even greater sensitivity at 6 K with greater microwaves powers. Greater microwave powers will also open the possibility of pulsed DNP for coherent manipulation of electron spins, especially with a narrow-line radical such as trityl. We have successfully performed electron decoupling on trityl below 6 K.[41] We have also demonstrated that we can successfully decouple the hyperfine interactions between the electron spins and nuclear spins in close proximity to the radical.[58] One advantage that TEMTriPol-1 has over trityl, though, is that the solid effect is less effective at fields for which TEMTriPol-1 is optimized (> 18 T). This opens the possibility that TEMTriPol-1, or other cross effect radicals designed for operation at high magnetic fields, will yield greater sensitivity at 90 K and/or 6 K.

The overall signal enhancement of 1000x we have demonstrated using MAS DNP < 6 K will benefit structural biology and characterization of materials. For example, determining distance

constraints on biochemical structures involves multiple evolution dimensions, leading to currently lengthy experimental times.[51–55] Maximizing the signal-to-noise ratio obtained in an NMR experiment by achieving the largest possible electron Boltzmann polarization, as well as optimizing the efficiency of DNP transfers, allows these experiments to be performed in a fraction of the time required otherwise.

Aside from its *in vitro* applications, AMUPol has also been shown to be effective for enhancing NMR signals in an *in vivo* environment of HEK293-F cells.[42] In-cell DNP experiments will be critical for elucidating the structure-function relationship of many biological systems in their native cellular environment. Maximizing the signal-to-noise of the sparsely-populated NMR spins in these cellular samples through DNP and through cooling the system down to cryogenic temperatures below 6 K will be necessary for such experiments.

There are two distinct routes for improving the MAS DNP-NMR below 6 K. One is to use new radicals for continuous wave DNP transfers that are designed to have optimal relaxation properties. However, we believe continuous wave DNP will evolve into the pulsed regime, as microwave technology is developed and becomes widely available. A second route to ultra-sensitive NMR below 6 K is therefore the application of pulsed microwaves for time-domain transfer mechanisms, followed by pulsed electron decoupling. Therefore, we will develop new instrumentation to implement intense chirped microwave pulses for MAS.

2.6 Acknowledgements

This research was supported by the NIH (DP2-GM119131), NSF-IDBR (CAREER DBI-1553577), the Camille Dreyfus Teacher-Scholar Awards Program, the Deutsche Forschungsgemeinschaft (DFG) postdoc fellowship (414196920), and the University of Iceland Research Fund. We thank Brice Albert, Faith Scott, Chukun Gao, and Natalie Golota for assistance building instrumentation.

Author Contributions:

- Design and planning of experiments was a collaboration between Patrick Judge, Erika Sesti, Edward Saliba, Nicholas Alaniva, and Alexander Barnes
- Experiments and analysis were carried out predominately by Patrick Judge
- TEMTriPol-1 synthesis was performed by Thomas Halbritter and Snorri Sigurdsson
- Manuscript was written and compiled predominately as a collaboration between Patrick Judge and Alexander Barnes

2.7 References

1. T. Polenova, R. Gupta and A. Goldbourt, Magic angle spinning NMR spectroscopy: A versatile technique for structural and dynamic analysis of solid-phase systems, *Anal. Chem.*, 2015, **87**, 5458–5469.

2. A. J. Rossini, C. M. Widdifield, A. Zagdoun, M. Lelli, M. Schwarzwälder, C. Copéret, A. Lesage and L. Emsley, Dynamic nuclear polarization enhanced NMR spectroscopy for pharmaceutical formulations, *J. Am. Chem. Soc.*, 2014, **136**, 2324–2334.

3. M. Kaplan, S. Narasimhan, C. de Heus, D. Mance, S. van Doorn, K. Houben, D. Popov-Čeleketić, R. Damman, E. A. Katrukha, P. Jain, W. J. C. Geerts, A. J. R. Heck, G. E. Folkers, L. C. Kapitein, S. Lemeer, P. M. P. van Bergen en Henegouwen and M. Baldus, EGFR Dynamics Change during Activation in Native Membranes as Revealed by NMR, *Cell*, 2016, **167**, 1241–1251.e11.

4. S. Hayes, L. Van Wüllen, H. Eckert, W. R. Even, R. W. Crocker and Z. Zhang, Solid-State NMR Strategies for the Structural Investigation of Carbon-Based Anode Materials, *Chem. Mater.*, 1997, **9**, 901–911.

5. M. L. Mak-Jurkauskas, V. S. Bajaj, M. K. Hornstein, M. Belenky, R. G. Griffin and J. Herzfeld, Energy transformations early in the bacteriorhodopsin photocycle revealed by DNP-enhanced solid-state NMR, *Proc. Natl. Acad. Sci.*, 2008, **105**, 883–888.

6. A. S. L. Thankamony, J. J. Wittmann, M. Kaushik and B. Corzilius, Dynamic nuclear polarization for sensitivity enhancement in modern solid-state NMR, *Prog. Nucl. Magn. Reson. Spectrosc.*, 2017, 120–195.

7. M.W.Dale and C.J. Wedge, Optically generated hyperpolarization for sensitivity enhancement in solution-state NMR spectroscopy, *Chem. Commun.*, 2016, **52**, 13221-13224.

8. E. P. Saliba, E. L. Sesti, N. Alaniva and A. B. Barnes, Pulsed Electron Decoupling and Strategies for Time Domain Dynamic Nuclear Polarization with Magic Angle Spinning, *J. Phys. Chem. Lett.*, 2018, **9**, 5539–5547.

9. T. Maly, G. T. Debelouchina, V. S. Bajaj, K.-N. Hu, C.-G. Joo, M. L. Mak–Jurkauskas, J. R. Sirigiri, P. C. A. van der Wel, J. Herzfeld, R. J. Temkin and R. G. Griffin, Dynamic nuclear polarization at high magnetic fields, *J. Chem. Phys.*, 2008, **128**, 052211.

10. A. B. Barnes, E. A. Nanni, J. Herzfeld, R. G. Griffin and R. J. Temkin, A 250 GHz Gyrotron With a 3 GHz Tuning Bandwidth for Dynamic Nuclear Polarization, *J. Magn. Reson.*, 2012, **221**, 147–153.

11. K. R. Thurber, W. M. Yau and R. Tycko, Low-temperature dynamic nuclear polarization at 9.4 T with a 30 mW microwave source, *J. Magn. Reson.*, 2010, **204**, 303–313.

12. A. N. Smith, M. A. Caporini, G. E. Fanucci and J. R. Long, A method for dynamic nuclear polarization enhancement of membrane proteins, *Angew. Chem. Int. Ed.*, 2015, **54**, 1542–1546.

13. J. M. Franck, A. Pavlova, J. A. Scott and S. Han, Quantitative cw Overhauser effect dynamic nuclear polarization for the analysis of local water dynamics, *Prog. Nucl. Magn. Reson. Spectrosc.*, 2014, **74**, 33–56.

14. A. Leavesley, C. B. Wilson, M. Sherwin and S. Han, Effect of water/glycerol polymorphism on dynamic nuclear polarization, *Phys. Chem. Chem. Phys.*, 2018, **20**, 9897–9903.

15. A. Equbal, Y. Li, A. Leavesley, S. Huang, S. Rajca, A. Rajca and S. Han, Truncated Cross Effect Dynamic Nuclear Polarization: An Overhauser Effect Doppelgänger, *J. Phys. Chem. Lett.*, 2018, **9**, 2175–2180.

16. L. R. Becerra, G. J. Gerfen, R. J. Temkin, D. J. Singel and R. G. Griffin, Dynamic nuclear polarization with a cyclotron resonance maser at 5 T, *Phys. Rev. Lett.*, 1993, **71**, 3561–3564.

17. D. A. Hall, D. C. Maus, G. J. Gerfen, S. J. Inati, L. R. Becerra, F. W. Dahlquist and R. G. Griffin, Polarization-Enhanced NMR Spectroscopy of Biomolecules in Frozen Solution, *Science.*, 1997, **276**, 930–932.

18. A. W. Overhauser, Polarization of Nuclei in Metals, *Phys. Rev.*, 1953, **92**, 411–415.

19. Y. Matsuki, T. Idehara, J. Fukazawa and T. Fujiwara, Advanced instrumentation for DNP-enhanced MAS NMR for higher magnetic fields and lower temperatures, *J. Magn. Reson.*, 2016, **264**, 107–115.

20. Y. Matsuki, H. Takahashi, K. Ueda, T. Idehara, I. Ogawa, M. Toda, H. Akutsu and T. Fujiwara, Dynamic nuclear polarization experiments at 14.1 T for solid-state NMR, *Phys. Chem. Chem. Phys.*, 2010, **12**, 5799–5803.

21. A. B. Barnes, E. Markhasin, E. Daviso, V. K. Michaelis, E. A. Nanni, S. Jawla, E. L. Mena, R. DeRocher, A. Thakkar, P. Woskov, J. Herzfeld, R. J. Temkin and R. G. Griffin, Dynamic Nuclear Polarization at 700 MHz/460 GHz, *J. Magn. Reson.*, 2012, **224**, 1–7.

22. F. J. Scott, E. P. Saliba, B. J. Albert, N. Alaniva, E. L. Sesti, C. Gao, N. C. Golota, E. J. Choi, A. P. Jagtap, J. J. Wittmann, M. Eckardt, W. Harneit, B. Corzilius, S. Th. Sigurdsson and A. B. Barnes, Frequency-agile gyrotron for electron decoupling and pulsed dynamic nuclear polarization, *J. Magn. Reson.*, 2018, **289**, 45–54.

23. D. E. M. Hoff, B. J. Albert, E. P. Saliba, F. J. Scott, E. J. Choi, M. Mardini and A. B. Barnes, Frequency swept microwaves for hyperfine decoupling and time domain dynamic nuclear polarization, *Solid State Nucl. Magn. Reson.*, 2015, **72**, 79–89.

24. E. P. Saliba, E. L. Sesti, F. J. Scott, B. J. Albert, E. J. Choi, N. Alaniva, C. Gao and A. B. Barnes, Electron Decoupling with Dynamic Nuclear Polarization in Rotating Solids, *J. Am. Chem. Soc.*, **139**, 6310-6313.

25. S. Alberti, F. Braunmueller, T. M. Tran, J. Genoud, J. P. Hogge, M. Q. Tran and J. P. Ansermet, Nanosecond pulses in a THz gyrotron oscillator operating in a mode-locked self-consistent q-switch regime, *Phys. Rev. Lett.*, 2013, **111**, 205101.

26. D.S. Wollan, Dynamic nuclear polarization with an inhomogeneously broadened ESR line, *Phys. Rev. B*, 1976, **13**:9, 3671-3685.

27. K. Hu, H. Yu, T.M. Swager, and R.G. Griffin, Dynamic nuclear polarization with biradicals, *J. Am. Chem. Soc.*, 2004, **126**, 10844-10845.

28. F. Mentink-Vigier, S. Paul, D. Lee, A. Feintuch, S. Hediger, S. Vega and G. De Paëpe, Nuclear depolarization and absolute sensitivity in magic-angle spinning cross effect dynamic nuclear polarization, *Phys. Chem. Chem. Phys.*, 2015, **17**, 21824–21836.

29. F. Mentink-Vigier, G. Mathies, Y. Liu, A.-L. Barra, M. A. Caporini, D. Lee, S. Hediger, R. G. Griffin and G. De Paëpe, Efficient cross-effect dynamic nuclear polarization without depolarization in high-resolution MAS NMR, *Chem. Sci.*, 2017, **8**, 8150–8163.

30. K. R. Thurber and R. Tycko, Theory for cross effect dynamic nuclear polarization under magic-angle spinning in solid state nuclear magnetic resonance: the importance of level crossings., *J. Chem. Phys.*, 2012, **137**, 084508.

31. K. R. Thurber and R. Tycko, Perturbation of nuclear spin polarizations in solid state NMR of nitroxide-doped samples by magic-angle spinning without microwaves, *J. Chem. Phys.*, 2014, **140**, 184201.

32. F. Mentink-Vigier, Ü. Akbey, Y. Hovav, S. Vega, H. Oschkinat and A. Feintuch, Fast passage dynamic nuclear polarization on rotating solids, *J. Magn. Reson.*, 2012, **224**, 13–21.

33. A. Lund, A. Equbal and S. Han, Tuning nuclear depolarization under MAS by electron T 1e, *Phys. Chem. Chem. Phys.*, 2018, **20**, 23976–23987.

34. F. Mentink-Vigier, I. Marin-Montesinos, A. P. Jagtap, T. Halbritter, J. Van Tol, S. Hediger, D. Lee, S. T. Sigurdsson and G. De Paëpe, Computationally-assisted design of polarizing agents for dynamic nuclear polarization enhanced NMR: the AsymPol family, *J. Am. Chem. Soc.*, 2018, **140**, 11013–11019.

35. D. Wisser, G. Karthikeyan, A. Lund, G. Casano, H. Karoui, M. Yulikov, G. Menzildjian, A. C. Pinon, A. Purea, F. Engelke, S. R. Chaudhari, D. Kubicki, A. J. Rossini, I. B. Moroz, D. Gajan, C. Copéret, G. Jeschke, M. Lelli, L. Emsley, A. Lesage and O. Ouari, BDPA-Nitroxide Biradicals Tailored for Efficient Dynamic Nuclear Polarization Enhanced Solid-State NMR at Magnetic Fields up to 21.1 T, *J. Am. Chem. Soc.*, 2018, **140**, 13340–13349.

36. G. Mathies, M. A. Caporini, V. K. Michaelis, Y. Liu, K.-N. Hu, J. L. Zweier, M. Rosay, M. Baldus and R. G. Griffin, Efficient Dynamic Nuclear Polarization at 800 MHz / 527 GHz with Trityl-nitroxide Biradicals, *Angew. Chem. Int. Ed.*, 2015, **54**, 11770–11774.

37. E. L. Sesti, N. Alaniva, P. W. Rand, E. J. Choi, B. J. Albert, E. P. Saliba, F. J. Scott and A. B. Barnes, Magic Angle Spinning NMR Below 6 K with a Computational Fluid Dynamics Analysis of Fluid Flow and Temperature Gradients, *J. Magn. Reson.*, 2017, **286**, 1–9.

38. B. J. Albert, S. H. Pahng, N. Alaniva, E. L. Sesti, P. W. Rand, E. P. Saliba, F. J. Scott, E. J. Choi and A. B. Barnes, Instrumentation for cryogenic magic angle spinning dynamic nuclear polarization using 90 L of liquid nitrogen per day, *J. Magn. Reson.*, 2017, **283**, 71–78.

39. D. Lee, E. Bouleau, P. Saint-Bonnet, S. Hediger and G. De Paëpe, Ultra-low temperature MAS-DNP, *J. Magn. Reson.*, 2016, **264**, 116–124.

40. K. R. Thurber, A. Potapov, W. M. Yau and R. Tycko, Solid state nuclear magnetic resonance with magic-angle spinning and dynamic nuclear polarization below 25 K, *J. Magn. Reson.*, 2013, **226C**, 100–106.

41. E. L. Sesti, E. P. Saliba, N. Alaniva and A. B. Barnes, Electron decoupling with cross polarization and dynamic nuclear polarization below 6 K, *J. Magn. Reson.*, 2018, **295**, 1–5.

42. B. J. Albert, C. Gao, E. L. Sesti, E. P. Saliba, N. Alaniva, F. J. Scott, S. T. Sigurdsson and A. B. Barnes, Dynamic Nuclear Polarization Nuclear Magnetic Resonance in Human Cells Using Fluorescent Polarizing Agents, *Biochemistry*, 2018, **57**, 4741–4746.

43. E. Bouleau, P. Saint-bonnet, F. Mentink-vigier, H. Takahashi, J. Jacquot, M. Bardet, F. Aussenac, A. Purea, F. Engelke, S. Hediger, D. Lee, and G. De Paëpe, Pushing NMR sensitivity limits using dynamic nuclear polarization with closed-loop cryogenic helium sample spinning, *Chem. Sci.* 2015, **6**, 6806–6812.

44. F. J. Scott, N. Alaniva, N. C. Golota, E. L. Sesti, E. P. Saliba, L. E. Price, B. J. Albert, P. Chen, R. D. O'Connor and A. B. Barnes, A Versatile Custom Cryostat for Dynamic Nuclear Polarization Supports Multiple Cryogenic Magic Angle Spinning Transmission Line Probes, *J. Magn. Reson.*, 2018, **297**, 23–32.

45. D. Massiot, F. Fayon, M. Capron, I. King, S. Le Calvé, B. Alonso, J. O. Durand, B. Bujoli, Z. Gan and G. Hoatson, Modelling one- and two-dimensional solid-state NMR spectra, *Magn. Reson. Chem.*, 2002, **40**, 70–76.

46. T. A. Siaw, A. Leavesley, A. Lund, I. Kaminker and S. Han, A versatile and modular quasi optics-based 200 GHz dual dynamic nuclear polarization and electron paramagnetic resonance instrument, *J. Magn. Reson.*, 2016, **264**, 131–153.

47. H. Takahashi, C. Fernández-de-alba, D. Lee, V. Maurel, S. Gambarelli, M. Bardet, S. Hediger, A. Barra and G. De Paëpe, Optimization of an absolute sensitivity in a glassy matrix during DNP-enhanced multidimensional solid-state NMR experiments, *J. Magn. Reson.*, 2014, **239**, 91–99.

48. A.E. Bennett, C.M. Rienstra, M. Auger, K.V. Lakshmi, and R.G. Griffin, Heteronuclear decoupling in rotating solids, *J. Chem. Phys.*, 1995, **103**:16, 6951-6958.

49. H. Takahashi, D. Lee, L. Dubois, M. Bardet, S. Hediger, and G. De Paëpe, Rapid Natural-Abundance 2D 13 C – 13 C Correlation Spectroscopy Using Dynamic Nuclear Polarization Enhanced Solid-State NMR and Matrix- Free Sample Preparation *Angew. Chem. Int. Ed.*, 2012, 11766–11769.

50. A. E. Bennett, C. M. Rienstra, J. M. Griffiths, W. Zhen, P. T. Lansbury and R. G. Griffin, Homonuclear radio frequency-driven recoupling in rotating solids, *J. Chem. Phys.*, 1998, **108**, 9463–9479.

51. D. Shimon, Y. Hovav, A. Feintuch, D. Goldfarb, and S. Vega, Dynamic nuclear polarization in the solid state: a transition between the cross effect and the solid effect, *Phys. Chem. Chem. Phys.*, 2012, **14**, 5729-5743.

52. N. M. Szevereny, M. J. Sullivan and G. E. Maciel, Observation of Spin Exchange by Two-Dimensional Fourier Transfrom 13C Cross Polarization-Magic-Angle Spinning, *J. Magn. Reson.*, 1982, **47**, 462–475.

53. S. Grzesiek and A. Bax, Improved 3D triple-resonance NMR techniques applied to a 31 kDa protein, *J. Magn. Reson.*, 1992, **96**, 432–440.

54. J. D. Gross, P. R. Costa, J. P. Dubacq, D. E. Warschawski, P. N. Lirsac, P. F. Devaux and R. G. Griffin, *J. Magn. Reson. Ser. B*, 1995, 106, 187–190.

55. A. B. Barnes, B. Corzilius, M. L. Mak-Jurkauskas, L. B. Andreas, V. S. Bajaj, Y. Matsuki, M. L. Belenky, J. Lugtenburg, J. R. Sirigiri, R. J. Temkin, J. Herzfeld and R. G. Griffin, Resolution and Polarization Distribution in Cryogenic DNP/MAS Experiments, *Phys. Chem. Chem. Phys.*, 2010, **12**, 5681–5687.

56. H.Y. Chen and R. Tycko, Temperature-Dependent Nuclear Spin Relaxation Due to Paramagnetic Dopants below 30 K: Relevance to DNP-Enhanced Magnetic Resonance Imagin. *J. Phys. Chem. B.* 2018, **122**, 11731-11742.

57. A. Lund, A. Equbal, and S. Han, Tuning nuclear depolarization under MAS by electron T_{1e}. *Phys. Chem. Chem. Phys.* 2018, **20**, 23976-23987.

58. N. Alaniva, E.P. Saliba, E.L. Sesti, P.T. Judge, and A.B. Barnes, Electron Decoupling with Chirped Microwave Pulses for Rapid Signal Acquisision and Electron Saturation Recovery. *Angew. Chem. Int. Ed.* 2019, doi:10.1002/anie.201900139.

Chapter 3: DNP with Electron Decoupling in Intact Human Cells and Cell Lysates

Forward

This chapter was adapted from the paper "Dynamic Nuclear Polarization with Electron Decoupling in Intact Human Cells and Cell Lysates" by Patrick T. Judge*, Erika L. Sesti*, Lauren E. Price, Brice J. Albert, Nicholas Alaniva, Edward P. Saliba, Thomas Halbritter, Snorri Th. Sigurdsson, George B. Kyei, and Alexander B. Barnes. This chapter builds on the work from the previous chapter by demonstrating further improvement in the sensitivity of solid effect radicals below 6 K through the application of electron decoupling, which mitigates hyperfine interactions between electrons and nuclei, improving the sensitivity and resolution of NMR experiments. Further, it demonstrates the feasibility of performing such experiments in biologically relevant samples including intact human cells and human and bacterial cellular lysates. Beyond the application of electron decoupling, one important result from these experiments is the demonstration of exceptionally short ^{1}H T_{1DNP} relaxation times with the newly synthesized trityl-Me_3N radical, a methylated variant of the trityl Finland radical. These results lay the groundwork for performing rapid, highly sensitive MAS DNP NMR experiments in complex cellular environments.

3.1 Overview

Dynamic nuclear polarization (DNP) is used to improve the inherently poor sensitivity of nuclear magnetic resonance (NMR) spectroscopy by transferring spin polarization from electrons to

nuclei. However, DNP radicals within the sample can have detrimental effects on NMR spins close to the polarizing agent. Chirped microwave pulses and electron decoupling (eDEC) attenuate these effects in model systems, but this approach has yet to be applied to intact cells or cellular lysates. Here, we demonstrate for the first time in the literature exceptionally fast ^{1}H T_{1DNP} times of just 200 ms and 300 ms at 90 K and 6 K, respectively, using a newly synthesized methylated trityl radical within intact human cells. We further demonstrate that eDEC can also be applied to intact human cells and human and bacterial cell lysates. We investigate eDEC efficiency at different temperatures, with different solvents, and with two trityl radical derivatives. At 90 K, eDEC yields a ^{13}C signal intensity increase of 8% in intact human cells and 10% in human and bacterial cell lysates. At 6 K, eDEC provides larger intensity increases of 15% and 39% in intact human cells and cell lysates, respectively. Combining the manipulation of electron spins with frequency-chirped pulses and sample temperatures approaching absolute zero is a promising avenue for executing rapid, high-sensitivity magic angle spinning DNP in complex cellular environments.

3.2 Introduction

Solid-state nuclear magnetic resonance (NMR) is a valuable method for studying biological systems at atomic resolution [1–7]; however, it suffers from an inherent lack of sensitivity [8–10]. In complex biological environments, NMR sensitivity is further challenged by low endogenous cellular concentrations of molecules of interest. Dynamic nuclear polarization (DNP) can increase NMR sensitivity by orders of magnitude by transferring spin polarization from electron paramagnetic resonance (EPR)-active polarizing agents to target nuclear spins [11–20]. While DNP polarizing agents boost polarization, they can also cause deleterious paramagnetic effects such as shorter coherence lifetimes (line-broadening) and signal attenuation [21–24]. These effects become more severe as hyperfine interactions increase. Recently, we introduced a strategy to attenuate

hyperfine couplings by decoupling electron-nuclear interactions with frequency-chirped microwave pulses generated by a frequency-agile gyrotron [25,26]. Electron decoupling (eDEC) has been successfully applied to model systems of small molecules suspended in a cryoprotecting glassy matrix (glycerol-d_8/D_20/H_20, 60/30/10%) [25,27]. Extending eDEC to more complex samples is important for translational studies in biological systems.

Establishing the structure-function relationship of molecular architectures of interest is fundamental to many biological studies. Reductive approaches are often employed to study biomolecular structures in simplified environments *in vitro.* However, proteins, drugs, and biomolecules of biomedical importance do not necessarily have the same behavior, or structural ensembles, in simple *in vitro* environments as they do in the cellular context or *in vivo*. Recent studies have demonstrated the profound effect of the complex cellular environment on protein structure [28,29].

Complex mixtures also have significant effects on DNP efficiency [30]. While different formulations can be detrimental to DNP *in vitro*, we recently demonstrated excellent DNP performance in intact human cells [31]. To transition eDEC with DNP to in-cell structural biology, the efficacy of eDEC must be demonstrated in more complex cellular environments. Chirped microwave pulses, which improve control over electronic and hyperfine interactions within the Hamiltonian, are a promising route to improve in-cell NMR. Here, we perform effective eDEC in isotopically-enriched intact human cells and human and bacterial cell lysates at 90 K and 6 K with two different trityl radicals (Finland trityl radical and trityl-Me_3N). Trityl-Me_3N is a newly synthesized polarizing agent designed to penetrate cellular membranes and also shorten magnetization recovery delays[32,33]. We present exceptionally short ^1H T_{1DNP} times with the trityl-Me_3N radical in intact human cells below 6 K.

3.3 Methods

3.3.1 Solid Effect Radicals

Two tertiary carbon stable organic radical containing compounds, Finland trityl radical (Oxford Instruments, Concord, MA) and trityl-Me_3N were investigated. While eDEC has been successfully applied to model systems, it has yet to be demonstrated within intact cells. Direct DNP transfers and eDEC within intact cells require penetration of DNP polarizing agents through membranes and distribution throughout cells. In addition to the Finland trityl radical, we also explored the use of trityl-Me_3N. The trityl-Me_3N derivative was synthesized and deployed in this study to exploit the additional advantage of the methyl groups, leading to faster replenishing of magnetization (shorter ^1H T_{1DNP}) and higher sensitivity experiments[34].

3.3.2 Human Cell Lysate Preparation

For human cell lysates, Jurkat T cells (ATCC, Manassas, VA) were cultured in [U-^{13}C, 98%; U-^{15}N, 98%] BioExpress-6000 mammalian cell growth medium (Cambridge Isotope Laboratories, Tewksbury, MA) at a concentration of 3 x 10^6 cells/mL in a six-well plate at 37°C and 5% CO_2 for 48 h. 4.0 x 10^7 cells were collected, spun at 170 x g for 5 min, washed with 1x phosphate-buffered saline (PBS), and spun again at 170 x g for 5 min to remove extracellular NMR labels. A solution was prepared for DNP cryoprotection and cell lysis by dissolving 40 mM Finland trityl radical in a solution of 60% glycerol-d_8, 30% D_2O, 10% H_2O (cryoprotecting glassy matrix). Triton X-100 was added to a final concentration of 0.5 v/v% to lyse the cells. 30 µL of cryoprotecting matrix combined with cell lysis solution was added to the cell pellet, and 36 µL of the resulting suspension was added to a 3.2 mm zirconia rotor and frozen in liquid nitrogen.

3.3.3 Intact Human Cell Preparation

Jurkat cells for intact human cell experiments were cultured and washed under the same conditions as the Jurkat cells for the lysed samples, except cells were plated at 2 x 10^6 cells/mL and 3.6 x 10^7 cells were collected for each experiment. The cell pellet was resuspended in 36 µL of 1x PBS with

10% DMSO containing either 40 mM of the Finland trityl radical or trityl-Me_3N radical. This suspension was centrifuged directly into the 3.2 mm zirconia rotor at 800 x g for 30 s and immediately frozen in liquid nitrogen as detailed in our previous work [31].

3.3.4 Bacteria Cell Lysate Preparation

Rosetta electro-competent *Escherichia coli* (*E. coli*) cells electroporated with a PGEX-4T plasmid (Genscript, Piscataway, NJ) bearing an insert coding for the C1b domain of the δ isoform of protein kinase C (PKC-δ) were incubated in Super Optimal Broth (S.O.C.) medium for one hour before plating on selective medium. The colonies obtained were then cultured in 200 mL ^{15}N, ^{13}C, ^{2}H-labeled ISOGROW complex medium (Sigma Aldrich, St Louis, MO) until the 600 nm optical density reached the midlog point (0.6). Then, the culture was induced and left to incubate and grow overnight at 20°C. The cells were collected by centrifugation. All buffers were completely deuterated to minimize the ^{1}H concentration. Pellets were lysed in lysis buffer by sonication and the lysate was then centrifuged. The soluble fraction was decanted, steri-filtered, and incubated for 2.5 h at room temperature with 1.2 mL glutathione-S-transferase (GST) beads (Thermo-Fisher Scientific, Waltham, MA) to isolate the GST-PKC C1b from the soluble fraction. The beads were then centrifuged at 600 x g for 4 min and the supernatant removed. A pellet was obtained from the supernatant by ultra-centrifugation at 4°C for 48 h. 8 mg of pellet was mixed with 100 µL 40 mM of the Finland trityl radical and fully deuterated cryoprotecting matrix (60% glycerol-d_8, 40% D_20 volume ratio), and 36 µL was packed into a 3.2 mm zirconia rotor. Another 8 mg of pellet was mixed with 100 µL of 40 mM Finland trityl radical in deuterated buffer, and 36 µL was packed into a 3.2 mm zirconia rotor.

3.3.5 NMR Experiments

All experiments were performed using a custom-built NMR MAS transmission line probe [35] with a Redstone (Tecmag Inc. Houston, TX) spectrometer. The Larmor frequencies of ^{1}H and ^{13}C at B_0 = 7.05 T were 300.179 MHz and 75.4937 MHz, respectively. The pulse sequence was a ^{13}C rotor-synchronized Hahn echo with eDEC applied over the Hahn echo pulse sequence and the acquisition as published previously [25]. Polarization times were 7 s, and the spinning frequency was 4 kHz. The ν_{13C} was 83 kHz, and TPPM ^{1}H decoupling had a ν_{1H} of 83 kHz. 3,072 transients of each spectrum were recorded, and the temperature of all experiments was maintained at 95 K or 6-7 K. DMFit [36] was used to fit the ^{13}C carbonyl resonance at approximately 180 ppm in each spectrum, and the resulting area under the curve was used to calculate the percent increase in area with eDEC. ^{1}H polarization build up times (^{1}H T_{1DNP}) were recorded using a saturation recovery CPMAS sequence with the ν_{1H} used above.

Microwaves and chirped pulses were generated from a custom-built frequency-agile gyrotron [37]. For the DNP condition, the microwave frequency was 197.719 GHz. The chirped pulses were centered on the trityl EPR resonance of 197.640 GHz with a sweep width of 103 MHz and a sweep time of 13.75 μs. The incident microwave power on the sample was 7 W, resulting in an estimated Rabi frequency (γB_{1S}) of 0.70 MHz.

A stream of liquid helium was directed at the sample centered within spinning zirconia rotors to achieve sample temperatures near 6 K, as described previously [38]. Bearing and drive were ultra-high purity helium gas maintained at 80 K. A calibrated Cernox temperature sensor (Lake Shore Cryotronics, Inc., Westerville, OH) was used to monitor the sample temperature at the interface of the variable temperature (VT) outlet and NMR stator [38]. The temperature of the sample, incoming transfer lines, and exhaust line were monitored with a Lake Shore temperature controller.

3.4 Results and Discussion

We previously demonstrated eDEC at 90 K in a model system of [U-^{13}C,^{15}N] urea using direct polarization transfer from electron spins to carbon nuclei [25]. We also performed eDEC in magic angle spinning (MAS) experiments below 6 K in model systems of [U-^{13}C,^{15}N] urea and [U-^{13}C,^{15}N] L-proline using cross-polarization [27,39]. Here we demonstrate direct carbon polarization with eDEC at 90 K and 6 K in more complex biological systems including intact and lysed human Jurkat T cells, and also in the soluble fraction of *Escherichia coli* bacterial cell lysates.

3.4.1 eDEC on Bacterial Cell Lysates

We first performed solid effect cross-polarization (CP)-MAS and eDEC on the purified soluble fraction of *E. coli* cell lysates (**Figs. 1 and 2**) using the Finland trityl radical to analyze the effect of solvent (cryoprotecting matrix or buffer) on DNP and eDEC efficiency. At 90 K, the soluble fraction of the *E. coli* cell lysate dissolved in cryoprotecting matrix showed a 35-fold ^{13}C enhancement of the carbonyl resonance intensity (**Fig. 1a**). The same sample suspended in buffer provided a slightly smaller, yet significant, 31-fold enhancement (**Fig. 1b**). This smaller enhancement was unsurprising, as the glassy matrix formed with the cryoprotecting solvent is well suited to distributing the radical and efficient DNP, and thus is expected to provide a greater enhancement than a buffer solution [30].

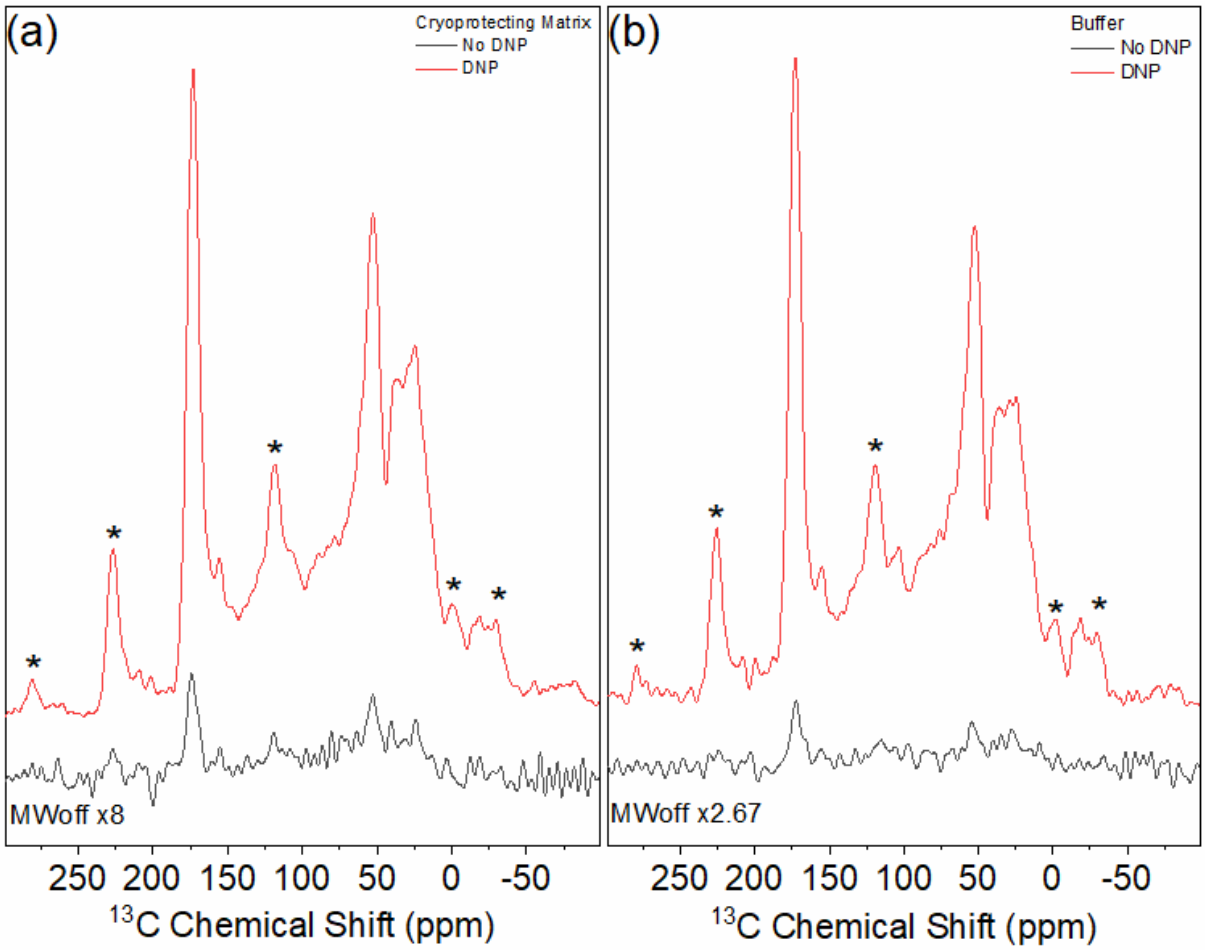

Figure 1. ^{13}C enhancements at 90 K of bacterial cell lysates with the Finland trityl radical in (**a**) a cryoprotecting matrix (32 DNP scans, 256 No DNP scans; ε = 35 +/- 1) and in (**b**) buffer (96 DNP scans, 256 No DNP scans; ε = 31 +/- 1). Red represents the ^{13}C signal with DNP; black is without DNP.

Similar to the lower DNP efficiency, eDEC performance in the bacteria lysate sample with a cryoprotecting matrix was also slightly less effective. At 90 K, eDEC enhanced the carbonyl resonance intensity of the lysate in a cryoprotecting matrix by 10 +/- 2% (**Fig. 2a**). The intensity of the lysate in deuterated buffer increased by a smaller percentage of 6.0 +/- 0.1% (**Fig. 2b**).

We also investigated high sensitivity experiments by lowering the sample temperature to 6 K (**Fig. 2c and d**). The carbonyl resonance intensity increased by 17 +/- 3% and 39 +/- 0.1% with electron

decoupling for the lysates in a cryoprotecting matrix and buffer, respectively, suggesting that the eDEC mechanism is independent of the DNP transfer efficiency.

Interestingly, at 90 K electron decoupling elicits a greater increase in intensity in the lysate sample with a cryoprotecting matrix than it does with buffer. However, at 6 K the reverse is true with the greater intensity increase occurring with the lysates with buffer. We postulate that this is due to differing polarization buildup times at each temperature. Polarization buildup times are expected to be longer at lower temperatures. Since we used the same polarization time for experiments at both temperatures, we are further from the optimal polarization time of $1.26*T_{1DNP}$ at 6 K than at 90 K. Thus, at 90 K we are reporting on observed spins with stronger hyperfine couplings, yielding a larger increase in intensity with electron decoupling in the cryoprotecting matrix, whereas the opposite is true at 6 K.

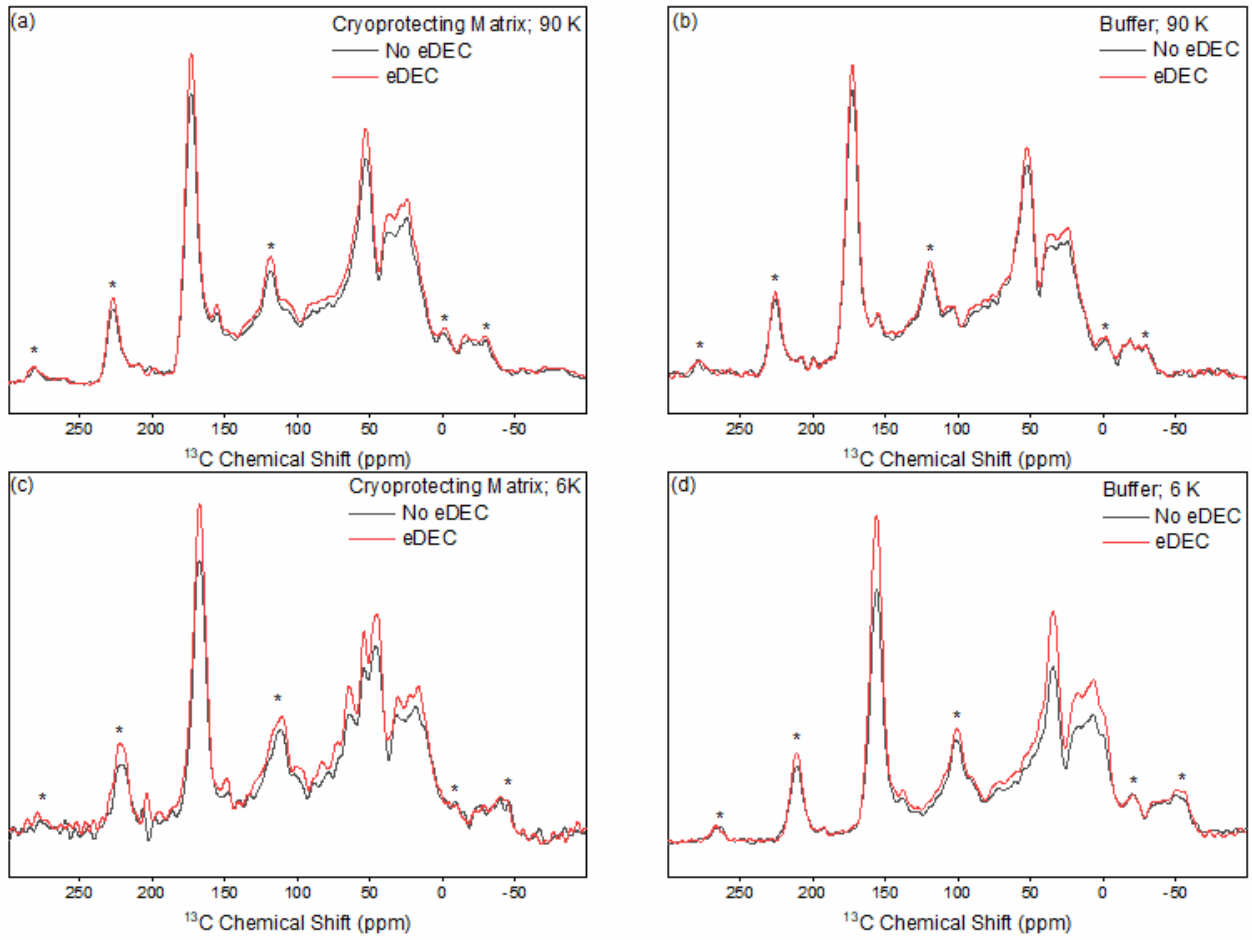

Figure 2. eDEC of bacterial cell lysates at 90 K in (**a**) a cryoprotecting matrix (32 scans) and (**b**) buffer (96 scans) and at 6 K in (**c**) a cryoprotecting matrix (4 scans) and (**d**) buffer (4 scans). Black represents no eDEC, while red is with eDEC. At 90 K, eDEC increased the spectrum intensity by 10 +/- 2% with a cryoprotecting matrix and 6.0 +/- 0.1% with buffer. These increases were about doubled at 6 K, where the intensity increased 17 +/- 3% with a cryoprotecting matrix and 39 +/- 0.1% with buffer.

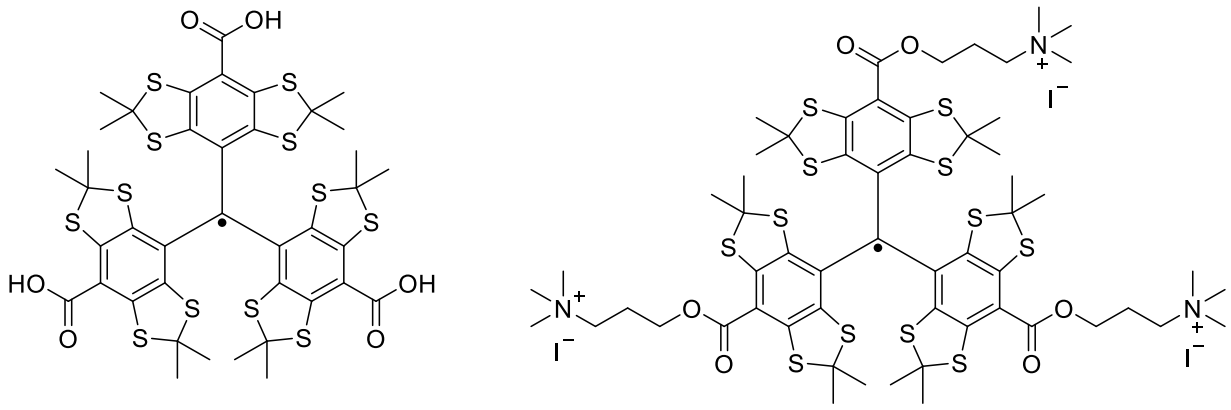

Figure 3. Chemical structures of the trityl derivatives, Finland trityl radical (left) and trityl-Me_3N (right).

3.4.2 eDEC on Intact Human Cells and Human Cell Lysates

^{13}C enhancements were recorded at 90 K to determine DNP performance to target nuclear spins within intact cells and cellular lysates (**Fig. 4**) and to probe the cellular uptake of the trityl derivatives (**Fig. 3**). In Jurkat lysates with the Finland trityl radical, nuclear spins were enhanced by a factor of 29.4 +/- 0.9 (**Fig. 4a**). In intact cells, the nuclear spins were enhanced by factors of 4.1 +/- 0.2 and 4.0 +/- 0.2 with the Finland trityl radical and trityl-Me_3N, respectively (**Fig. 4b,c**). The enhancements in intact cells were likely lower due to cellular localization; in the lysate, radicals are evenly distributed throughout the lysed cellular material, whereas in a cell they are likely to be subcellularly localized, limiting the number of nuclear spins in close proximity for enhancement. Note that the ^{13}C spectra for the Jurkat lysates and intact Jurkat cells with both radicals had the same resonances and similar relative intensities. This, along with the exceptionally short ^{1}H T_{1DNP} buildup times with both radicals (see below, **Fig. 9**), indicates that both radicals successfully penetrated the cellular membrane and are distributed within the cell. Further, light microscopy was performed on Jurkat cell samples with no radical and with Trityl Finland radical to confirm that the cells were not lysed in the process of sample preparation (**Fig. 6**).

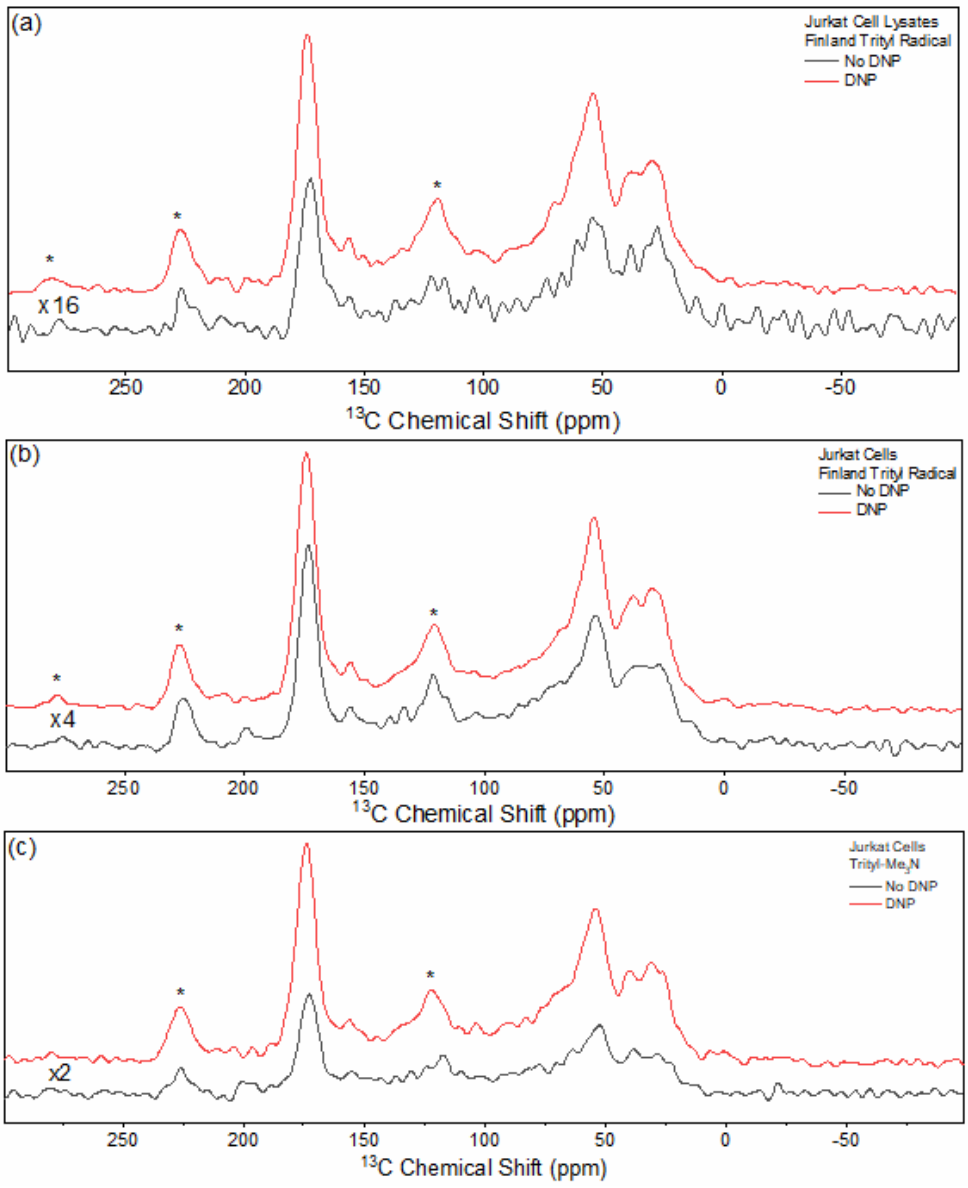

Figure 4. ^{13}C enhancements at 90 K in (**a**) Jurkat cell lysates with Finland trityl radical (256 DNP scans, 4,096 No DNP scans; ε = 29.4 +/- 0.9), (**b**) intact Jurkat cells with the Finland trityl radical (2,560 DNP scans, 10,240 No DNP scans; ε = 4.1 +/- 0.2), and (**c**) intact Jurkat cells with trityl-Me_3N (3,584 DNP scans, 6,144 No DNP scans; ε = 4.0 +/- 0.2). Red represents the ^{13}C signal with DNP, while black is without DNP.

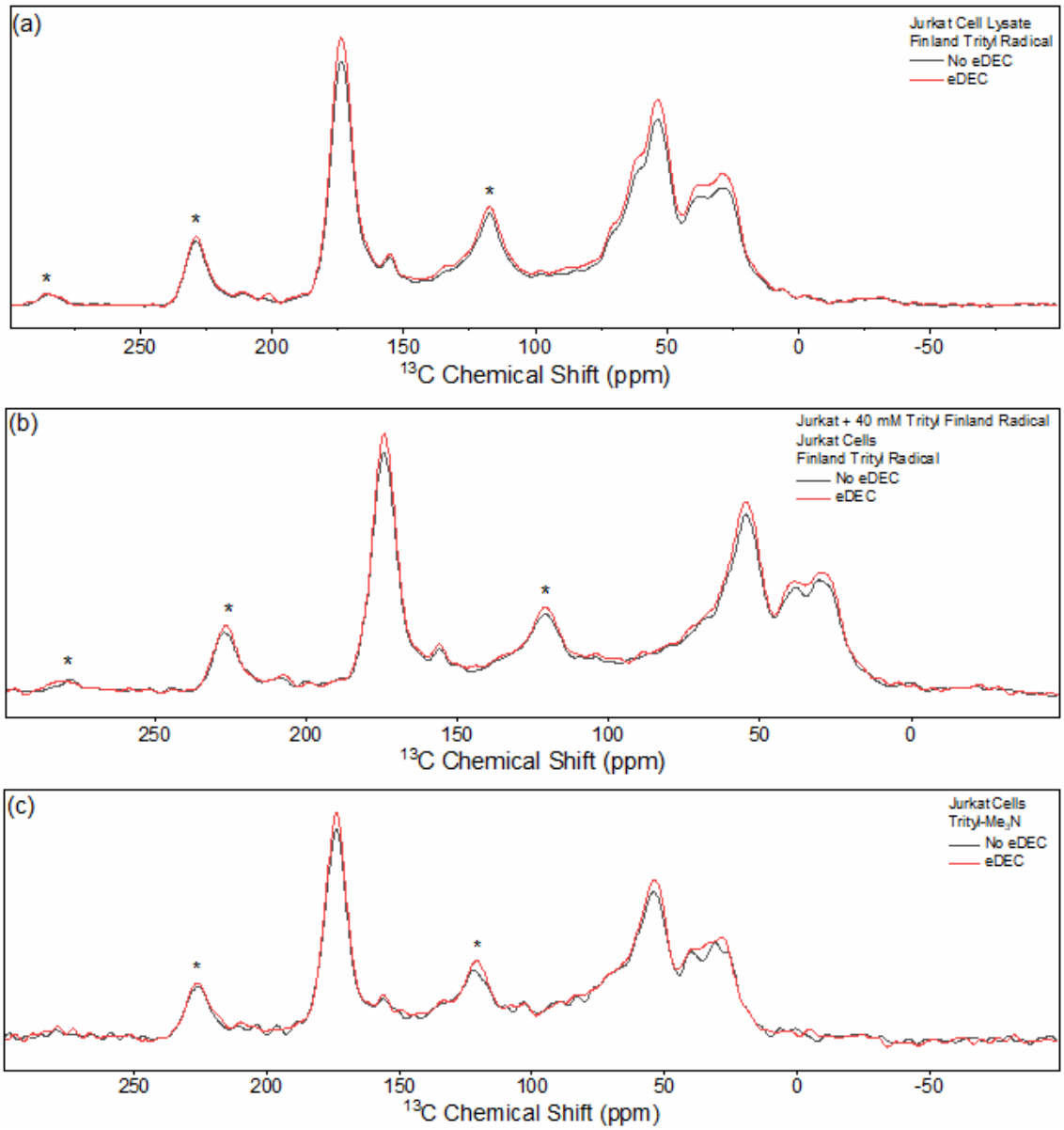

Figure 5: Comparison of DNP spectra with (red) and without (black) eDEC at 90 K for (**a**) Jurkat cell lysates with the Finland trityl radical (3,072 scans), (**b**) intact Jurkat cells with the Finland trityl radical (2,560 scans), and (**c**) intact Jurkat cells with trityl-Me_3N (3,584 scans). The carbonyl resonances increased in intensity by 8.2 +/- 3.2%, 8.2 +/- 2.8%, and 8.4 +/- 2.7%, respectively, with eDEC for each sample.

When eDEC was applied at 90 K, the intensity of the carbonyl resonances in the Jurkat cell lysates increased by 8.2 +/- 3.2% (**Fig. 5a**), and by 8.2 +/- 2.8% and 8.4 +/- 2.7% in intact Jurkat cells

with Finland trityl radical and trityl-Me_3N, respectively (**Fig. 5b,c**). This intensity improvement demonstrates that eDEC reveals nuclear spins not contributing to the NMR signal without eDEC due to paramagnetic effects. Moreover, the added cellular components do not prevent eDEC, which has a similar efficiency in these more complex biological systems as in previously studied model systems [25,27].

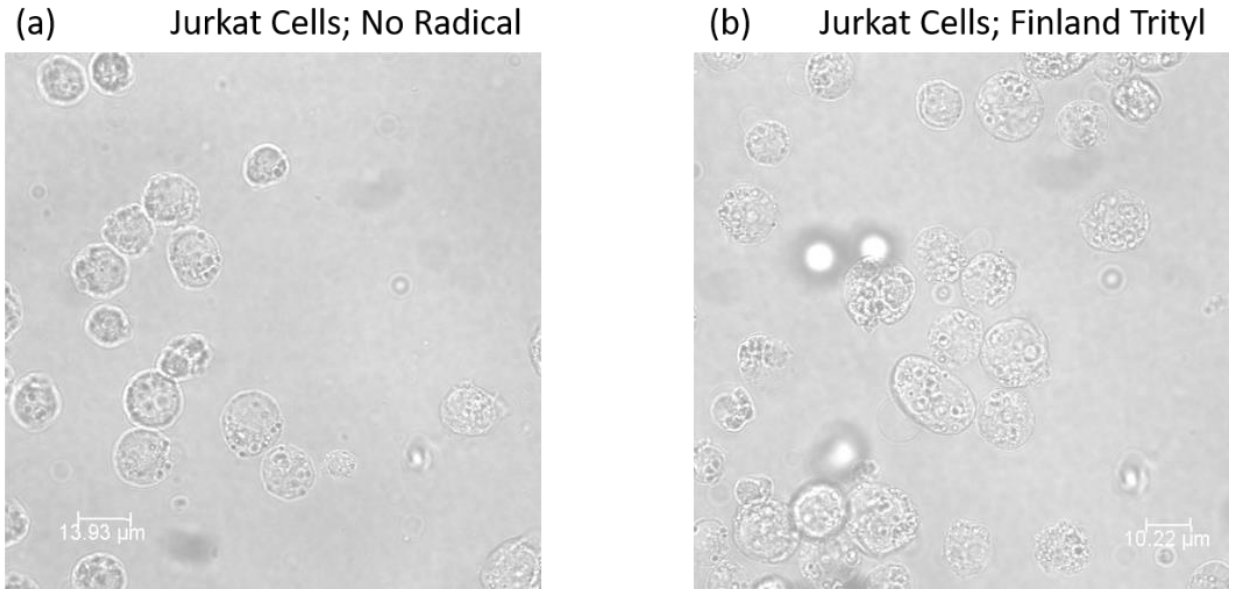

Figure 6: Light microscopy images of Jurkat cells with no radical (a), and Jurkat cells with Finland trityl radical (b).

To further improve sensitivity and to determine the effectiveness of eDEC in intact human cells at lower temperatures, the sample temperature was reduced to below 6 K (**Figs. 7, 8**). Again utilizing the solid effect DNP mechanism, there was about an 8-fold (7.6 +/- 0.3) enhancement in intact Jurkat cells with the Finland trityl radical (**Fig. 7a**) and a slightly larger 12-fold (12.5 +/- 3.8) enhancement in cells with the trityl-Me_3N radical (**Fig. 7b**). Compared to experiments at 90 K, the enhancement with Finland trityl radical increased by a factor of 1.9 while the enhancement with trityl-Me_3N increased by a factor of 3.1. These enhancements are likely due to improved polarization transfer efficiency associated with longer spin relaxation at lower temperatures.

Figure 8 shows that eDEC efficiency also improved in human cells at sample temperatures below 6 K. The carbonyl resonance intensity of intact cells using the Finland trityl radical and trityl-Me_3N increased by 12.4 +/- 3.0% (**Fig. 8a**) and 14.5 +/- 4.0% (**Fig. 8b**), respectively. In addition, slight linewidth narrowing was observed in the carbonyl resonance for both trityl derivatives.

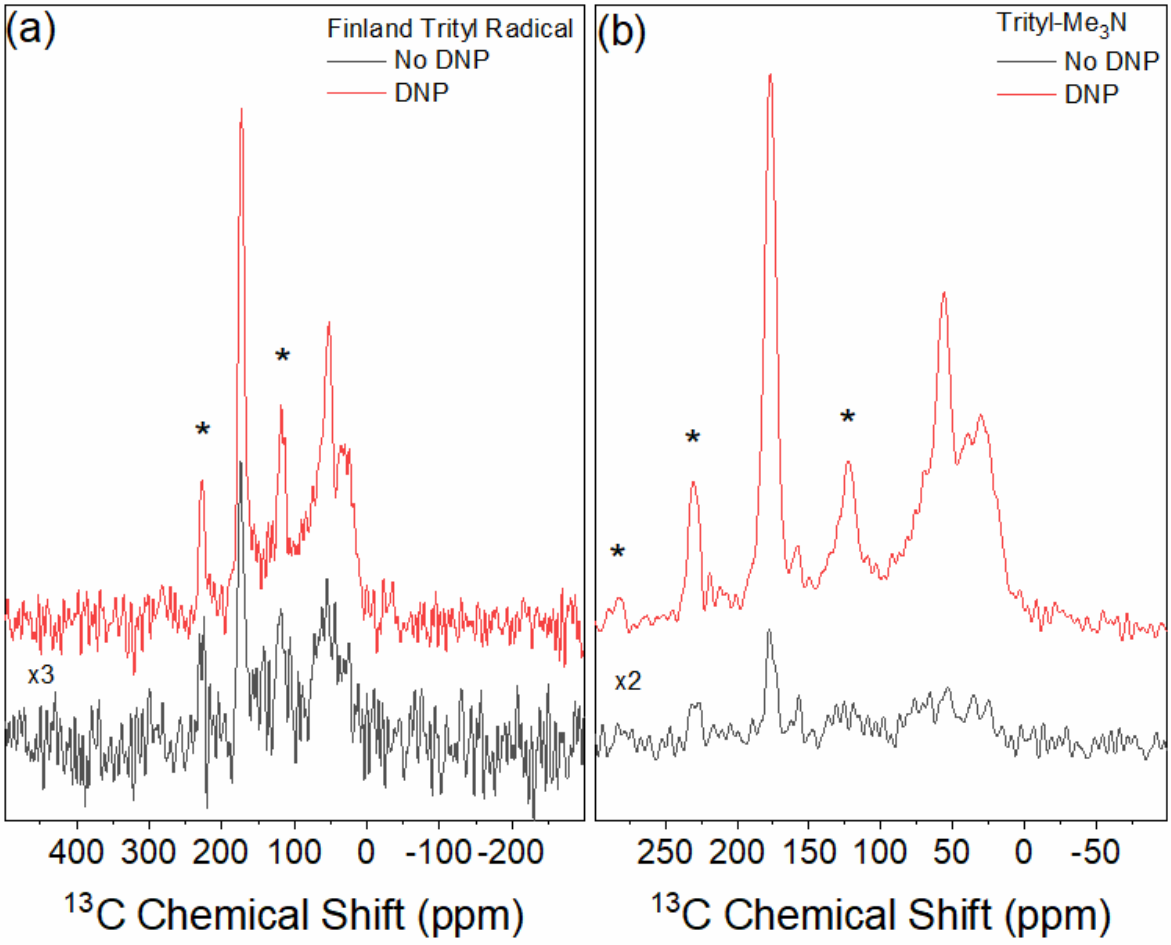

Figure 7. ^{13}C enhancements at 6 K in intact Jurkat cells with the (**a**) Finland trityl radical (24 DNP scans, 80 No DNP scans; ε = 7.6 +/- 0.3) and (**b**) trityl-Me_3N (40 DNP scans, 80 No DNP scans; ε = 12.5 +/-3.8). Red represents the ^{13}C signal with DNP, while black is without DNP.

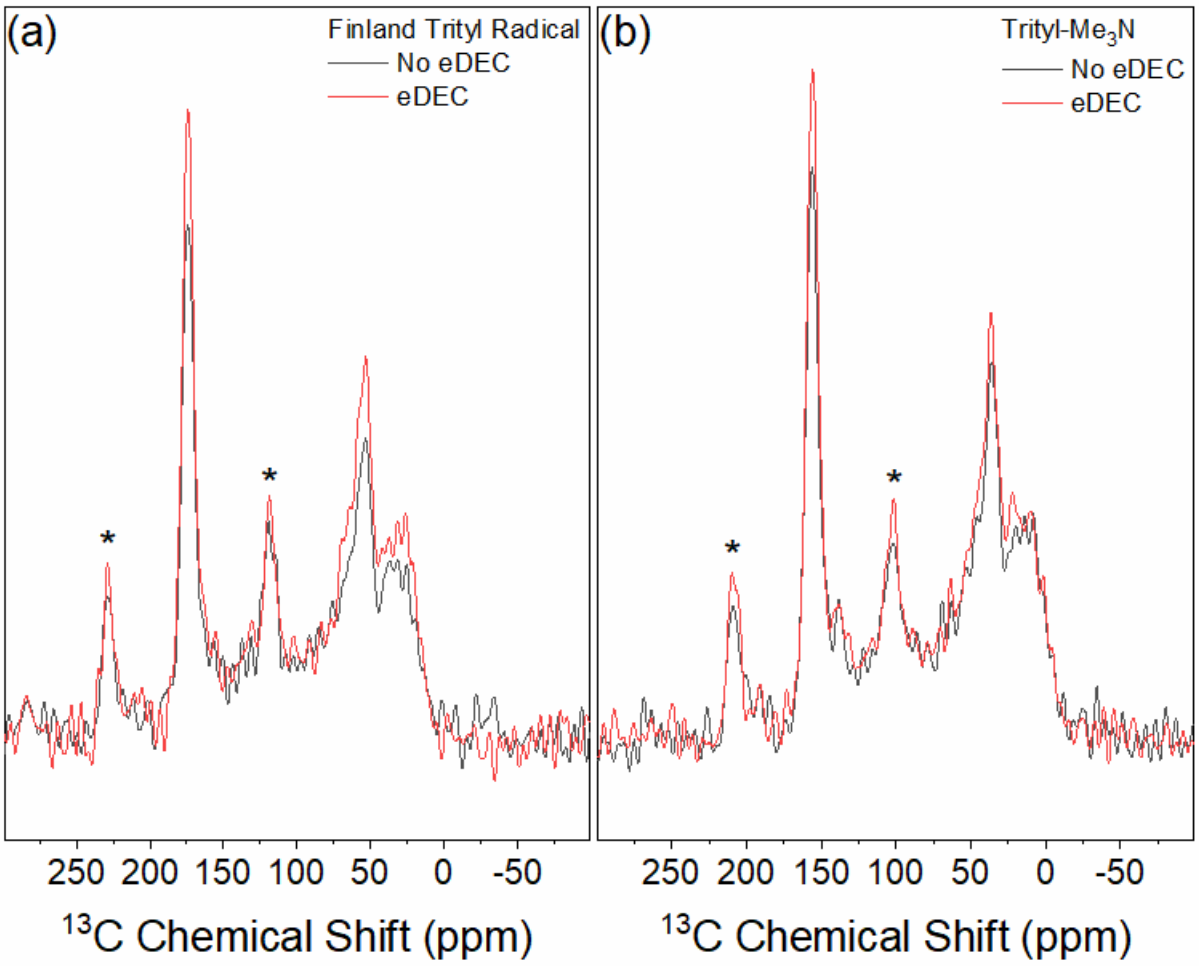

Figure 8: Comparison of DNP spectra with (red) and without (black) eDEC at 6 K for intact Jurkat cells with the (**a**) Finland trityl radical (24 scans) and (**b**) trityl-Me_3N (24 scans). The carbonyl resonances increased in intensity by 12.4 +/- 3.0% and 14.5 +/- 4.0%, respectively, with eDEC for each sample.

3.4.3 ^1H T_{1DNP} below 6 Kelvin in Human Cells

Electron decoupling with trityl-Me_3N yielded similar results to the Finland trityl radical at 90 K, yet below 6 K, trityl-Me_3N shows a smaller increase in intensity (**Fig. 8**), indicating that the Finland trityl radical is better suited to temperatures below 6 K. However, trityl-Me_3N has a unique advantage below 6 K (and also at 90 K) by virtue of its exceptionally short ^1H T_{1DNP} times (**Fig. 9**). At 90 K, intact Jurkat cells with the Finland trityl radical exhibited a ^1H T_{1DNP} of 1.6 ± 0.1 s

(**Fig. 9a**), while cells with trityl-Me_3N exhibited a ^1H T_{1DNP} that was 8-times shorter at 0.2 ± 0.01 s (**Fig. 9b**). The difference in ^1H T_{1DNP} times was similar at temperatures near 6 K: 2.7 ± 0.4 s with the Finland trityl radical and only 0.3 ± 0.01 s with trityl-Me_3N (**Fig. 9c,d**). We note that this proton polarization buildup time of 300 milliseconds is remarkably short and unprecedented in the literature. Although the mechanism is unclear, the methyl groups on trityl-Me_3N appear to significantly reduce the ^1H T_{1DNP}, as shown previously for bcTol and bcTol-M [34]. We previously showed that in model systems the ^1H T_{1DNP} is 19 s with the Finland trityl radical [27]; therefore, the complex cellular environment is conducive to short recovery times. Inhomogeneous distribution of the radical in the sample, which would lead to higher local concentrations of radical in these localized areas, could contribute to the shortening of the ^1H T_{1DNP} times for this radical. The short recovery times associated with the trityl-Me_3N polarizing agent are promising for extremely high sensitivity experiments below 6 K, as experiments can be repeated very quickly to yield incredible signal-to-noise per unit square root of time [40].

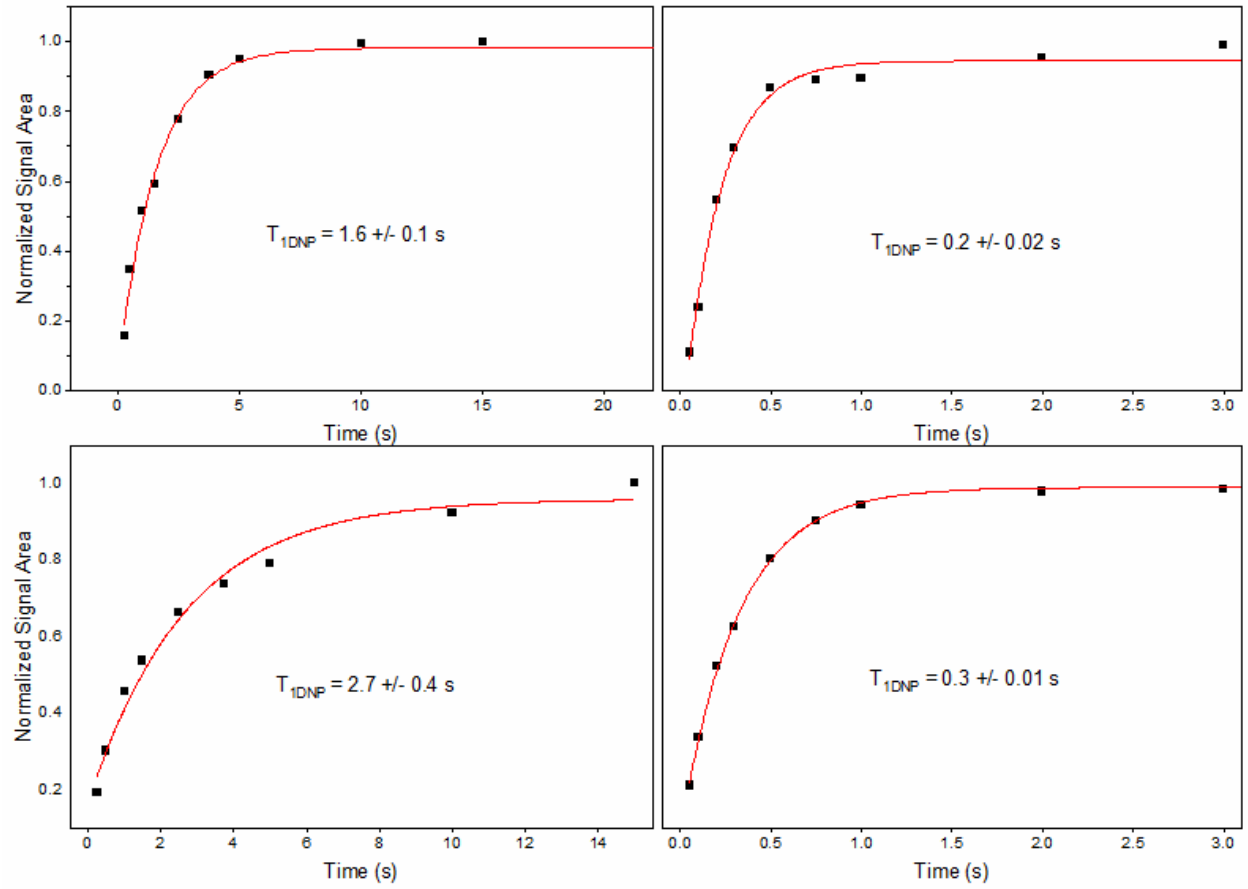

Figure 9. ^{1}H T_{1DNP} of intact Jurkat cells at 90 K with the Finland trityl radical (**a**) and trityl-Me_3N (**b**) and at 6 K with the Finland trityl radical (**c**) and trityl-Me_3N (**d**).

3.5 Conclusions and Outlook

Here, we demonstrated that the Finland trityl radical and trityl-Me_3N not only yield substantial sensitivity increases in human and bacterial cell lysates through DNP, but they can also be electron decoupled to further improve sensitivity. Furthermore, in bacterial cell lysates, these sensitivity improvements were shown to be largely independent of the sample matrix.

The intact human cells readily took up both trityl-based DNP polarizing agents. In these cells, DNP and eDEC successfully enhanced the sensitivity of the observed nuclear spins. Moreover, we demonstrated that NMR sensitivity in human cells can be readily improved by decreasing the sample temperature to below 6 K. The combination of DNP and eDEC at temperatures below 6 K

enabled the most sensitive NMR experiments recorded to date at 7 Tesla in intact human cells. In addition, we showed that trityl-Me_3N has extremely short ^1H T_{1DNP} times in cells, likely due to methyl groups not present in the Finland trityl radical. At temperatures below 6 K, the ^1H T_{1DNP} time was 0.3 s, which allows for exceptionally fast repetition of experiments. This pace of data acquisition, coupled with the already superb sensitivity at 6 K with DNP and eDEC, will facilitate structural biology in the human cellular context. Moreover, eDEC implemented with multidimensional NMR will provide the sensitivity enhancements and spectral resolution required for the analysis of complex biological systems. Lastly, we note that future implementation of DNP and eDEC for in-cell NMR will realize the ability to target radicals to specific sites of structural interest.

3.6 Acknowledgements

This work received financial support from the National Institute of Health (NIH) in the form of the grant DP2- GM119131, the National Science Foundation in the form of the grant NSF-IDBR (CAREER DBI-1553577), and the Camille Dreyfus Teacher-Scholar Awards Program. We thank Chukun Gao, Faith Scott, and Pin-Hui Chen for helpful discussions.

A.B.B is the author of a patent related to this work filed by the Washing University in Saint Louis (WO20115175507A1).

Author Contributions:

- Design and planning of experiments was a collaboration between Patrick Judge, Erika Sesti, Nicholas Alaniva, Edward Saliba, and Alexander Barnes
- Preparation of intact human cells and cell lysates was designed and carried out by Lauren Price, Brice Albert, and George Kyei

- Preparation of bacterial cell lysates was designed and carried out by Patrick Judge and Erika Sesti
- Trityl-Me_3N synthesis was designed and performed by Thomas Halbritter and Snorri Sigurdsson
- Experiments and analysis were carried out by Patrick Judge and Erika Sesti
- Manuscript was written and compiled as a collaboration between Patrick Judge, Erika Sesti, and Alexander Barnes

3.7 References

1. Polenova, T.; Gupta, R.; Goldbourt, A. Magic Angle Spinning NMR Spectroscopy: A Versatile Technique for Structural and Dynamic Analysis of Solid-Phase Systems. *Anal. Chem.* **2015**, *87*, 5458–5469.

2. Kaplan, M.; Narasimhan, S.; Heus, C. De; Mance, D.; van Doorn, S.; Houben, K.; Popov-Celeketic, D.; Damman, R.; Katrukha, E. A.; Jain, P.; et al. EGFR Dynamics Change during Activation in Native Membranes as Revealed by NMR Article EGFR Dynamics Change during Activation in Native Membranes as Revealed by NMR. *Cell* **2016**, *167*, 1241–1251.

3. Mak-Jurkauskas, M. L.; Bajaj, V. S.; Hornstein, M. K.; Belenky, M.; Griffin, R. G.; Herzfeld, J. Energy Transformations Early in the Bacteriorhodopsin Photocycle Revealed by DNP-Enhanced Solid-State NMR. *Proc. Natl. Acad. Sci.* **2008**, *105* (3), 883–888.

4. Selenko, P.; Wagner, G. Looking into Live Cells with In-Cell NMR Spectroscopy. *J. Struct. Biol.* **2007**, *158*, 244–253.

5. Wylie, B. J.; Dzikovski, B. G.; Pawsey, S.; Caporini, M.; Rosay, M.; Freed, J. H.; McDermott, A. E. Dynamic Nuclear Polarization of Membrane Proteins: Covalently Bound Spin-Labels at Protein-Protein Interfaces. *J. Biomol. NMR* **2015**, *61* (3–4), 361–367.

6. Ceccon, A.; Tugarinov, V.; Bax, A.; Clore, M. G. Global Dynamics and Exchange Kinetics of a Protein on the Surface of Nanoparticles Revealed by Relaxation-Based Solution NMR Spectroscopy. *J. Am. Chem. Soc.* **2016**, *138* (18), 5789–5792.

7. Gupta, R.; Lu, M.; Hou, G.; Caporini, M. A.; Rosay, M.; Maas, W.; Struppe, J.; Suiter, C.; Ahn, J.; Byeon, I. J. L.; et al. Dynamic Nuclear Polarization Enhanced MAS NMR Spectroscopy for Structural Analysis of HIV-1 Protein Assemblies. *J. Phys. Chem. B*

2016, *120* (2), 329–339.

8. Lilly Thankamony, A. S.; Wittmann, J. J.; Kaushik, M.; Corzilius, B. Dynamic Nuclear Polarization for Sensitivity Enhancement in Modern Solid-State NMR. *Prog. Nucl. Magn. Reson. Spectrosc.* **2017**, *102–103*, 120–195.

9. Saliba, E. P.; Sesti, E. L.; Alaniva, N.; Barnes, A. B. Pulsed Electron Decoupling and Strategies for Time Domain Dynamic Nuclear Polarization with Magic Angle Spinning. *J. Phys. Chem. Lett.* **2018**, *9*, 5539–5547.

10. Dale, M. W.; Wedge, C. J. Optically Generated Hyperpolarization for Sensitivity Enhancement in Solution-State NMR Spectroscopy. *Chem. Commun.* **2016**, *52*, 13221–13224.

11. Maly, T.; Debelouchina, G. T.; Bajaj, V. S.; Hu, K.-N.; Joo, C.-G.; Mak–Jurkauskas, M. L.; Sirigiri, J. R.; van der Wel, P. C. A.; Herzfeld, J.; Temkin, R. J.; et al. Dynamic Nuclear Polarization at High Magnetic Fields. *J. Chem. Phys.* **2008**, *128* (5), 052211.

12. Thurber, K. R.; Yau, W. M.; Tycko, R. Low-Temperature Dynamic Nuclear Polarization at 9.4 T with a 30 MW Microwave Source. *J. Magn. Reson.* **2010**, *204* (2), 303–313.

13. Becerra, L. R.; Gerfen, G. J.; Temkin, R. J.; Singel, D. J.; Griffin, R. G. Dynamic Nuclear Polarization with a Cyclotron Resonance Maser at 5 T. *Phys. Rev. Lett.* **1993**, *71* (21), 3561–3564.

14. Hall, D. A.; Maus, D. C.; Gerfen, G. J.; Inati, S. J.; Becerra, L. R.; Dahlquist, F. W.; Griffin, R. G. Polarization-Enhanced NMR Spectroscopy of Biomolecules in Frozen Solution. *Science.* **1997**, *276* (5314), 930–932.

15. Overhauser, A. W. Polarization of Nuclei in Metals. *Phys. Rev.* **1953**, *92* (2), 411.

16. Barnes, A. B.; Nannia, E. A.; Herzfeld, J.; Griffin, R. G.; Tempkin, R. J. A 250 GHz Gyrotron with a 3 GHz Tuning Bandwidth for Dynamic Nuclear Polarization Alexander. *J. Magn. Reson.* **2012**, *221*, 147–153.

17. Smith, A. N.; Caporini, M. A.; Fanucci, G. E.; Long, J. R. A Method for Dynamic Nuclear Polarization Enhancement of Membrane Proteins. *Angew. Chemie - Int. Ed.* **2015**, *54*, 1542–1546.

18. Franck, J. M.; Pavlova, A.; Scott, J. A.; Han, S. Quantitative Cw Overhauser Effect Dynamic Nuclear Polarization for the Analysis of Local Water Dynamics. *Prog. Nucl. Magn. Reson. Spectrosc.* **2013**, *74*, 33–56.

19. Bajaj, V. S.; Mak-Jurkauskas, M. L.; Belenky, M.; Herzfeld, J.; Griffin, R. G. Functional and Shunt States of Bacteriorhodopsin Resolved by 250 GHz Dynamic Nuclear Polarization-Enhanced Solid-State NMR. *Proc. Natl. Acad. Sci. U. S. A.* **2009**, *106* (23), 9244–9249.

20. Equbal, A.; Li, Y.; Leavesley, A.; Huang, S.; Rajca, S.; Rajca, A.; Han, S. Truncated Cross Effect Dynamic Nuclear Polarization: An Overhauser Effect Doppelgänger. *J. Phys. Chem. Lett.* **2018**, *9*, 2175–2180.

21. Lange, S.; Linden, A. H.; Akbey, Ü.; Trent Franks, W.; Loening, N. M.; Rossum, B. J. Van; Oschkinat, H. The Effect of Biradical Concentration on the Performance of DNP-MAS-NMR. *J. Magn. Reson.* **2012**, *216*, 209–212.

22. Mentink-Vigier, F.; Paul, S.; Lee, D.; Feintuch, A.; Hediger, S.; Vega, S.; De Paëpe, G. Nuclear Depolarization and Absolute Sensitivity in Magic-Angle Spinning Cross Effect Dynamic Nuclear Polarization. *Phys. Chem. Chem. Phys.* **2015**, *17* (34), 21824–21836.

23. Thurber, K. R.; Tycko, R. Perturbation of Nuclear Spin Polarizations in Solid State NMR of Nitroxide-Doped Samples by Magic-Angle Spinning without Microwaves. *J. Chem. Phys.* **2014**, *140* (18).

24. Corzilius, B.; Andreas, L. B.; Smith, A. A.; Ni, Q. Z.; Griffin, R. G. Paramagnet Induced Signal Quenching in MAS – DNP Experiments in Frozen Homogeneous Solutions. *J. Magn. Reson.* **2014**, *240*, 113–123.

25. Saliba, E. P.; Sesti, E. L.; Scott, F. J.; Albert, B. J.; Choi, E. J.; Alaniva, N.; Gao, C.; Barnes, A. B. Electron Decoupling with Dynamic Nuclear Polarization in Rotating Solids. *J. Am. Chem. Soc.* **2017**, *139* (18), 6310–6313.

26. Lee, D.; Bouleau, E.; Saint-Bonnet, P.; Hediger, S.; De Paëpe, G. Ultra-Low Temperature MAS-DNP. *J. Magn. Reson.* **2016**, *264*, 116–124.

27. Sesti, E. L.; Saliba, E. P.; Alaniva, N.; Barnes, A. B. Electron Decoupling with Cross Polarization and Dynamic Nuclear Polrization Below 6 K. *J. Magn. Reson.* **2018**, *295*, 1–5.

28. Frederick, K. K.; Michaelis, V. K.; Corzilius, B.; Ong, T. C.; Jacavone, A. C.; Griffin, R. G.; Lindquist, S. Sensitivity-Enhanced NMR Reveals Alterations in Protein Structure by Cellular Milieus. *Cell* **2015**, *163* (3), 620–628.

29. Latham, M. P.; Kay, L. E. Is Buffer a Good Proxy for a Crowded Cell-Like Environment? A Comparative NMR Study of Calmodulin Side-Chain Dynamics in Buffer and E . Coli Lysate. *PLoS One* **2012**, *7* (10), e48226.

30. Leavesley, A.; Wilson, C. B.; Sherwin, M.; Han, S. Effect of Water/Glycerol Polymorphism on Dynamic Nuclear Polarization. *Phys. Chem. Chem. Phys.* **2018**, *20*, 9897–9903.

31. Sesti, E. L.; Albert, B. J.; Gao, C.; Saliba, E. P.; Scott, F. J.; Sigurdsson, S. T.; Barnes, A. B. From the Bench Dynamic Nuclear Polarization NMR in Human Cells Using Fluorescent Polarizing Agents. *Biochemistry* **2018**, *57* (31), 4741–4746.

32. Trukhin, D. V.; Rogozhnikova, O. Y.; Troitskaya, T. I.; Kuzhelev, A. A.; Amosov, E.

V.; Halpern, H. J.; Koval', V. V.; Tormyshev, V. M. New Spin Probes: Tri- and Hexacationic Derivatives of Stable Tetrathiatriarylmethyl Radicals. *Russ. J. Org. Chem.* **2019**, *55* (3), 296–301.

33. Dhimitruka, I.; Grigorieva, O.; Zweier, J. L.; Khramtsov, V. V. Synthesis, Structure, and EPR Characterization of Deuterated Derivatives of Finland Trityl Radical. *Bioorganic Med. Chem. Lett.* **2010**, *20* (13), 3946–3949.

34. Geiger, M.-A.; Jagtap, A. P.; Kaushik, M.; Sun, H.; Stçppler, D.; Sigurdsson, S. T.; Corzilius, B.; Oschkinat, H. Efficiency of Water-Soluble Nitroxide Biradicals for Dynamic Nuclear Polarization in Rotating Solids at 9 . 4 T : BcTol-M and Cyolyl-TOTAPOL as New Polarizing Agents. *Chem. - A Eur. J.* **2018**, *24*, 13485–13494.

35. Scott, F. J.; Alaniva, N.; Golota, N. C.; Sesti, E. L.; Saliba, E. P.; Price, L. E.; Albert, B. J.; Chen, P.; O'Connor, R. D.; Barnes, A. B. A Versatile Custom Cryostat for Dynamic Nuclear Polarization Supports Multiple Cryogenic Magic Angle Spinning Transmission Line Probes. *J. Magn. Reson.* **2018**, *297*, 23–32.

36. Massiot, D.; Fayon, F.; Capron, M.; King, I.; Le Calvé, S.; Alonso, B.; Durand, J. O.; Bujoli, B.; Gan, Z.; Hoatson, G. Modelling One- and Two-Dimensional Solid-State NMR Spectra. *Magn. Reson. Chem.* **2002**, *40* (1), 70–76.

37. Scott, F. J.; Saliba, E. P.; Albert, B. J.; Alaniva, N.; Sesti, E. L.; Gao, C.; Golota, N. C.; Choi, E. J.; Jagtap, A. P.; Wittmann, J. J.; et al. Frequency-Agile Gyrotron for Electron Decoupling and Pulsed Dynamic Nuclear Polarization. *J. Magn. Reson.* **2018**, *289*, 45–54.

38. Sesti, E. L.; Alaniva, N.; Rand, P. W.; Choi, E. J.; Albert, B. J.; Saliba, E. P.; Scott, F. J.; Barnes, A. B. Magic Angle Spinning NMR below 6 K with a Computational Fluid Dynamics Analysis of Fluid Flow and Temperature Gradients. *J. Magn. Reson.* **2018**, *286*, 1–9.

39. Alaniva, N.; Saliba, E. P.; Sesti, E. L.; Judge, P. T.; Barnes, A. B. Electron Decoupling with Chirped Microwave Pulses for Rapid Signal Acquisition and Electron Saturation Recovery. *Angew. Chemie - Int. Ed.* **2019**.

40. Bouleau, E.; Saint-bonnet, P.; Mentink-vigier, F.; Takahashi, H.; Jacquot, J. F.; Bardet, M.; Aussenac, F.; Purea, A.; Engelke, F.; Hediger, S.; et al. Chemical Science Pushing NMR Sensitivity Limits Using Dynamic Nuclear Polarization with Closed-Loop Cryogenic Helium Sample Spinning. *Chem. Sci.* **2015**, *6*, 6806–6812.

Chapter 4: Frequency-Chirped Dynamic Nuclear Poalrization in Rotating Solids

Forward

This chapter is adapted from the paper "Characterization of Frequency-Chirped Dynamic Nuclear Polarization in Rotating Solids" by Patrick T. Judge*, Erika L. Sesti*, Nicholas Alaniva, Edward P. Saliba, Lauren E. Price, Chukun Gao, Thomas Halbritter, Snorri Th. Sigurdsson, George B. Kyei, and Alexander B. Barnes and describes work done to characterize newly applied frequency-chirped DNP on cross effect radicals, demonstrating their application in model systems and in intact human cells. Here, parameters such as sweep time, sweep width, center frequency, and electron Rabi frequency of the chirps are explored to determine their effect on frequency-chirped DNP experiments. Its effectiveness is demonstrated on a trityl-nitroxide biradical, TEMTriPol-1, and compared to a binitroxide radical, AMUPol. We demonstrate an improved sensitivity with TEMTriPol-1 in intact human cells with this new technique. These improvements will play an important role in future experiments involving in cell DNP NMR. Citation: Judge, P.T.*, Sesti, E.L., Alaniva, N., Saliba, E.P., Price, L.E., Gao, C., Halbritter, T., Sigurdsson, S.Th., Kyei, G.B., Barnes, A.B. Characterization of Frequency-Chirped Dynamic Nuclear Polarization in Rotating Solids. *J. Magn. Reson.* 2020, 313, 106702.

4.1 Overview

Continuous wave (CW) dynamic nuclear polarization (DNP) is used with magic angle spinning (MAS) to enhance the typically poor sensitivity of nuclear magnetic resonance (NMR) by orders of magnitude. In a recent publication we show that further enhancement is obtained by using a frequency-agile gyrotron to chirp incident microwave frequency through the electron resonance

frequency during DNP transfer. Here we characterize the effect of chirped MAS DNP by investigating the sweep time, sweep width, center-frequency, and electron Rabi frequency of the chirps. We show the advantages of chirped DNP with a trityl-nitroxide biradical, and a lack of improvement with chirped DNP using AMUPol, a nitroxide biradical. Frequency-chirped DNP on a model system of urea in a cryoprotecting matrix yields an enhancement of 142, 21% greater than that obtained with CW DNP. We then go beyond this model system and apply chirped DNP to intact human cells. In human Jurkat cells, frequency-chirped DNP improves enhancement by 24% over CW DNP. The characterization of the chirped DNP effect reveals instrument limitations on sweep time and sweep width, promising even greater increases in sensitivity with further technology development. These improvements in gyrotron technology, frequency-agile methods, and in-cell applications are expected to play a significant role in the advancement of MAS DNP.

4.2 Introduction

Dynamic nuclear polarization (DNP) is commonly used to improve the inherent insensitivity of nuclear magnetic resonance (NMR) spectroscopy[1–13]. Typically, only continuous wave (CW) microwave methods have been employed with magic angle spinning (MAS) DNP. The solid effect and the cross effect are the primary DNP mechanisms used in moderate magnetic field strengths of 5-14 Tesla (T)[14–18]. While CW approaches can significantly increase NMR sensitivity, they have limitations. Except in certain model systems[6,19,20], the solid effect and cross effect are inefficient at room temperature due to short longitudinal electron relaxation times. To perform CW DNP, samples are commonly cooled to <120 K, which adds complexity not only to the instrumentation, but also often leads to a loss of spectral resolution[14,21]. Arrested molecular motion at these temperatures can cause substantial line broadening in most samples[3,21–23]. The cross effect and solid effect also exhibit worse performance at higher magnetic field, with cross

effect efficiency decreasing as $1/B_0$ and that of solid effect as $1/B_0^2$[15,24,25]. Therefore new mechanisms will be required for efficient DNP at magnetic fields of 28 T and higher.

Frequency-chirped DNP techniques, such as the frequency-swept integrated solid effect (FS-ISE)[15,26], nuclear orientation via electron spin locking (NOVEL)[27,28], and time-optimized pulsed (TOP) DNP[29] show promise to perform well both at high magnetic field and room temperature. For instance, ISE yields DNP enhancements of ~150 at room temperature and is predicted to be unaffected by the strength of the external magnetic field [15].

However, these experiments have been performed without MAS and at magnetic fields <3 T[15,27,29], primarily due to the difficulty of implementing MAS with the microwave resonators required to generate considerable electron nutation frequencies. Frequency-swept DNP at higher magnetic fields has also been shown to improve DNP performance[30,31], but has only recently been implemented with MAS[32,33]. MAS improves the sensitivity and resolution of solid-state NMR[34–38] by partially averaging anisotropic interactions of the magnetic resonance Hamiltonian, and is a crucial aspect of applying DNP to systems of interest.

Here we characterize the behavior of frequency-chirped DNP experiments performed with MAS, expanding on our recent work[32]. We optimize frequency chirps from a custom-built frequency-agile high-power gyrotron[39] to produce large gains in intensity beyond those obtained with CW DNP. In addition to measuring its performance on a model system, we conduct optimized chirped experiments on intact human Jurkat cells to demonstrate frequency-chirped DNP in a biologically complex environment.

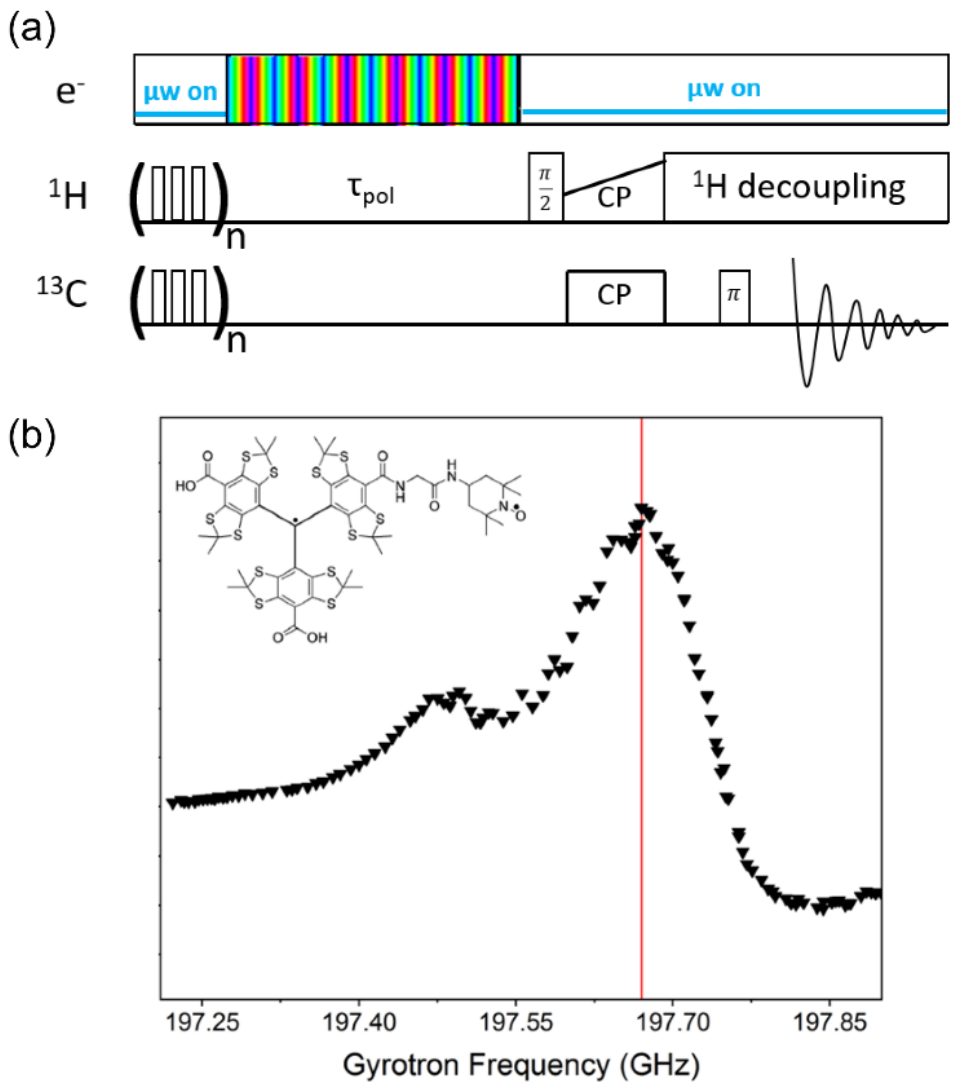

Fig. 1. Frequency-chirped DNP pulse sequence and ^{1}H enhancement profile of TEMTriPol-1. (**a**) The frequency-chirped DNP NMR pulse sequence. Triangular waveform frequency chirps (shown by the rainbow gradient) were applied over the polarization period (τ_{pol}), while CW irradiation was applied during the remainder of the experiment. (**b**) Enhancement profile of TEMTriPol-1 using CW DNP. CPMAS experiments were performed with a τ_{pol} of 3 s at varying microwave frequencies to record a ^{1}H enhancement profile of the TEMTriPol-1 radical (shown in upper left corner). The red line represents the peak of Trityl's EPR resonance (197.670 GHz)

as well as the center of the frequency chirps. This enhancement profile was adapted from Judge et al.[40]

4.3 Methods

4.3.1 NMR Experiments

MAS DNP NMR experiments were performed using a custom-built DNP spectrometer at a magnetic field of 7.1584 T[41]. ^{13}C and ^{1}H Larmor frequencies were 75.4937 MHz and 300.1790 MHz, respectively. A CPMAS, rotor synchronized, Hahn echo sequence with TPPM decoupling[42] was used for all experiments (Fig. 1a). The initial magnetization of ^{1}H and ^{13}C spins was destroyed using a saturation train. ^{1}H and ^{13}C pulses were performed with nutation frequencies of 77 kHz and 100 kHz, respectively. The Hartmann-Hahn matching condition (γB_1) for ^{1}H and ^{13}C was 30 kHz. Frequency chirps were applied over the DNP polarization period (τ_{pol}), and CW microwaves were employed over the rest of the experiment. The spinning frequency was 4.5 kHz for all experiments, and the sample temperature was 90 K. Typical polarization times (τ_{pol}) for optimized spectra were 5-times the T_1 of the sample in the absence of microwaves, in order to remove contamination of the data by differences in the nuclear T_1 and the T_{1DNP}.

Microwaves were generated using a frequency-agile gyrotron, whose output frequency was adjusted by varying the electron acceleration potential at the electron gun anode. An arbitrary waveform generator (AWG) integrated into the NMR spectrometer (Redstone, Tecmag Inc. Houston, TX) was used to generate a waveform, which ramped the output frequency of the gyrotron in a linear fashion through 197.670 GHz, the frequency of maximum DNP enhancement of the TEMTriPol-1 radical[39]. The frequency chirps were a triangular waveform, which was repeated over the entire polarization period. For frequency chirp optimization the incident microwave power, the center DNP microwave frequency, and the sweep width and sweep time of

the individual chirps were varied. The center frequency of the sweeps was varied by changing the voltage at the gyrotron anode with the AWG amplified by a high-voltage amplifier (TREK, Inc. Lockport, NY). The sweep width corresponded to the frequency range of one sweep/chirp (either up or down) in MHz, and sweep time was the time to complete a sweep/chirp. Microwave power was attenuated from full power by inserting copper foil with slits cut in it into a gap in the waveguide to partially pass the microwave beam. The optimal power of 7 W incident on the sample was used for most experiments, which provided an estimated electron Rabi frequency of 0.43 MHz[43].

The ^{13}C carbonyl resonance was fit using DMfit[44] to determine resulting enhancement increases. For all optimization spectra, the magnitude of the Hahn echo was used to calculate the percent increase in intensity. All experiments were repeated four times to acquire adequate error values for the measurements.

4.3.2 Sample Preparation

Experiments were performed on 4 M [U-^{13}C,^{15}N] urea mixed with 5 mM TEMTriPol-1 or 5 mM AMUPol in a cryoprotecting matrix consisting of 60% d8 glycerol, 30% D_2O, and 10% H_2O by volume. Intact Jurkat cells (ATCC, Manassas, VA) were cultured in [U-^{13}C, 98%; U-^{15}N, 98%] BioExpress-6000 mammalian cell growth medium (Cambridge Isotope Laboratories, Tewksbury, MA) at a concentration of 3×10^6 cells/mL in a six-well plate at 37°C and 5% CO_2 for 48 hr. 3.6×10^7 cells were collected, spun at 170 g for 5 min, washed with 1× phosphate-buffered saline (PBS), and spun again at 170 g for 5 min to remove extracellular NMR labels ($g = 9.8\ m/s^2$). 40 µL of 20 mM TEMTriPol-1 in 1×PBS with 10% DMSO was added to a cell pellet containing 36 million Jurkat cells. This suspension was centrifuged directly into the 3.2 mm zirconia rotor at 800 g for 30 s and immediately frozen in liquid nitrogen as detailed in our previous work [4].

4.4 Results and Discussion

Frequency-chirped DNP refers to a change in the microwave frequency or intensity throughout the course of an experiment. The frequency-chirped DNP pulse sequence is shown in Fig. 1A. Frequency chirps (represented by the rainbow gradient) are applied over the DNP polarization period and the resulting NMR signal is detected through a cross polarization (CP) Hahn echo sequence. We emphasize that microwave frequency chirps result in better manipulation of the electron spin polarization, yet the active DNP mechanism is still the cross effect.

Selection of appropriate radicals for frequency-chirped DNP is crucial due to drastic differences in electron spin g-anisotropy and relaxation properties. In our previous demonstrations of electron decoupling using chirped microwave pulses with MAS, we employed trityl rather than nitroxide radicals[3,22]. Those successes led us to explore the use of trityl-nitroxide biradicals, with the rationale that the narrow trityl resonance would be easier to manipulate and the tethered nitroxide would provide greater DNP enhancements through the cross effect mechanism. TEMTriPol-1 is such a biradical, consisting of a Finland trityl radical covalently linked to a 4-amino TEMPO radical, which is used for cross effect DNP[13,45]. TEMTriPol-1 improves cross effect efficiency at high magnetic fields. Where other biradicals, such as AMUPol, depolarize nuclear spins at 100 K in the absence of microwave irradiation, TEMTriPol-1 preserves nuclear polarization[5,46].

4.4.1 Frequency-chirped DNP on a Model System

CW DNP CPMAS experiments were performed at various microwave frequencies to record a ^{1}H DNP enhancement profile with TEMTriPol-1[40]. The enhancement profile shows the trityl resonance frequency as the optimal frequency for CW DNP enhancement. This will be the target for the center of the frequency chirps. In a 7.1584 T magnetic field, the microwave frequency for maximum CW DNP enhancement was 197.670 GHz (Fig. 1B).

Experiments were performed to determine the effect of frequency-chirped microwave pulses during the polarization period of MAS DNP (Fig. 2). For comparison, cross effect DNP experiments were performed with CW microwave irradiation. CW DNP experiments on a model system of urea with TEMTriPol-1 resulted in an enhancement of 118 (Fig. 2, red). Enhancements herein are defined as the NMR signal intensity recorded with DNP compared to that without DNP[46]. For frequency-chirped DNP experiments, the microwave frequency was linearly chirped with a triangular waveform over 197.670 GHz, with a 28 μs sweep time and a 120 MHz sweep width. These optimized chirps yielded a 21% increase over CW DNP and an enhancement of 142 (Fig. 2, blue). Polarization times of 53 s ($5\times T_{1DNP}$, Fig. S1) were used to ensure that >99% of the polarization had built up for both experiments, allowing for direct comparison of the CW and frequency-chirped experiments.

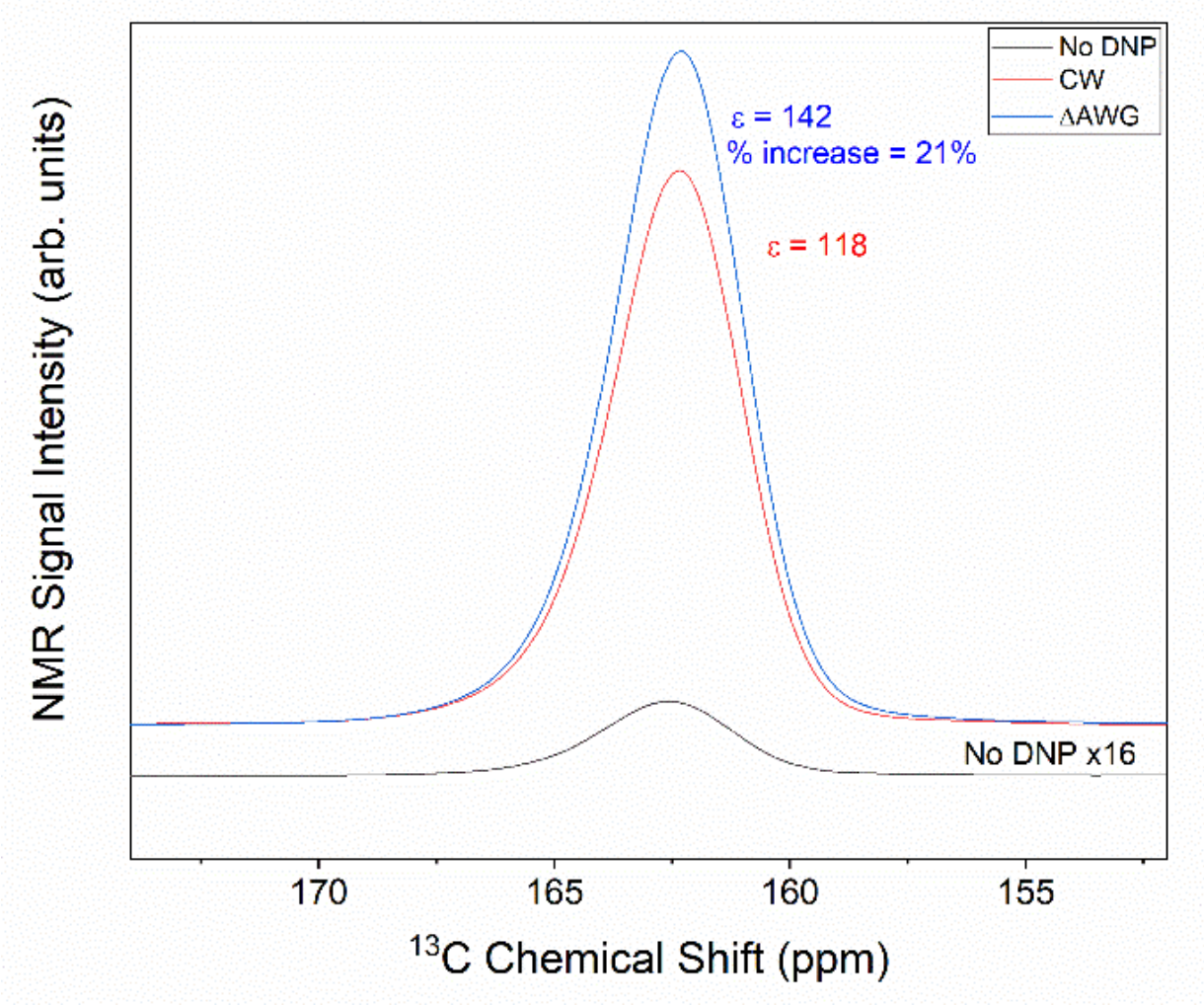

Fig. 2. Frequency-chirped DNP with TEMTriPol-1. Comparison of DNP spectra with triangular frequency sweeps (blue) and CW (red) microwave irradiation using 7 W of microwave power incident on the sample. The spectrum with no microwave irradiation is shown in black. The triangular frequency chirps generated an increase of 21% over CW DNP. The DNP polarization period for all three experiments was 53 s, the sweep width was 120 MHz, and the sweep time was 28 μs.

To determine the necessity of a narrow-line radical, such as trityl, for frequency-chirped DNP, experiments were performed on a sample containing the nitroxide-nitroxide biradical, AMUPol.

The frequency chirps were centered at 197.674 GHz (maximum with ^{1}H-enhancement for AMUPol) the previously optimized sweep time of 28 μs and sweep width of 120 MHz were used. Frequency chirps over the polarization period resulted in a decrease in signal intensity of 3% compared to CW DNP (Fig. 3). These frequency chirps do not yield the same improved electron spin control over the nitroxide biradical, AMUPol, as they do over TEMTriPol-1. This implies that a narrow-line radical is required for implementation of frequency-chirped DNP.

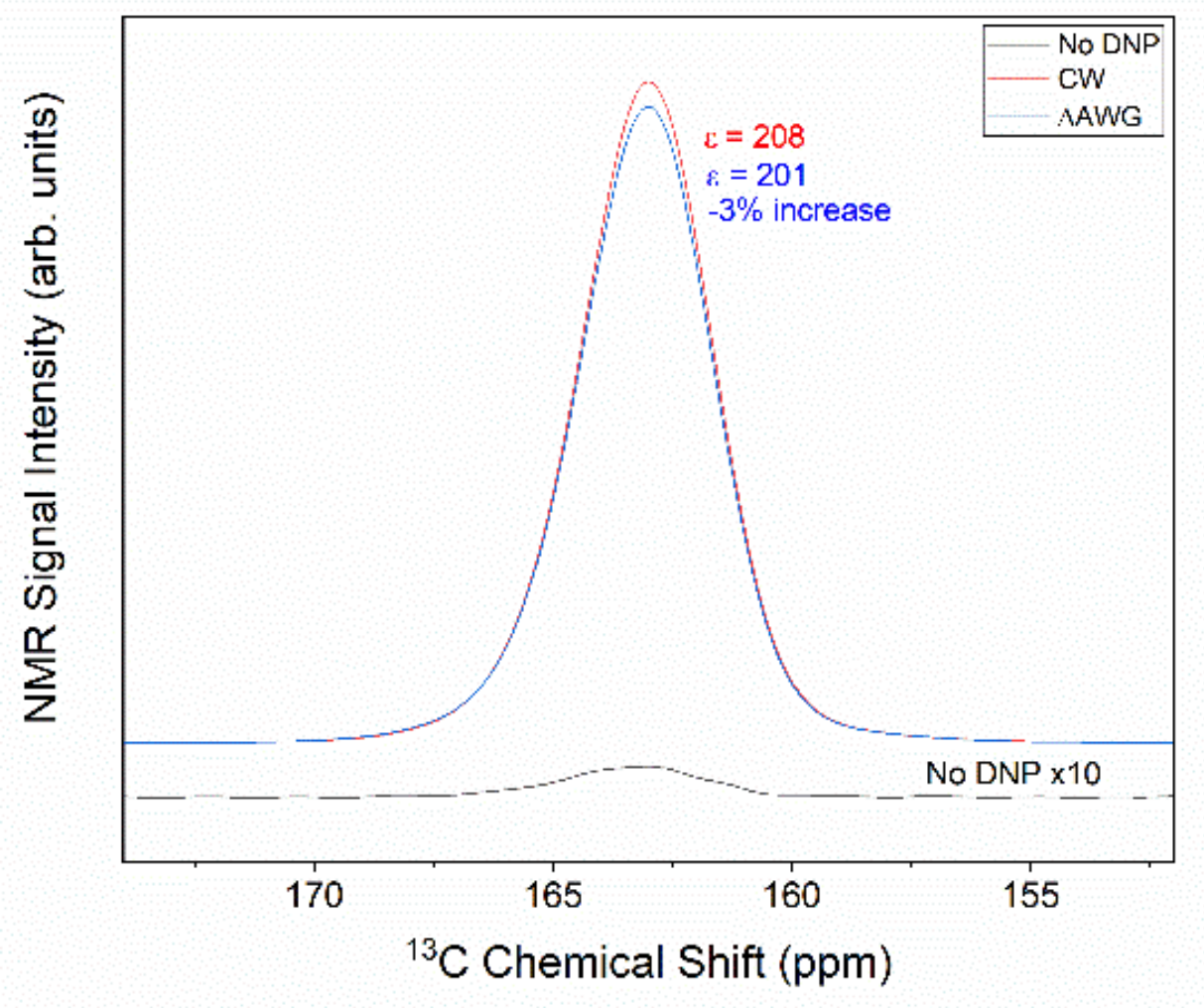

Fig. 3. Frequency-chirped DNP with AMUPol. The polarization time was 47 s with a sweep time of 28 μs and sweep width of 120 MHz centered at 197.674 GHz. Frequency chirps (blue)

decreased the signal intensity by 3% compared to CW (red), providing an enhancement of 201 compared to an experiment with no microwaves incident on the sample (black).

4.4.2 Frequency-chirped DNP in Intact Jurkat Cells

The performance of frequency-chirped DNP was then examined within intact human Jurkat cells (Fig. 4). Frequency chirps improved the NMR signal by 24%, yielding an enhancement of 6 (versus 4.8 for CW DNP). These results display the application of frequency-chirped DNP to more complex samples of biological interest.

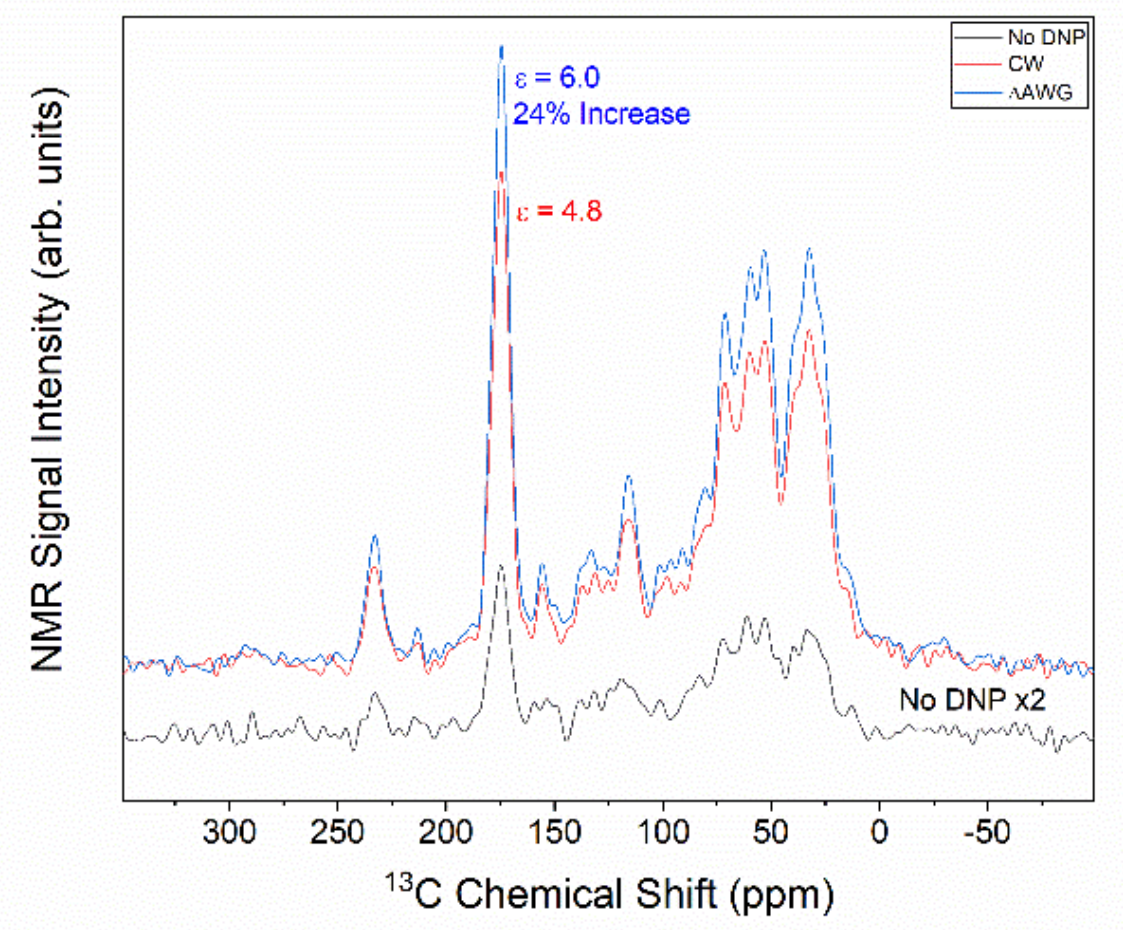

Fig. 4. Frequency-chirped MAS DNP in intact human cells. The polarization time was 10 s ($5\times T_{1DNP}$, Fig. S1). Frequency chirps (blue) resulted in a 24% improvement in overall signal

intensity compared to CW (red) and enhanced the NMR signal by 6 times compared to signal without DNP (black).

4.4.3 Power Dependence of CW and Frequency-chirped DNP

To determine the dependence of CW and frequency-chirped enhancement on microwave power, CPMAS experiments were performed with varying microwave attenuation on the TEMTriPol-1/urea sample (Fig. 5). For frequency-chirped DNP the optimized triangle waveform (28 μs sweep time and 120 MHz sweep width) was repeated over a polarization time of 20 s. 35 W of microwave power incident on the sample (Rabi frequency of 0.95 MHz) produced a 123% increase in signal with frequency-chirped DNP compared to CW, yielding enhancements of 17 and 8, respectively (Fig. 5a, b). We note that such high microwave powers place the cross effect in the oversaturated regime, leading to less overall enhancement.

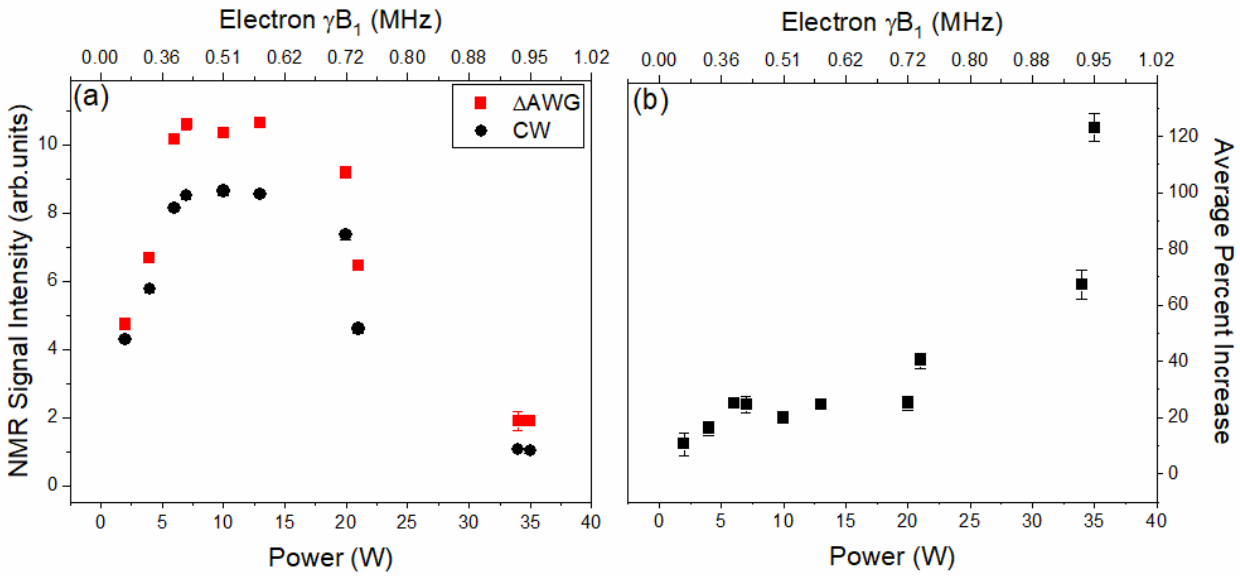

Fig. 5. Frequency-chirped DNP microwave power dependence. (**a**) Dependence of signal enhancement on incident microwave power, with and without frequency chirps. (**b**) Effect of microwave power on average percent increase in signal area with frequency chirps over CW.

7 W of microwave power resulted in the highest sensitivity and an improvement of 25% with frequency-chirped DNP compared to CW. Higher microwave power yielded greater improvements with frequency-chirped DNP over CW DNP, but the overall signal intensity obtained was suboptimal due to saturation of the cross effect[47].

4.4.4 Characterization of Frequency-chirped DNP

The effects of sweep time, sweep width, and center frequency on the improvement with frequency-chirped DNP over CW irradiation are shown in Fig. 6. For this dependence the polarization time was 20 s; the sweep width was held constant at 80 MHz, the incident microwave power at 7 W, and the center frequency at 197.670 GHz. Shorter sweep times increased the sensitivity to a greater extent than longer sweep times, with the greatest improvement over CW (15%) occurring with a 20 μs sweep time (Fig. 6a). Sweep times below 20 μs were not achievable with the current microwave frequency agility circuit, as the frequency output waveform became distorted. A sweep time of 150 μs resulted in only a 1% improvement in signal intensity over CW. We suspect that at longer sweep times electron spin saturation is lost through relaxation mechanisms.

The dependence of frequency-chirped DNP sensitivity on the sweep width of the frequency chirps is shown in Fig. 6b. For this dependence the polarization time was 20 s; the sweep time was held constant at 28 μs, the incident microwave power at 7 W, and the center frequency at 197.670 GHz. The improvement from the frequency chirps increased as the sweep width increased. A 120 MHz sweep width resulted in an improvement of 21%, while the signal intensity decreased by 1% with a sweep width of 10 MHz. Due to instrument limitations, sweep widths greater than 120 MHz could not be attained. This width is roughly that of the base of the trityl lineshape in the enhancement profile (Fig. 1b). We previously reported a similar optimal sweep width in electron decoupling experiments involving the Finland trityl radical[3]. Larger sweep widths provide

microwave irradiation that is resonant with a greater number of trityl electron spins, enabling better electron spin control and improving the efficiency of frequency-chirped DNP.

During characterization it is important to consider multiple points on the enhancement profile. Fig. 6d provides a clear picture of the effect of frequency chirping, whereas Fig. 6c shows the potential for misinformation. The choice of irradiation frequency can lead to suspiciously high improvements due to difference in positive and negative enhancement regions between CW and frequency-chirped DNP. The CW enhancement profile shows maximum positive and negative enhancements at 197.670 GHz and 197.850 GHz, respectively (Fig. 6d). Frequency chirping at microwave frequencies lower than 197.750 GHz (positive enhancement), yielded greater enhancements than CW (Fig. 6d). However, at frequencies greater than 197.750 GHz (negative enhancement), the frequency-chirped DNP provided lower signal intensity than CW DNP.

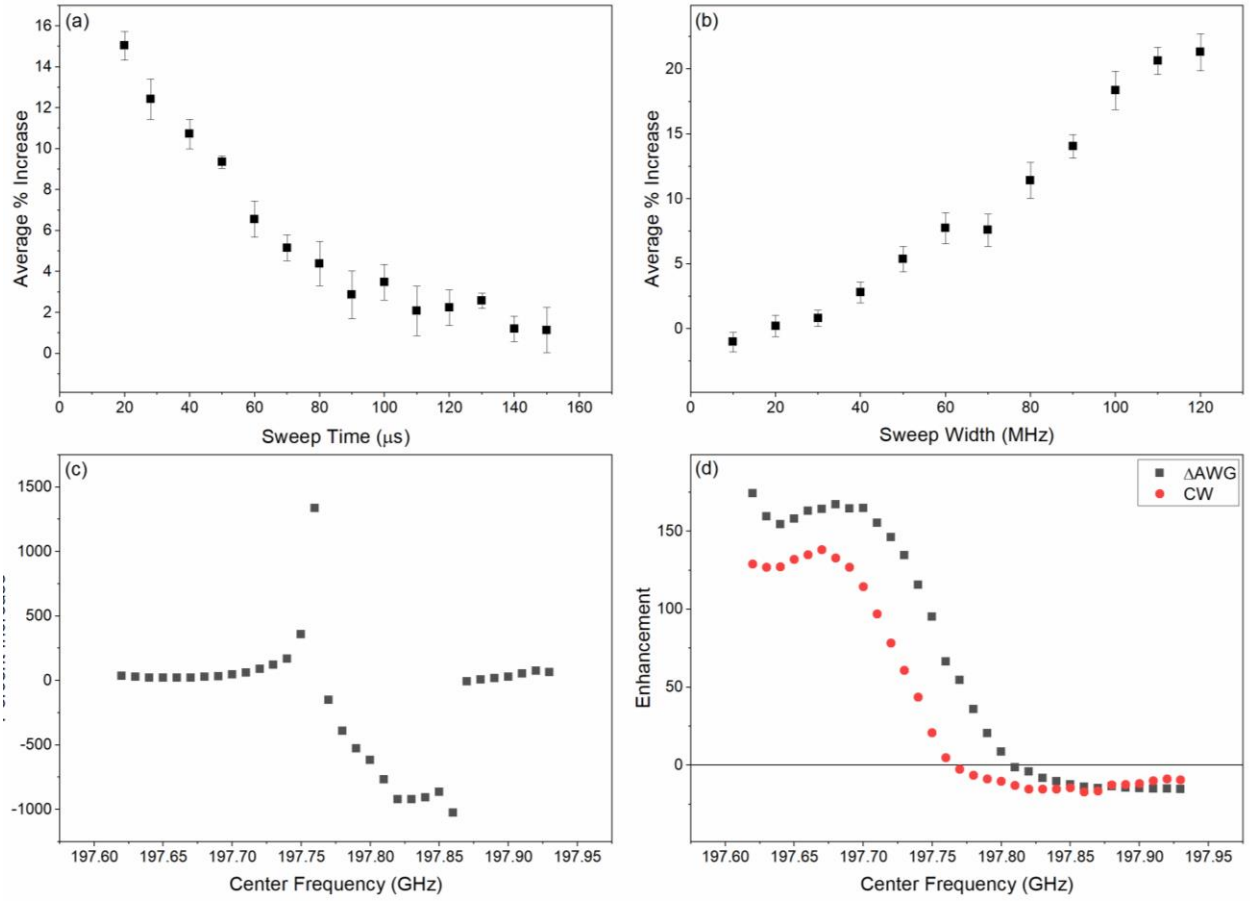

Fig. 6. Experimental parameter optimization for frequency-chirped DNP on urea with TEMTriPol-1. (**a**) Sweep time dependence using a 80 MHz sweep width centered at a gyrotron frequency of 197.670 GHz. (**b**) Sweep width dependence using a 28 μs sweep time centered at 197.670 GHz. (**c**) The percent increase of frequency-chirped DNP over CW DNP, using the points from the enhancement profile in (**d**). The order-of-magnitude larger increases/decreases are due to the different positive/negative enhancement crossing points for the two methods. (**d**) Enhancement profiles for CW DNP (red) and frequency-chirped DNP (black). A 20 s polarization time was used for all experiments.

Note that at this point we have simply demonstrated the methodology of performing frequency-chirped DNP experiments with TEMTriPol-1. To compare the sensitivity of the experiments with TEMTriPol-1 and AMUPol, we can divide the signal-to-noise from each experiment by the square root of the polarization time for the respective experiments. In doing so, we obtain a sensitivity of 79 with AMUPol (Fig. 3) and 73 with TEMTriPol-1 (Fig. 2). Thus, while the sensitivity of the experiments performed on each radical are similar at this stage, advances in instrumentation that enable greater sweep times and sweep widths will make frequency-chirped DNP experiments with TEMTriPol-1 more sensitive than AMUPol, and thus more feasible for sensitivity-demanding, multidimensional experiments.

4.5 Conclusions and Outlook

To date, frequency-chirped DNP experiments, such as FS-ISE, NOVEL, and TOP DNP, have been largely restricted to static samples due to the difficulties of housing microwave resonators with the instrumentation required for magic angle spinning (MAS). Here, we have characterized the optimal experimental conditions for frequency-chirped MAS DNP. At a magnetic field of 7 T and with 7 W of microwave power, frequency-chirped microwaves over the polarization period

improved DNP enhancements by 21%. Greater microwave powers resulted in up to 123% improvements with frequency-chirped DNP, but saturation of the cross effect resulted in less overall signal intensity.

These optimized frequency-chirped experiments were applied to a more biologically complex sample: intact Jurkat cells. This resulted in an improvement in signal intensity of 24% over CW DNP. Characterization of the parameters of frequency-chirped DNP revealed areas for further improvements to elicit even greater sensitivity. More powerful gyrotrons with larger frequency bandwidths, and gating mechanisms for chirps can be developed to increase sweep widths and shorten the sweep times, thus improving electron spin control. To take full advantage of frequency-chirped DNP at high power and high electron Rabi frequencies, duty cycling of the microwaves can be implemented to reduce dielectric heating[29]. We expect optimization of the waveform, with respect to both intensity and phase, to result in improved frequency-chirped DNP MAS performance. Future studies could analyze the effect of the spinning frequency on the enhancement achieved by frequency chirped DNP over CW DNP. Both the solid effect and cross effect are driven by interactions between the spin system, the microwave field, and the spinning rotor. Understanding these effects will prove crucial in the future development of DNP, as MAS frequencies and magnetic fields are pushed to ever higher values.

New radicals composed of tethered broad and narrow line radicals are currently being investigated with useful electronic properties such as long longitudinal relaxation times. Longer relaxation times will afford even more electron spin control with frequency-chirped DNP. Although the precise mechanism governing the improvement in sensitivity will require further investigation, it is possible that it is governed by an adiabatic process. As such, future experiments could focus on maintaining a constant sweep rate by simultaneously varying the sweep time and sweep width in

an inverse manner. This could prove important, as adiabatic processes often show a remarkable resilience to microwave inhomogeneities and frequency offsets arising from difference in molecular orientation and conformations in a solid sample. These techniques can be paired with other advances in instrumentation such as higher power microwave sources and microwave lenses for improved microwave intensity and high frequency MAS for ^{1}H detected spectra in future experiments. These could allow for the implementation of pulsed DNP mechanisms such as electron-nuclear cross polarization at high magnetic fields in the foreseeable future.

4.6 Acknowledgements

The research reported in this publication was supported by an NIH Director's New Innovator Award [grant number DP2GM119131], an NSF CAREER Award [grant number DBI-1553577], a Camille Dreyfus Teacher-Scholar Award, a Deutsche Forschungsgemeinschaft (DFG) Postdoctoral Fellowship [414196920], and the University of Iceland Research Fund. We also thank Faith Scott and Sarah Overall for helpful discussions.

Author Contributions:

- Design and planning of experiments was a collaboration between Patrick Judge, Erika Sesti, Nicholas Alaniva, Edward Saliba, Chukun Gao, and Alexander Barnes
- Preparation of intact human cells was designed and carried out by Lauren Price and George Kyei
- Experiments and analysis were carried out by Patrick Judge and Erika Sesti
- TEMTriPol-1 synthesis was performed by Thomas Halbritter and Snorri Sigurdsson
- Manuscript was written and compiled as a collaboration between Patrick Judge, Erika Sesti, and Alexander Barnes

4.7 References

1. A.W. Overhauser, Polarization of Nuclei in Metals, Phys. Rev. 92 (1953) 411–415.

2. T.R. Carver, C.P. Slichter, Polarization of nuclear spins in metals, Phys. Rev. 92 (1953) 212–213. doi:10.1103/PhysRev.92.212.2.

3. E.P. Saliba, E.L. Sesti, F.J. Scott, B.J. Albert, E.J. Choi, N. Alaniva, C. Gao, A.B. Barnes, Electron Decoupling with Dynamic Nuclear Polarization in Rotating Solids, J. Am. Chem. Soc. 139 (2017) 6310–6313. doi:10.1021/jacs.7b02714.

4. B.J. Albert, C. Gao, E.L. Sesti, E.P. Saliba, N. Alaniva, F.J. Scott, S.T. Sigurdsson, A.B. Barnes, Dynamic Nuclear Polarization Nuclear Magnetic Resonance in Human Cells Using Fluorescent Polarizing Agents, Biochemistry. 57 (2018) 4741–4746. doi:10.1021/acs.biochem.8b00257.

5. A. Zagdoun, G. Casano, O. Ouari, M. Schwarzwälder, A.J. Rossini, F. Aussenac, M. Yulikov, G. Jeschke, C. Copéret, A. Lesage, P. Tordo, L. Emsley, Large molecular weight nitroxide biradicals providing efficient dynamic nuclear polarization at temperatures up to 200 K, J. Am. Chem. Soc. 135 (2013) 12790–12797. doi:10.1021/ja405813t.

6. L.R. Becerra, G.J. Gerfen, R.J. Temkin, D.J. Singel, R.G. Griffin, Dynamic nuclear polarization with a cyclotron resonance maser at 5 T, Phys. Rev. Lett. 71 (1993) 3561–3564. doi:10.1103/PhysRevLett.71.3561.

7. T. Kobayashi, F.A. Perras, I.I. Slowing, A.D. Sadow, M. Pruski, Dynamic Nuclear Polarization Solid-State NMR in Heterogeneous Catalysis Research, ACS Catal. 5 (2015) 7055–7062. doi:10.1021/acscatal.5b02039.

8. D.J. Kubicki, A.J. Rossini, A. Purea, A. Zagdoun, O. Ouari, P. Tordo, F. Engelke, A. Lesage, L. Emsley, Amplifying dynamic nuclear polarization of frozen solutions by incorporating dielectric particles, J. Am. Chem. Soc. 136 (2014) 15711–15718. doi:10.1021/ja5088453.

9. T.V. Can, M.A. Caporini, F. Mentink-Vigier, B. Corzilius, J.J. Walish, M. Rosay, W.E. Maas, M. Baldus, S. Vega, T.M. Swager, R.G. Griffin, Overhauser effects in insulating solids, J. Chem. Phys. 141 (2014) 064202. doi:10.1063/1.4891866.

10. A.N. Smith, M.A. Caporini, G.E. Fanucci, J.R. Long, A method for dynamic nuclear polarization enhancement of membrane proteins, Angew. Chemie - Int. Ed. 54 (2015) 1542–1546. doi:10.1002/anie.201410249.

11. B.J. Wylie, B.G. Dzikovski, S. Pawsey, M. Caporini, M. Rosay, J.H. Freed, A.E. McDermott, Dynamic nuclear polarization of membrane proteins: Covalently bound spin-labels at protein-protein interfaces, J. Biomol. NMR. 61 (2015) 361–367. doi:10.1007/s10858-015-9919-6.

12. A.B. Barnes, E.A. Nanni, J. Herzfeld, R.G. Griffin, R.J. Temkin, A 250 GHz gyrotron with a 3 GHz tuning bandwidth for dynamic nuclear polarization, J. Magn. Reson. 221 (2012) 147–153. doi:10.1016/j.jmr.2012.03.014.

13. F. Mentink-Vigier, G. Mathies, Y. Liu, A.-L. Barra, M.A. Caporini, D. Lee, S. Hediger, R. G. Griffin, G. De Paëpe, Efficient cross-effect dynamic nuclear polarization without depolarization in high-resolution MAS NMR, Chem. Sci. (2017). doi:10.1039/C7SC02199B.

14. E.P. Saliba, E.L. Sesti, N. Alaniva, A.B. Barnes, Pulsed Electron Decoupling and Strategies for Time Domain Dynamic Nuclear Polarization with Magic Angle Spinning, J. Phys. Chem. Lett. 9 (2018) 5539–5547. doi:10.1021/acs.jpclett.8b01695.

15. T. V. Can, R.T. Weber, J.J. Walish, T.M. Swager, R.G. Griffin, Frequency-Swept Integrated Solid Effect, Angew. Chemie - Int. Ed. 56 (2017) 6744–6748. doi:10.1002/anie.201700032.

16. K.R. Thurber, R. Tycko, Theory for cross effect dynamic nuclear polarization under magic-angle spinning in solid state nuclear magnetic resonance: The importance of level crossings, J. Chem. Phys. 137 (2012). doi:10.1063/1.4747449.

17. X. Wang, B.G. Caulkins, G. Riviere, L.J. Mueller, F. Mentink-Vigier, J.R. Long, Direct dynamic nuclear polarization of 15 N and trityl radical and magic angle spinning C spins at 14 . 1 T using a trityl radical and magic angle spinning, 100 (2019) 85–91. doi:10.1016/j.ssnmr.2019.03.009.

18. A.S. Lilly Thankamony, J.J. Wittmann, M. Kaushik, B. Corzilius, Dynamic nuclear polarization for sensitivity enhancement in modern solid-state NMR, Prog. Nucl. Magn. Reson. Spectrosc. 102–103 (2017) 120–195. doi:10.1016/j.pnmrs.2017.06.002.

19. M. Lelli, S.R. Chaudhari, D. Gajan, G. Casano, A.J. Rossini, O. Ouari, P. Tordo, A. Lesage, L. Emsley, Solid-State Dynamic Nuclear Polarization at 9.4 and 18.8 T from 100 K to Room Temperature, J. Am. Chem. Soc. 137 (2015) 14558–14561. doi:10.1021/jacs.5b08423.

20. M. Afeworki, R.A. McKay, J. Schaefer, Selective Observation of the Interface of Heterogeneous Polycarbonate/Polystyrene Blends by Dynamic Nuclear Polarization Carbon-13 NMR Spectroscopy, Macromolecules. 25 (1992) 4084–4091. doi:10.1021/ma00042a006.

21. A.B. Barnes, B. Corzilius, M.L. Mak–Jurkauskas, L.B. Andreas, V.S. Bajaj, Y. Matsuki, M.L. Belenky, J. Lugtenburg, J.R. Sirigiri, R.J. Temkin, J. Herzfeld, R.G. Griffin, Resolution and polarization distribution in cryogenic DNP/MAS experiments, Phys. Chem. Chem. Phys. 12 (2010) 5741–5751. doi:10.1039/c002146f.

22. E.L. Sesti, E.P. Saliba, N. Alaniva, A.B. Barnes, Electron Decoupling with Cross Polarization and Dynamic Nuclear Polrization Below 6 K, J. Magn. Reson. 295 (2018) 1–5. doi:10.1016/J.JMR.2018.07.016.

23. A.B. Siemer, K.Y. Huang, A.E. McDermott, Protein Linewidth and Solvent Dynamics in Frozen Solution NMR, PLoS One. 7 (2012). doi:10.1371/journal.pone.0047242.

24. B. Corzilius, Theory of solid effect and cross effect dynamic nuclear polarization with half-integer high-spin metal polarizing agents in rotating solids, Phys. Chem. Chem. Phys. 18 (2016) 27190–27204. doi:10.1039/c6cp04621e.

25. T. Maly, G.T. Debelouchina, V.S. Bajaj, K.-N. Hu, C.-G. Joo, M.L. Mak–Jurkauskas, J.R. Sirigiri, P.C.A. van der Wel, J. Herzfeld, R.J. Temkin, R.G. Griffin, Dynamic nuclear polarization at high magnetic fields, J. Chem. Phys. 128 (2008) 052211. doi:10.1063/1.2833582.

26. A. Henstra, P. Dirksen, W.T. Wenckebach, Enhanced dynamic nuclear polarization by the integrated solid effect, Phys. Lett. A. 134 (1988) 134–136. doi:10.1016/0375-9601(88)90950-4.

27. T.V. Can, J.J. Walish, T.M. Swager, R.G. Griffin, Time domain DNP with the NOVEL sequence, J. Chem. Phys. 143 (2015) 1–8. doi:10.1063/1.4927087.

28. A. Henstra, P. Dirksen, J. Schmidt, W.T. Wenckebach, Nuclear Spin Orientation via Electron Spin Locking (NOVEL), J. Magn. Reson. 77 (1988) 389–393. doi:10.1016/0022-2364(88)90190-4.

29. K.O. Tan, C. Yang, R.T. Weber, G. Mathies, R.G. Griffin, Time-optimized pulsed dynamic nuclear polarization, Sci. Adv. 5 (2019) 1–8. doi:10.1126/sciadv.aav6909.

30. I. Kaminker, S. Han, Amplification of Dynamic Nuclear Polarization at 200 GHz by Arbitrary Pulse Shaping of the Electron Spin Saturation Profile, J. Phys. Chem. Lett. 9 (2018) 3110–3115. doi:10.1021/acs.jpclett.8b01413.

31. A. Bornet, J. Milani, B. Vuichoud, A.J. Perez Linde, G. Bodenhausen, S. Jannin, Microwave frequency modulation to enhance Dissolution Dynamic Nuclear Polarization Dedicated to To Martial Rey, as a token of appreciation., Chem. Phys. Lett. 602 (2014) 63–67. doi:10.1016/j.cplett.2014.04.013.

32. C. Gao, N. Alaniva, E.P. Saliba, E.L. Sesti, P.T. Judge, F.J. Scott, T. Halbritter, S.T. Sigurdsson, A.B. Barnes, Frequency-chirped Dynamic Nuclear Polarization with Magic Angle Spinning Using a Frequency-agile Gyrotron, J. Magn. Reson. 308 (2019) 106586. doi:10.1016/j.jmr.2019.106586.

33. A. EQUBAL, K. Tagami, S. Han, Pulse Shaped Dynamic Nuclear Polarization Under Magic Angle Spinning, (2019). doi:10.26434/chemrxiv.9788471.v1.

34. V.S. Bajaj, M.L. Mak-Jurkauskas, M. Belenky, J. Herzfeld, R.G. Griffin, Functional and shunt states of bacteriorhodopsin resolved by 250 GHz dynamic nuclear polarization-enhanced solid-state NMR, Proc. Natl. Acad. Sci. U. S. A. 106 (2009) 9244–9249. doi:10.1073/pnas.0900908106.

35. R.W. Martin, R.C. Jachmann, D. Sakellariou, U.G. Nielsen, A. Pines, High-resolution nuclear magnetic resonance spectroscopy of biological tissues using projected magic angle spinning, Magn. Reson. Med. 54 (2005) 253–257. doi:10.1002/mrm.20585.

36. W. Tang, A. Bhatt, A.N. Smith, P.J. Crowley, L.J. Brady, J.R. Long, Specific binding of a naturally occurring amyloidogenic fragment of Streptococcus mutans adhesin P1 to intact P1 on the cell surface characterized by solid state NMR spectroscopy, J. Biomol. NMR. 64 (2016) 153–164. doi:10.1007/s10858-016-0017-1.

37. S.H. Werby, L. Cegelski, Spectral comparisons of mammalian cells and intact organelles by solid-state NMR, J. Struct. Biol. 206 (2019) 49–54. doi:10.1016/j.jsb.2018.05.007.

38. R. Gupta, H. Zhang, M. Lu, G. Hou, M. Caporini, M. Rosay, W. Maas, J. Struppe, J. Ahn, I.J.L. Byeon, H. Oschkinat, K. Jaudzems, E. Barbet-Massin, L. Emsley, G. Pintacuda, A. Lesage, A.M. Gronenborn, T. Polenova, Dynamic Nuclear Polarization Magic-Angle Spinning Nuclear Magnetic Resonance Combined with Molecular Dynamics Simulations Permits Detection of Order and Disorder in Viral Assemblies, J. Phys. Chem. B. 123 (2019) 5048–5058. doi:10.1021/acs.jpcb.9b02293.

39. F.J. Scott, E.P. Saliba, B.J. Albert, N. Alaniva, E.L. Sesti, C. Gao, N.C. Golota, E.J. Choi, A.P. Jagtap, J.J. Wittmann, M. Eckardt, W. Harneit, B. Corzilius, S. Th. Sigurdsson, A.B. Barnes, Frequency-agile gyrotron for electron decoupling and pulsed dynamic nuclear polarization, J. Magn. Reson. 289 (2018) 45–54. doi:10.1016/j.jmr.2018.02.010.

40. P.T. Judge, E.L. Sesti, E.P. Saliba, N. Alaniva, T. Halbritter, S.T. Sigurdsson, A.B. Barnes, Sensitivity Analysis of Magic Angle Spinning Dynamic Nuclear Polarization Below 6 K, J. Magn. Reson. (2019). doi:10.1016/j.jmr.2019.05.011.

41. F.J. Scott, N. Alaniva, N.C. Golota, E.L. Sesti, E.P. Saliba, L.E. Price, B.J. Albert, P. Chen, R.D. O'Connor, A.B. Barnes, A Versatile Custom Cryostat for Dynamic Nuclear Polarization Supports Multiple Cryogenic Magic Angle Spinning Transmission Line Probes, J. Magn. Reson. 297 (2018) 23–32. doi:10.1016/J.JMR.2018.10.002.

42. C.M. Rienstra, A.E. Bennett, R.G. Griffin, K. V. Lakshmi, M. Auger, Heteronuclear decoupling in rotating solids, J. Chem. Phys. 103 (2002) 6951–6958. doi:10.1063/1.470372.

43. D.E.M. Hoff, B.J. Albert, E.P. Saliba, F.J. Scott, E.J. Choi, M. Mardini, A.B. Barnes, Frequency swept microwaves for hyperfine decoupling and time domain dynamic nuclear polarization, Solid State Nucl. Magn. Reson. 72 (2015) 79–89. doi:10.1016/j.ssnmr.2015.10.001.

44. D. Massiot, F. Fayon, M. Capron, I. King, S. Le Calvé, B. Alonso, J.O. Durand, B. Bujoli, Z. Gan, G. Hoatson, Modelling one- and two-dimensional solid-state NMR spectra, Magn. Reson. Chem. 40 (2002) 70–76. doi:10.1002/mrc.984.

45. G. Mathies, M.A. Caporini, V.K. Michaelis, Y. Liu, K.N. Hu, D. Mance, J.L. Zweier, M. Rosay, M. Baldus, R.G. Griffin, Efficient Dynamic Nuclear Polarization at 800 MHz/527

GHz with Trityl-Nitroxide Biradicals, Angew. Chemie - Int. Ed. 54 (2015) 11770–11774. doi:10.1002/anie.201504292.

46. F. Mentink-Vigier, S. Paul, D. Lee, A. Feintuch, S. Hediger, S. Vega, G. De Paëpe, Nuclear depolarization and absolute sensitivity in magic-angle spinning cross effect dynamic nuclear polarization, Phys. Chem. Chem. Phys. 17 (2015) 21824–21836. doi:10.1039/C5CP03457D.

47. T.A. Siaw, M. Fehr, A. Lund, A. Latimer, S.A. Walker, D.T. Edwards, S.I. Han, Effect of electron spin dynamics on solid-state dynamic nuclear polarization performance, Phys. Chem. Chem. Phys. 16 (2014) 18694–18706. doi:10.1039/c4cp02013h.

Chapter 5: Interactions between Cholesterol and the C1b Regulatory domain of PKC-δ in the Presence of Modulating Ligands

Forward

Molecular dynamics is a powerful tool capable of studying the structure and dynamics of proteins with atomistic detail. Here, molecular dynamics simulations are used to examine the C1b regulatory domain of PKC-δ when bound to a range of modulating ligands. Phorbol and bryostatin are known modulators that bind to the same region of the C1b domain and with similar affinity yet elicit vastly different cellular effects. To date, the reasoning behind these different cellular responses is not known. In this chapter, this problem is investigated from the angle of how the complexes interact with the membrane in which they are embedded. Through simulations of the complexes in a heterogeneous membrane mimicking that which would be observed in a cellular environment, it is shown that bryostatin- and phorbol-bound complexes interact with cholesterol to different extents. These interactions appear to be determined by membrane insertion depth and tilt angle, exposing more backbone residues for hydrogen bonding with membrane cholesterol. This result suggests that the signaling differences between byrostatin and phorbol could be due to altered localization in membrane microdomains, and therefore, different access to substrates for subsequent phosphorylation. This hypothesis is tested by comparing these results to simulations involving the C1b domain bound to a bryostatin analogue – Merle27. Combined with the previous chapters, a plan for investigating the differences between the bryostatin- and phorbol-bound complexes by MAS DNP-NMR *in vitro* is proposed.

5.1 Overview

Protein kinase C, belonging to the family of serine/threonine kinases, is a widely studied kinase involved in many important signaling transduction pathways. As such, it is a therapeutic target for a wide range of diseases including cancer, cardiovascular diseases, HIV/AIDS, and Alzheimer's. Two classes of ligands, phorbol esters and bryostatin, are known modulators of PKC-δ through binding to the C1b regulatory domain. Bryostatin is a potential therapeutic currently undergoing clinical trials for Alzheimer's and HIV/AIDS, while phorbol esters are known to be tumor promoters, despite both ligands binding to the same site with similar affinity. To date, it is still unknown why these ligands elicit such contrasting effects in the cell. Here molecular dynamics simulations are used to investigate the structure and intermolecular interactions of these ligands bound to the C1b regulatory domain of PKC-δ and with heterogeneous membranes. Notably, the C1b-phorbol complex displays clear interactions with cholesterol primarily via the amide hydrogen on Leu250. Additionally, simulations with the C1b domain bound to the bryostatin analogue Merle27 show predominant interactions between cholesterol and Trp252. However, the C1b-bryostatin complex does not exhibit any interactions between cholesterol and Leu250 or Trp252. Topological maps of the insertion depth and angle of orientation of the complexes in the membrane suggest that differences in these topological characteristics modulate the interactions with cholesterol, as well as differences in protein-ligand interactions. The lack of cholesterol interactions suggests that the bryostatin bound complex may not favorably translocate to cholesterol-rich domains in the cell, altering the substrate specificity of PKC-δ compared to the phorbol-bound complex.

5.2 Introduction

Protein Kinase C (PKC) belongs to a family of serine/threonine kinases and play an important role in cellular responses[1,2] involved in cell growth, proliferation and apoptosis, making them

therapeutic targets related to the eradication of HIV/AIDS, Alzheimer's treatment, and cancers[3–7]. Novel and conventional PKC's are activated endogenously by diacylglycerol. PKC-δ belongs to the novel class of PKC isoforms, which have a calcium-independent C2 domain. The C1 domain comprises the C1a and C1b regulatory domains and plays a predominant role in anchoring PKC to the plasma membrane through binding to ligands[8–10]. The ligand binding site is formed from two hydrophobic loops that form a hydrophilic pocket that interacts with the glycerol backbone of the native ligand, diacylglycerol. Ligand binding results in a hydrophobic surface that favors insertion into the membrane. Below this surface are 4 positively charged lysine residues that interact with negatively charged headgroups such as phosphatidylserine. For this reason, phosphatidylserine is a lipid whose presence is necessary for PKC-δ activation. The final third of the protein contains twin zinc finger motifs that are important for proper folding of the domain[11–13].

Cell membranes are bilayers composed primarily of phospholipids. Other lipids, such as sterols, ceramides, and sphingolipid, are also important for proper membrane function. Cholesterol is the most common sterol found in mammalian cells, and is crucial to cellular function through processes such as interactions with membrane proteins and the formation of lipid rafts[14–18]. Lipid rafts serve an important role in the cell membrane, controlling cell signaling through association with kinases and phosphatases and influencing the ability of intracellular pathogens to enter and exit the cell[19–21]. Cholesterol is also important for regulating membrane structure, thickness, and membrane fluidity. Through its effects on membrane characteristics, cholesterol can thus have an indirect effect on cellular signaling along with its direct effect through interactions with membrane proteins[18,22,23].

Two known exogenous modulators of PKC-δ are phorbol esters and bryostatin. Bryostatin and phorbol esters bind to the same region of the C1b regulatory domain as diacylglycerol and is

currently undergoing clinical trials as a potential therapeutic for the eradication of HIV/AIDS and as treatment for Alzheimer's[24–26]. Phorbol, on the other hand, binds to the same site of the C1b domain with the same affinity as bryostatin, yet is a well-known tumor promotor[27]. It is currently unknown why these two ligands with such similar binding characteristics result in such different cellular responses.

While recent studies have started to focus on the C1b domain's properties when bound to different modulators[28], little is known about how this domain interacts with its immediate membrane environment when bound to modulators such as phorbol and bryostatin. This study uses molecular dynamics simulations to explore the interactions between these different protein-ligand complexes and the surrounding membrane, looking specifically at differences in how these complexes interact with cholesterol. MD simulations are a useful tool for studying such protein/ligand/membrane interactions with atomistic detail. They can provide a strong foundation for the potential structure and dynamics of these complexes that could be observed within their natural environment. With the results detailed herein, a working hypothesis for why phorbol and bryostatin elicit such different cellular responses is posed, as well as several layers of experimental testing that can take place *in vitro* to validate the findings *in silico.*

5.3 Methods

5.3.1 Preparation of Protein-Ligand Complexes

5.3.1.1 C1b-Phorbol Complex

The crystal structure of the C1b regulatory domain of PKC-δ bound to phorbol 13-acetate was obtained from the RCSB Protein Data Bank (PDB ID: 1PTR). The Orientation of Proteins in Membranes (OPM) PPM server[29] was used for obtaining a structure with the initial orientation and insertion depth into a membrane and was saved as a PDB file. This structure was then used in the Membrane Builder module of the online CHARMM-GUI interface[30], which creates a pre-

equilibrated membrane around the inserted protein. A heterogeneous membrane bilayer with cholesterol (CHL1), phosphatidylethanolamine (POPE), phosphatidylcholine (POPC), phosphatidylserine (SOPS), phosphatidic acid (POPA), phosphatidylinositol (PLPI35), and sphingomyelin (CER160) was constructed with lipid composition shown in **Table 1**. A water height of 17 was used with the TIP3P water model, and a neutralizing amount of ions were added using the replacement method. Input files for GROMACS[31] were generated for use with the CHARMM36m[32] forcefield and a system temperature of 310.15 kelvin. This process was repeated for a total of 5 C1b/phorbol systems.

Membrane Component	Upper Leaflet Number	Lower Leaflet Number
Cholesterol	14	13
POPC	13	12
POPE	18	17
SOPS	8	7
POPA	2	1
PLPI35	4	3
CER160	7	6
Total	66	59

Table 1: Membrane composition for C1b-phorbol simulations. Lower leaflet numbers are slightly lower due to the presence of the inserted C1b-phorbol complex.

	Upper Leaflet Number	Lower Leaflet Number
Cholesterol	16	16
POPC	15	13
POPE	19	18
SOPS	8	8
POPA	3	2
PLPI35	5	4
CER160	7	6
Total	73	67

Table 2: Membrane composition for C1b-bryostatin- and C1b-Merle27 simulations. Lower leaflet numbers are slightly lower due to the presence of the inserted C1b-ligand complex.

5.3.1.2 C1b-Bryostatin and C1b-Merle 27 Complexes

As above, the crystal structure of the C1b regulatory domain of PKC-δ bound to phorbol 13-acetate was obtained (PDB ID: 1PTR). The ligand was removed using BIOVIA Discovery Studio Visualizer (BIOVIA (2020), Dassault Systemes, San Diego, CA). The bryostatin and Merle 27 structures were sketched as a mol2 files in BIOVIA Discovery Studio Visualizer. The AutoDock Tools package[33] was used to create pdbqt files of the protein and ligands. The size of the three-dimensional grid box for docking was set to 18, 26, 16 (x, y, z) and centered at 10.707, 21.52, 25.199 (x, y, z). The docking was performed using AutoDock Vina in Ubuntu 16.4 with

exhaustiveness = 10 and energy_range = 5 kcal/mol. From the resulting files, one structure exhibited the expected interaction between the C1 carbonyl on bryostatin/Merle 27 with Gly253. This structure was used, and the same steps outlined in section 5.3.1.1 were used to generate input files for GROMACS, with a membrane composition shown in **Table 2**. As with phorbol, this process was repeated for a total of 5 C1b-bryostatin and 5 C1b-Merle 27 systems. The RMSD between the post equilibration structures for the C1b-bryostatin and C1b-phorbol simulations was 0.398 Å, and 0.364 Å for the C1b-Merle27 and C1b-phorbol structures.

5.3.2 Molecular Dynamics Simulations

All 15 systems comprising the three C1b/ligand complexes were energy minimized, equilibrated, and simulated using the CHARMM36m forcefield with GROMACS. All systems were simulated out to 500 ns (2.5 microseconds total for each complex). Necessary residues of the C1b domain crystal structure were mutated to model human PKC. Cysteines involved in zinc ion coordination were deprotonated, and all other residues were protonated as dictated by their pKa values at pH 7.4. Zinc ions were restrained so that they remained coordinated within their zinc finger motifs with harmonic springs. A lack of restraints resulted in loss of coordination of the zinc ions with their respective residues. Energy minimization was completed with the steepest descent method for a maximum of 5000 steps. Equilibration for a total time of 1125 picoseconds with a pressure of 1 bar and reference temperature of 310.15 kelvin was carried out. All bonds with rigid hydrogen atoms were kept with the LINCS algorithm, and long-range electrostatic interactions were investigated with the particle-mesh Ewald algorithm. The production runs were carried out at 310.15 K with times steps of 2 femtoseconds.

5.3.3 Data Analysis

Data analysis was carried out using home written PYTHON code, including MDTraj[34] to read the trajectories into the code. Heat maps were obtained by tracking the x and y position of the oxygen

on cholesterol and the phosphate on the phosphatidylserine lipids in the lower leaflet housing the protein-ligand complexes. The same method was used for obtaining the average position of the backbone of the c1b domain. Visual Molecular Dynamics[35] was used to observe the structure and trajectories for each system.

5.4 Results and Discussion

Lipids play an important role in cellular signaling, especially through their interaction with membrane-associated proteins[17,23] and the formation of membrane microdomains[18,21]. Partitioning of proteins into and out of microdomains such as lipid rafts is a key regulatory mechanism for a number of receptor complexes such as T-cell receptors, EGF receptors, and H-Ras receptors[36–39]. As such, interactions between the PKC-δ C1b domain and membrane lipids such as phosphatidylserine (SOPS) and cholesterol could dictate the cellular response after the binding of a modulator such as phorbol esters or bryostatin and its analogues.

5.4.1 C1b-Phorbol and C1b-Bryostatin Interactions with SOPS Lipids

Phosphatidylserine is known to be an important lipid in the activation of PKC-δ[40,41]. Its negatively charged phosphate headgroup stabilizes the C1b domain in the membrane through interacting with positively charged lysine residues in the middle third of the C1b domain around the surface of the membrane. To validate (preliminarily) the MD simulations presented, interactions between SOPS and lysine residues of PKC-δ were investigated. **Figure 1A-E** shows heatmaps of the phosphatidylserine headgroups in each of the 5 simulations with the C1b domain bound to phorbol.

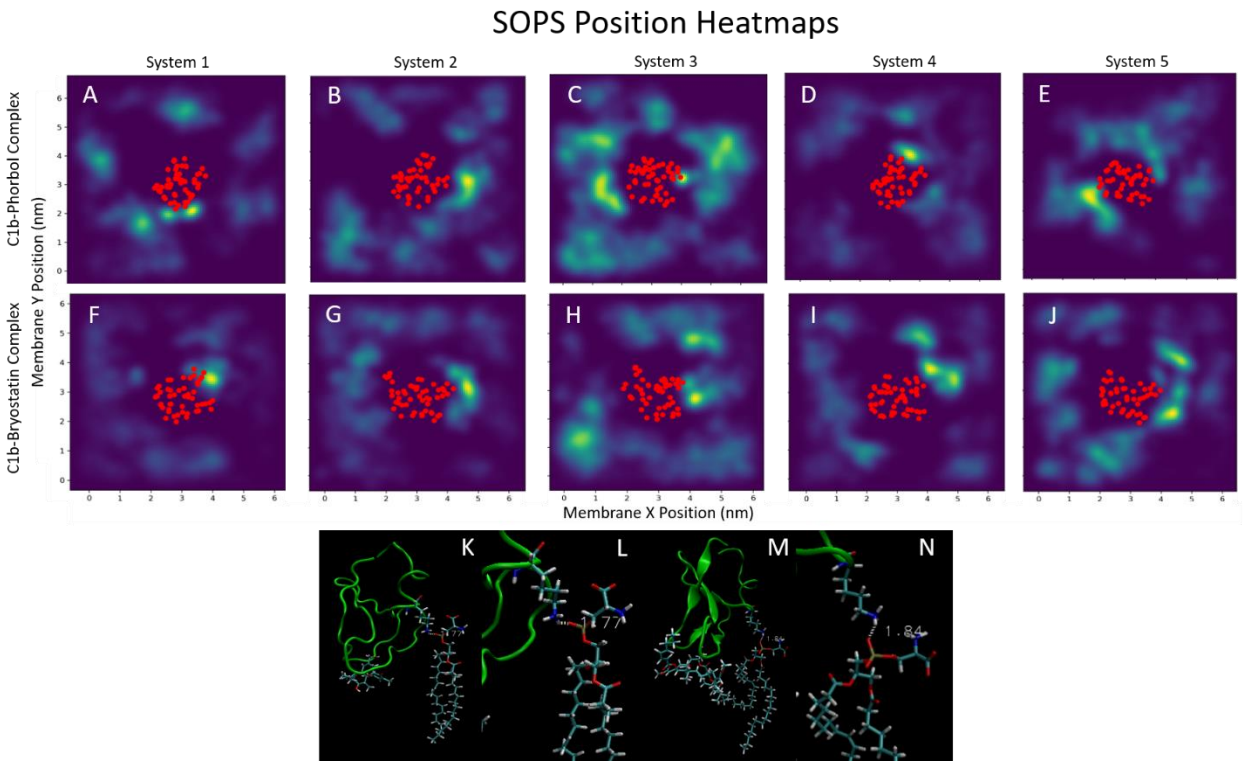

Figure 1: Heatmaps of SOPS lipid positions in each of the 10 total C1b-phorbol (A-E) and C1b-bryostatin (F-G) simulations. Areas of high intensity are regions frequented by the SOPS lipids. Red dots represent the average position of each backbone residue on the C1b domain. Also shown are representative SOPS-Lysine interactions from the C1b-phobol (K,L) and C1b-bryostatin (M,N) simulations.

Figure 1 shows prolonged interactions between SOPS and PKC in both the C1b-phorbol and C1b-bryostatin simulations. Similar regions around the protein-ligand complexes are more likely to be occupied by SOPS lipids. In particular, inspection of the PKC structures revealed extension of the Lys271 side chain out towards the bilayer and interacting with SOPS head groups. In C1b-phorbol, system 5, for example, interactions between Lys271 and SOPS headgroups lasted for over 300 ns of the 500ns simulation (cutoff between Lys271 amine nitrogen and SOPS phosphorus of < 6Å). These regions around the protein favored by SOPS lipids are areas where lysine side chains extend

out from the protein, forming interactions with the SOPS lipids, an example of which can be seen in **Figure 1K-N** for each C1b-ligand complex.

5.4.2 C1b-Phorbol and C1b-Bryostatin Interactions with Cholesterol

Cholesterol is an important cellular signaling membrane lipid in cells[14–18,22]. In T-cells, PKC is known to translocate toward lipid rafts, which are cholesterol rich regions in the cell, resulting in cytokine production[42]. Furthermore, studies with the native ligand diacylglycerol suggests a role for ligand-cholesterol interactions in amplifying the activity of PKC[43]. Thus, it is likely that interactions with cholesterol could play a major role in regulating cellular responses following PKC activation with different modulators. **Figure 2A-E** shows heat maps of cholesterol positions in all 5 simulations of the C1b domain bound to phorbol.

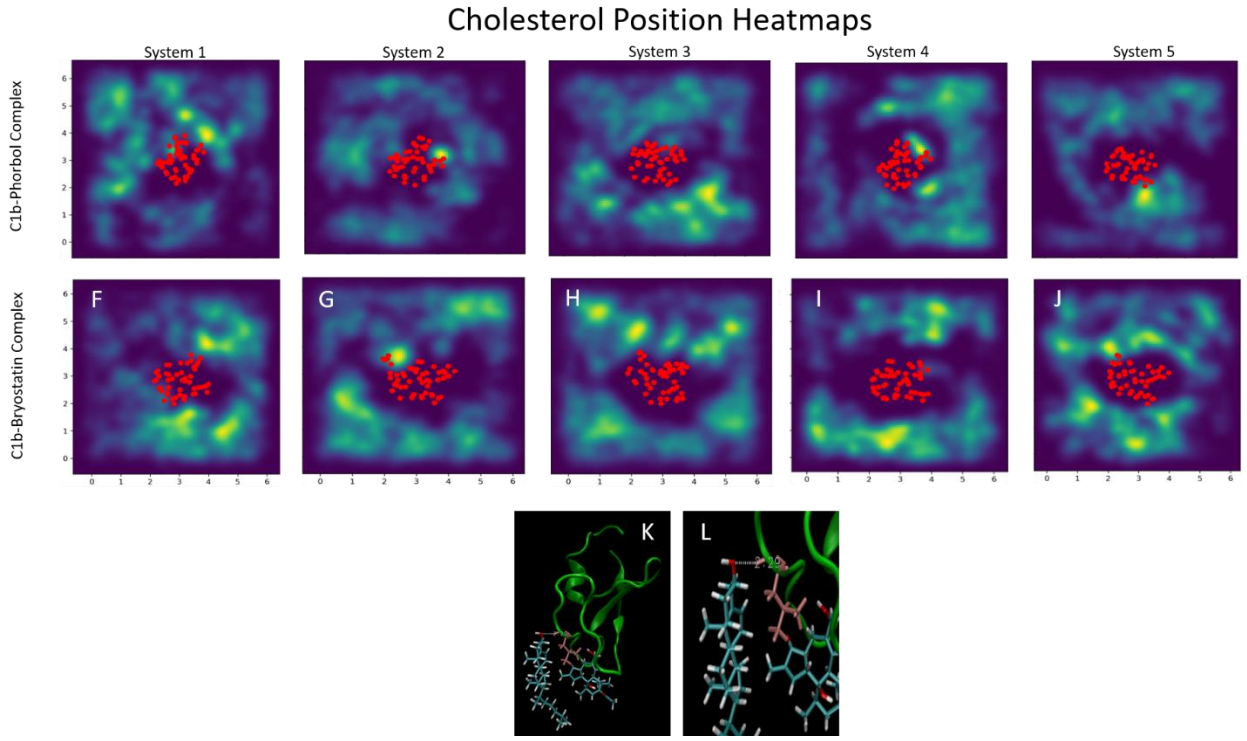

Figure 2: Heatmaps of Cholesterol positions in each of the 10 total C1b-phorbol (A-E) and C1b-bryostatin (F-G) simulations. Areas of high intensity are regions frequented by cholesterol. Red

dots represent the average position of each backbone residue on the C1b domain. Also shown are representative Leu250-cholestrol interactions from the C1b-phobol simulations (K,L).

The heatmaps shown in **Figure 2** indicate that L250 forms a stable interaction between the backbone N-H proton of L250 and the cholesterol hydroxyl (**Figure 2K,L**). Across all 5 C1b-phorbol simulations, L250-cholesterol interactions were present for over 1 microsecond of the total 2.5 microseconds of simulation (over 40% of the total simulation time, cutoff < 3Å).

Contrarily, in the 5 simulations of the C1b domain bound to bryostatin, this Leu250-cholesterol interaction is not present (cutoff < 3Å). **Figure 2F-J** shows positional heatmaps of the cholesterol lipids in the 5 bryostatin-bound simulations. Simulations 2 and 5 for the C1b-brysostatin complex (**Figure 2G and Figure 2J**, respectively) do indicate an increased presence of cholesterol near what is the C-terminal end of the C1b domain. Inspection of the trajectories revealed that this is not the case. In the heatmap's 2D format, there appears to be an interaction, but in 3D these interactions do not exist. Manual inspection of the simulations revealed L250 to not be inserted into the membrane, thus precluding interaction with cholesterol.

To assess this hypothesis, topological heat maps were generated to determine the average insertion depth and tilt angle of the PKC-ligand complexes. **Figure 3** shows the C1b domain inserts deeper into the membrane when bound to phorbol, averaging about a 7 Å insertion depth compared to 5 Å when bound to bryostatin and is oriented at a slightly different angle. The effect that this change in topology has on the positioning of the Leu250 residue with respect to the cholesterol headgroups is shown in **Figure 4**.

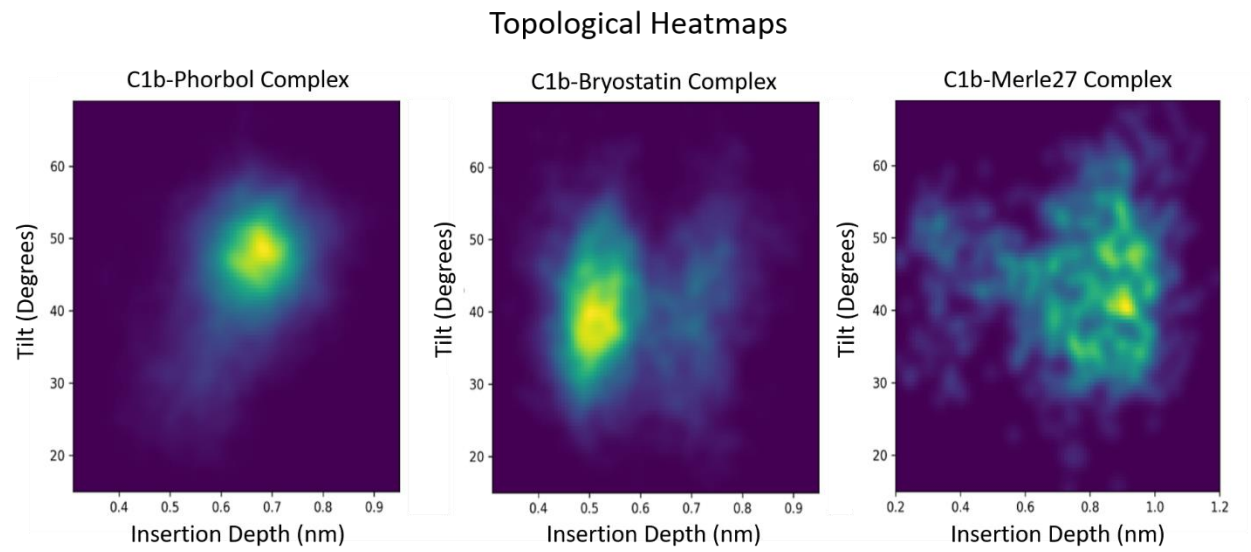

Figure 3: Topological heatmaps of the insertion depth and angle of orientation of the C1b-ligand complexes for C1b-phorbol (left) and C1b-bryostatin (right). Each heatmap is an average for all 5 simulations for each complex. Areas of greater intensity represent topologies more frequently found in each simulation.

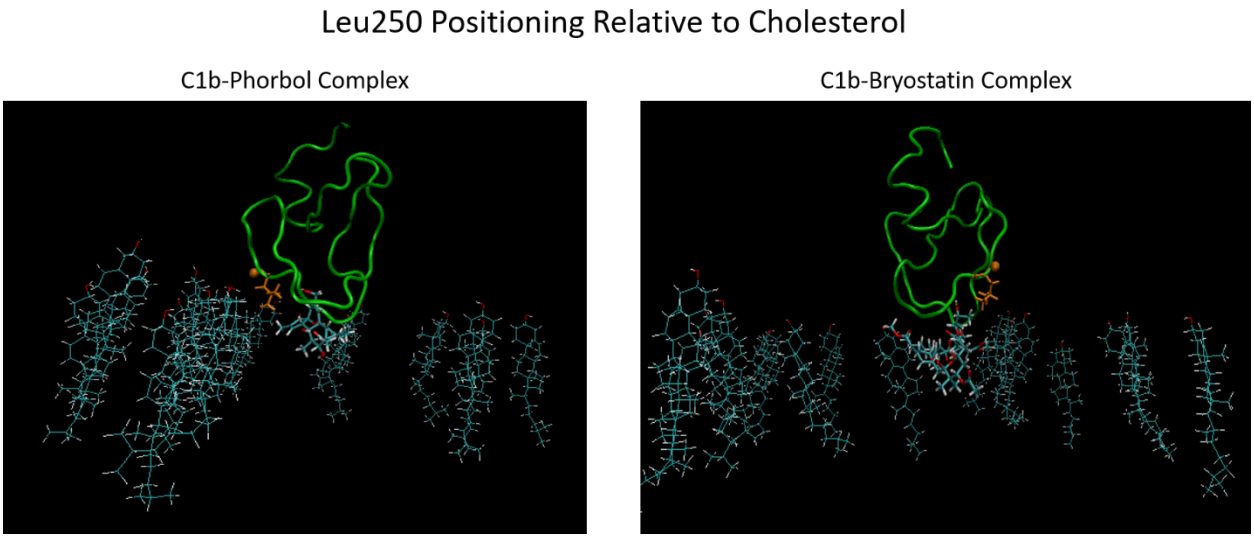

Figure 4: Images showing the positioning of the Leu250 residue (orange in both figures) relative to the cholesterol headgroups in a C1b-phorbol (left) simulation and C1b-bryostatin (right) simulation. The N-H hydrogen is drawn is pictured as an orange sphere on Leu250.

When inserted deep enough into the membrane, as is the case for the C1b-phorbol complex, the Leu250 residue on the C1b domain is free to interact with the surrounding cholesterol lipids. However, the C1b domain when bound to bryostatin is inserted too shallowly in the membrane for these interactions to occur. Mutation of Leu250 to glycine is known to result in abrogated activity of PKC, due potentially to reduced lipid interactions[44]. Thus, the shallower binding mode elicited by the bryostatin-bound complex may have an important role in dictating the potential interactions PKC-δ has with surrounding lipids and its inclusion or exclusion from lipid rafts. Since the C1b domain is the primary determinant of membrane association of the novel class of PKC's[8,9,40], this could influence the cellular localization of the protein.

5.4.3 C1b-Merle27 Simulations

To further investigate this hypothesis, MD simulations were performed on the C1b domain when bound to a bryostatin analogue known as Merle27. Merle27 is a bryostatin analogue that is known to elicit cellular responses that are more similar to those initiated by phorbol, rather than bryostatin[45]. Again, as a preliminary validation tool, interactions between the C1b domain and SOPS lipids were investigated (**Figure 5**). As expected, interactions between SOPS and the lysine residues was observed (**Figure 5F,**G). Indeed, when comparing the topological heatmaps of the C1b-ligand complexes in **Figure 3**, the membrane insertion of C1b-Merle27 complex is more similar to that of phorbol than bryostatin, as it inserts more deeply into the membrane. However, the cholesterol heatmaps shown in **Figure 6** show that the C1b-Merle27 complex does not exhibit as much of a propensity to interact with cholesterol through the Leu250 residue (interactions for

less than 15%, cutoff 3Å) but there is a significant C1b-cholesterol interaction that forms through Trp252 (20%, cutoff 3Å).

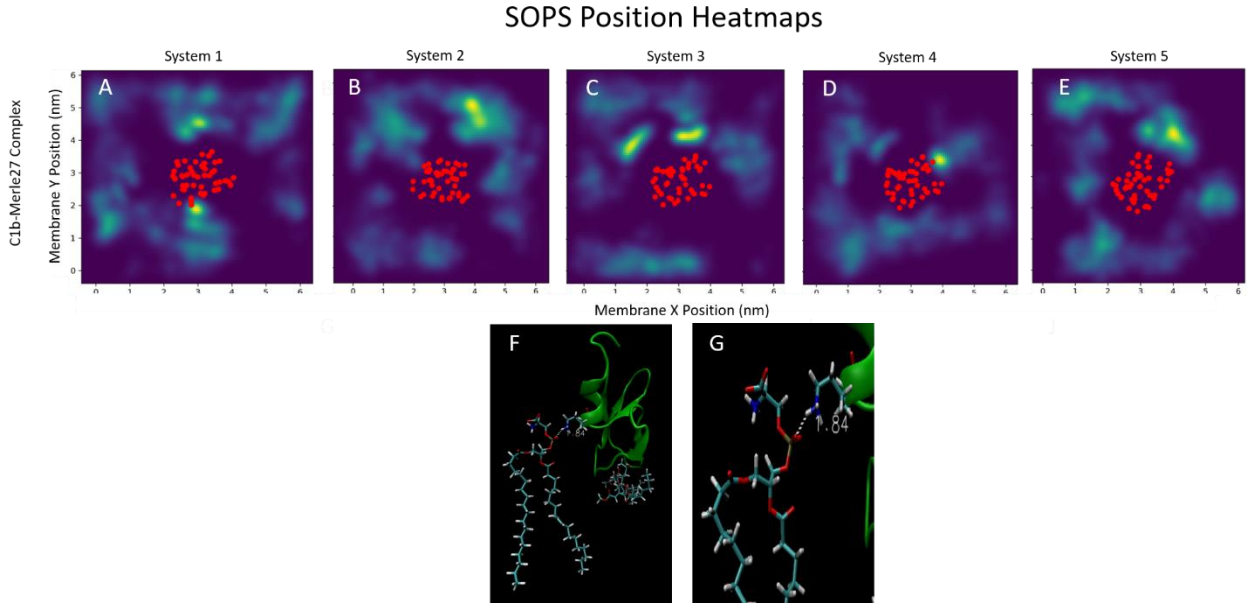

Figure 5: Heatmaps of SOPS positions in each of the 5 C1b-Merle27 simulations (A-E). Areas of higher intensity represent areas more frequently occupied by SOPS lipids. Red dots represent the average position of each backbone residue on the C1b domain. Also shown are representative SOPS-Lysine interactions from the C1b-Merle27 simulations (F,G).

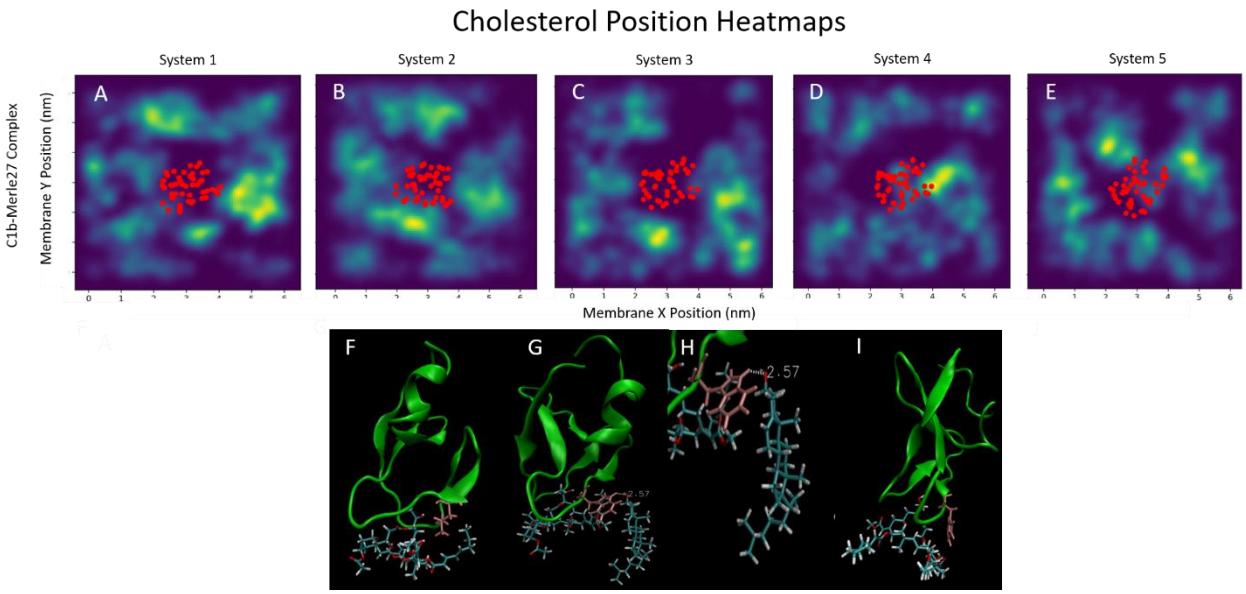

Figure 6: Heatmaps of cholesterol positions in each of the 5 C1b-Merle27 simulations (A-E). Areas of higher intensity represent areas more frequently occupied by cholesterol. Red dots represent the average position of each backbone residue on the C1b domain. Also shown is an image of the acyl chain of Merle27 extending out to Leu250, in pink (F), a representative interaction between Trp252, in pink, and cholesterol in the C1b-Merle27 simulations (G,H), and an image Trp252, in pink, interacting with bryostatin in the C1b-bryostatin simulations (I).

The acyl chain on Merle 27 extends out near Leu250, sterically hindering access of cholesterol to this residue. Thus, interactions between Leu250 and cholesterol were reduced, but still present. There were instances where the acyl chain on cholesterol interacted with the acyl chain on Merle27, but this was not a common interaction found in the simulations. Interestingly, another hotspot for cholesterol appears to involve residue Trp252 (**Figure 6G,H**).

In the C1b-Merle27 simulations, the Trp252 sidechain extends away from the ligand, enabling it to interact with nearby cholesterol lipids. In the C1b-bryostatin simulations, however, it can be seen that the indole nitrogen of Trp252 is turned in toward bryostatin, stabilizing the protein-ligand

complex (**Figure 6I**). This makes the Trp252 side chain unavailable for interactions with cholesterol.

These simulations suggest that interactions between the C1b domain and cholesterol could play an important role in influencing the cellular responses elicited from different modulators. The C1b-phorbol and C1b-Merle27 complexes exhibit consistent predominant interactions with cholesterol through Leu250 and Trp252, respectively. Through changes in topology and differences in protein-ligand interactions, these cholesterol interactions are not present in the C1b-bryostatin simulations. The lack of cholesterol interactions may serve a critical role in modulating the cellular localization of PKC, thus having an effect on which substrates are accessible to the kinase. This could have a profound impact on which cellular responses are triggered through modulators binding to the C1b domain.

5.5 Conclusions and Outlook

Through molecular dynamics simulations, a reasonable hypothesis can be proposed for why bryostatin and phorbol elicit different cellular effects within the cell. Namely, that cholesterol interactions with the C1b domain drive the cellular localization of the protein, affecting the substrate specificity of PKC. Through topological changes and variations in protein-ligand interactions, the C1b domain displays a significant decrease in cholesterol interactions when bound to bryostatin when compared to the C1b-phorbol and C1b-Merle27 complexes. This decrease in the C1b domain's interactions with cholesterol when bound to byrostatin could affect its likelihood of translocating to cholesterol-rich regions of the cell membrane, such as lipid rafts, which will alter which substrates have accessibility to the active site of PKC-δ.

With this working hypothesis, *in vitro* solid-state NMR experiments can be performed to verify whether or not these characteristics are likely to persist in a cellular membrane. By introducing

^{17}O-labelled cholesterol into the phosphatidylserine lipid vesicles, interactions between the cholesterol and a singly labelled ^{15}N-Leu250 or ^{15}N-Trp252 residue can be explored and quantified. Furthermore, selective labelling on bryostatin and these same residues on the C1b domain can also be used to determine if the bound conformation of bryostatin does inhibit cholesterol interactions with those residues on the protein. While labelling cholesterol with ^{17}O would be ideal, experiments performed with ^{13}C or ^{19}F labelled cholesterol may be more tractable for initial experiments.

If the *in vitro* results support the hypothesis derived from the molecular dynamics simulations, it would ultimately be beneficial to confirm them with in-cell DNP. Ffurther improvements upon the sensitivity enhancements produced in chapters 2-4 will make these experiments more tractable. Improvements can be made through a combination of increasing microwave power, improving microwave coupling to the sample in the NMR rotor, and optimizing microwave polarization. These examples are outlined in more detail in Chapter 6.

Author Contributions:

- Planning and direction of molecular dynamics simulations was a collaboration between Patrick Judge, Sarah Overall, and Alexander Barnes
- Analysis of simulations was performed by Patrick Judge
- Chapter was written and compiled by Patrick Judge

5.6 References

1. Nishizuka Y. Protein kinase C and lipid signaling for sustained cellular responses. *FASEB J.* 1995;9(7):484-496. doi:10.1096/fasebj.9.7.7737456

2. Takai Y, Kishimoto A, Kikkawa U, Mori T, Nishizuka Y. Unsaturated diacylglycerol as a possible messenger for the activation of calcium-activated, phospholipid-dependent protein kinase system. *Biochem Biophys Res Commun*. 1979;91(4):1218-1224. doi:10.1016/0006-

291X(79)91197-5

3. Wender PA, Kee J-M, Warrington JM. Practical Synthesis of Prostratin, DPP, and Their Analogs, Adjuvant Leads Against Latent HIV. *Science (80-)*. 2008;320(5876):649-652. doi:10.1126/science.1154690.Practical

4. DeChristopher BA, Loy BA, Marsden MD, Schrier AJ, Zack JA, Wender PA. Designed, Synthetially Accessible Bryostatin Analogues Potently Induce Activation of Latent HIV Reservoirs in vitro. *Nat Chem*. 2012;4:705-710. doi:10.1038/nchem.1395.Designed

5. Mehla R, Bivalkar-Mehla S, Zhang R, et al. Bryostatin modulates latent HIV-1 infection via PKC and AMPK signaling but inhibits acute infection in a receptor independent manner. *PLoS One*. 2010;5(6). doi:10.1371/journal.pone.0011160

6. Alkon DL, Sun MK, Nelson TJ. PKC signaling deficits: a mechanistic hypothesis for the origins of Alzheimer's disease. *Trends Pharmacol Sci*. 2007;28(2):51-60. doi:10.1016/j.tips.2006.12.002

7. Khan TK, Nelson TJ, Verma VA, Wender PA, Alkon DL. A cellular model of Alzheimer's disease therapeutic efficacy: PKC activation reverses Aβ-induced biomarker abnormality on cultured fibroblasts. *Neurobiol Dis*. 2009;34(2):332-339. doi:10.1016/j.nbd.2009.02.003

8. Stahelin R V., Wang J, Blatner NR, Rafter JD, Murray D, Cho W. The origin of C1A-C2 interdomain interactions in protein kinase Cα. *J Biol Chem*. 2005;280(43):36452-36463. doi:10.1074/jbc.M506224200

9. Giorgione JR, Lin JH, McCammon JA, Newton AC. Increased membrane affinity of the C1 domain of protein kinase Cδ compensates for the lack of involvement of its C2 domain in membrane recruitment. *J Biol Chem*. 2006;281(3):1660-1669. doi:10.1074/jbc.M510251200

10. Stahelin R V., Digman MA, Medkova M, et al. Mechanism of diacylglycerol-induced membrane targeting and activation of protein kinase Cδ. *J Biol Chem*. 2004;279(28):29501-29512. doi:10.1074/jbc.M403191200

11. Xu RX, Pawelczyk T, Xia TH, Brown SC. NMR structure of a protein kinase C-γ phorbol-binding domain and study of protein-lipid micelle interactions. *Biochemistry*. 1997;36(35):10709-10717. doi:10.1021/bi970833a

12. Zhang G, Kazanietz MG, Blumberg PM, Hurley JH. Crystal structure of the Cys2 activator-binding domain of protein kinase Cδ in complex with phorbol ester. *Cell*. 1995;81(6):917-924. doi:10.1016/0092-8674(95)90011-X

13. Hommel U, Zurini M, Luyten M. Solution structure of a cysteine rich domain of rat protein kinase C. *Nat Struct Biol*. 1994;1(6):383-387. doi:10.1038/nsb0694-383

14. Ohvo-Rekilä H, Ramstedt B, Leppimäki P, Peter Slotte J. Cholesterol interactions with phospholipids in membranes. *Prog Lipid Res*. 2002;41(1):66-97. doi:10.1016/S0163-

7827(01)00020-0

15. Epand RM. Cholesterol and the interaction of proteins with membrane domains. *Prog Lipid Res*. 2006;45(4):279-294. doi:10.1016/j.plipres.2006.02.001

16. PE K, M L. The sterol-sensing domain: multiple families, a unique role? *Trends Genet*. 2002;18(4):193-201. http://www.wormbase.org/db/misc/paper?name=WBPaper00005195.

17. Incardona JP, Eaton S. Cholesterol in signal transduction. *Curr Opin Cell Biol*. 2000;12(2):193-203. doi:10.1016/S0955-0674(99)00076-9

18. Edidin M. The state of lipid rafts: From model membranes to cells. *Annu Rev Biophys Biomol Struct*. 2003;32:257-283. doi:10.1146/annurev.biophys.32.110601.142439

19. Kabouridis PS, Janzen J, Magee AL, Ley SC. Cholesterol depletion disrupts lipid rafts and modulates the activity of multiple signaling pathways in T lymphocytes. *Eur J Immunol*. 2000;30(3):954-963. doi:10.1002/1521-4141(200003)30:3<954::AID-IMMU954>3.0.CO;2-Y

20. Simons K, Toomre D. Lipid Rafts and Signal transduction. *Nat Rev Mol Cell Biol*. 2000;1:31-41.

21. Van Der Goot FG, Harder T. Raft membrane domains: From a liquid-ordered membrane phase to a site of pathogen attack. *Semin Immunol*. 2001;13(2):89-97. doi:10.1006/smim.2000.0300

22. Lundbæk JA, Andersen OS, Werge T, Nielsen C. Cholesterol-induced protein sorting: An analysis of energetic feasibility. *Biophys J*. 2003;84(3):2080-2089. doi:10.1016/S0006-3495(03)75015-2

23. Mcintosh T, Simon S. Roles of bilayer material properties in function and distribution of membrane properties. Annu. Rev. Biophys. Biomolec. Struct. 35, 177-198. *Annu Rev Biophys Biomol Struct*. 2006;35:177-198. doi:10.1146/annurev.biophys.35.040405.102022

24. Pettit GR, Herald CL, Doubek DL, Herald DL, Arnold E, Clardy J. Isolation and Structure of Bryostatin 1. *J Am Chem Soc*. 1982;104(24):6846-6848. doi:10.1021/ja00388a092

25. PETTIT GR, DAY JF, HARTWELL JL, WOOD HB. Antineoplastic Components of Marine Animals. *Nature*. 1970;227(5261):962-963. doi:10.1038/227962a0

26. Wender PA, Hardman CT, Ho S, et al. Scalable synthesis of bryostatin 1 and analogs, adjuvant leads against latent HIV. *Science (80-)*. 2017;358(6360):218-223. doi:10.1126/science.aan7969

27. Nishizuka Y. The role of protein kinase C in cell surface signal transduction and tumour promotion. *Nature*. 1984;308(5961):693-698. doi:10.1038/308693a0

28. Ryckbosch SM, Wender PA, Pande VS. Molecular dynamics simulations reveal ligand-

controlled positioning of a peripheral protein complex in membranes. *Nat Commun*. 2017;8(1):6. doi:10.1038/s41467-016-0015-8

29. Lomize MA, Pogozheva ID, Joo H, Mosberg HI, Lomize AL. OPM database and PPM web server: Resources for positioning of proteins in membranes. *Nucleic Acids Res*. 2012;40(D1):370-376. doi:10.1093/nar/gkr703

30. Jo S, Kim T, Iyer VG, Im W. A Graphical User Interface for Computational Chemistry Softwares. *J Comput Chem*. 2008;29:1859-1865. doi:10.1002/jcc

31. Brooks BR, Brooks III CL, Mackerell Jr. AD, et al. CHARMM: The Biomolecular Simulation Program B. *J Comput Chem*. 2009;30:1545-1614. doi:10.1002/jcc

32. Lee J, Cheng X, Swails JM, et al. CHARMM-GUI Input Generator for NAMD, GROMACS, AMBER, OpenMM, and CHARMM/OpenMM Simulations Using the CHARMM36 Additive Force Field. *J Chem Theory Comput*. 2016;12(1):405-413. doi:10.1021/acs.jctc.5b00935

33. Sanner MF. Python: a programming language for software integration and development. *J Mol Graph Model*. 1999;17(1):57-61.

34. McGibbon RT, Beauchamp KA, Harrigan MP, et al. MDTraj: A Modern Open Library for the Analysis of Molecular Dynamics Trajectories. *Biophys J*. 2015;109(8):1528-1532. doi:10.1016/j.bpj.2015.08.015

35. Frishman D, Argos P. Knowledge-based protein secondary structure assignment. *Proteins Struct Funct Genet*. 1995;23:566-579.

36. Janes PW, Ley SC, Magee AI, Kabouridis PS. The role of lipid rafts in T cell antigen receptor (TCR) signalling. *Semin Immunol*. 2000;12(1):23-34. doi:10.1006/smim.2000.0204

37. Langlet C, Bernard AM, Drevot P, He HT. Membrane rafts and signaling by the multichain immune recognition receptors. *Curr Opin Immunol*. 2000;12(3):250-255. doi:10.1016/S0952-7915(00)00084-4

38. Waugh MG, Lawson D, Hsuan JJ. Epidermal growth factor receptor activation is localized within low-buoyant density, non-caveolar membrane domains. *Biochem Soc*. 1999;597(337):591-597.

39. Roy S, Luetterforst R, Harding A, et al. Dominant-negative caveolin inhibits H-Ras function by disrupting cholesterol-rich plasma membrane domains. *Nat Cell Biol*. 1999;1(2):98-105. doi:10.1038/10067

40. Stahelin R V., Digman MA, Medkova M, et al. Mechanism of diacylglycerol-induced membrane targeting and activation of protein kinase Cδ. *J Biol Chem*. 2004;279(28):29501-29512. doi:10.1074/jbc.M403191200

41. Medkova M, Cho W. Differential membrane-binding and activation mechanisms of protein kinase C-α and -ε. *Biochemistry*. 1998;37(14):4892-4900. doi:10.1021/bi972495j

42. Bi K, Tanaka Y, Coudronniere N, et al. Antigen-induced translocation of PKC-θ to membrane rafts is required for T cell activation. *Nat Immunol*. 2001;2(6):556-563. doi:10.1038/88765

43. Armstrong D, Zidovetzki R. Amplification of diacylglycerol activation of protein kinase C by cholesterol. *Biophys J*. 2008;94(12):4700-4710. doi:10.1529/biophysj.107.121426

44. Kazanietz MG, Wang S, Milne GWA, Lewin NE, Liu HL, Blumberg PM. Residues in the second cysteine-rich region of protein kinase C δ relevant to phorbol ester binding as revealed by site-directed mutagenesis. *J Biol Chem*. 1995;270(37):21852-21859. doi:10.1074/jbc.270.37.21852

45. Keck GE, Li W, Kraft MB, Kedei N, Lewin NE, Blumberg PM. The bryostatin 1 A-ring acetate is not the critical determinant for antagonism of phorbol ester-induced biological responses. *Org Lett*. 2009;11(11):2277-2280. doi:10.1021/ol900585t

Chapter 6: Conclusions and Future Outlook

6.1 Conclusions for Increasing DNP NMR Sensitivity

Chapters 2 through 4 form a foundation for improving the sensitivity of DNP NMR for both solid effect and cross effect radicals to be applied in human cells. It is shown that lowering the sample temperature from 90 K to below 6 K improved the sensitivity of trityl Finland radical by a factor of 3.2x. At 6 K trityl outperformed TEMTriPol-1 and AMUPol by factors of 6x and 1.9x, respectively, indicating that the ability to access temperatures below 6 K will be important for performing highly sensitive NMR experiments in the future[1]. Electron decoupling is shown to be effective in cellular environments, including intact human cells, enabling the decoupling of hyperfine interactions between electrons and nuclei to improve the sensitivity and resolution of the NMR signal[2,3]. Further, frequency-chirped DNP is shown to be more sensitive than conventional continuous wave DNP methods and is proven to be effective in human cell lines[4,5]. The improved sensitivity of solid effect and cross effect radicals opens many avenues for performing ultra-sensitive DNP NMR on samples in their biologically natural environment in cells.

6.2 Conclusions for Molecular Dynamics Simulations of the C1b Domain Bound to Modulating Ligands

Through molecular dynamics simulations in Chapter 5, it is hypothesized that, when bound to the C1b domain, bryostatin prevents interactions between cholesterol and the Leu250 and Trp252 residues on the PKC-d C1b regulatory domain. When bound to phorbol, the C1b domain is free to interact with nearby cholesterol molecules predominately through Leu250, with some cholesterol interactions observed through Trp252. The byrolog Merle27, which is structurally similar to bryostatin yet elicits cellular effects more similar to phorbol, also exhibits a propensity to interact with cholesterol. These interactions are predominately found with Trp252, with some

interactions still observed with Leu250. This difference in interaction propensity is expected to play a role in modulating the cellular localization of PKC-δ, thus having an effect on which substrates are available to be phosphorylated by PKC-δ's kinase domain.

6.3 Future Outlook

While these sensitivity improvements are an important step toward in-cell DNP NMR, further advances can yet be made to improve sensitivity for the study of PKC-δ in intact human cells. The most direct method for making these improvements is to increase the microwave power incident on the NMR sample. Higher microwave powers will enable the transfers of electron spin polarization to the nuclei on a timescale shorter than the electron relaxation time.

One indirect method for increasing microwave power is taking advantage of the polarization of the microwaves. Generally, applied microwaves are linearly polarized, which can be represented as a superposition of left and right circularly polarized components. The only component that is absorbed is that which shares the chirality of the spin's precession. It is possible to convert the other polarization component to the proper chirality, which would double the microwave power absorbed by the sample.

In order to be able to implement this strategy of altering the polarization of the microwaves, it will be necessary to use recently implemented MAS spheres with a saddle coil[6]. The saddle coil is not conducive to sensitive NMR with conventional MAS stators using solenoids, but the spheres stators developed in our lab can take advantage of the ample space provided by the saddle coil to allow the circularly polarized microwaves to enter the sample unimpeded. The unimpeded microwave access to the sphere also allows the addition of a Teflon lens to focus the microwaves to further improve the utilized microwave power.

With current and future improvements made in microwave power, experiments can be performed on PKC *in vitro* and *in vivo* to determine the extent of cholesterol interactions for each protein-ligand complex observed *in silico*. One important step is to incorporate DNP polarizing agents into membrane systems. An elegant method would be to covalently attach a polarizing agent to the N-terminus of the C1b domain via solid phase peptide synthesis. This improves DNP sensitivity in non-glassy membranes and ensures that the radical is close to the target. Tethering of the trityl-Me_3N radical would enable some of the most sensitive DNP NMR experiments to date while allowing for the decoupling of the electron-nuclear hyperfine interactions. Initially, selectively labeling Leu250, Trp252, and cholesterol can be useful for confirming the interactions between C1b domain and cholesterol *in vitro*. Similarly, this can be used to rule out interactions between these residues and cholesterol when the C1b domain is bound to bryostatin. Observing ^{15}N chemical shift anisotropies has been shown to be an effective method for determining the presence of a hydrogen bond and could be applied to this system[7]. Confirming these results *in vitro* will be another preliminary step toward studying PKC-δ in intact human cells with DNP NMR.

6.4 References

1. Judge PT, Sesti EL, Saliba EP, et al. Sensitivity analysis of magic angle spinning dynamic nuclear polarization below 6 K. *J Magn Reson*. 2019;305:51-57. doi:10.1016/j.jmr.2019.05.011
2. Sesti EL, Saliba EP, Alaniva N, Barnes AB. Electron decoupling with cross polarization and dynamic nuclear polarization below 6 K. *J Magn Reson*. 2018;295:1-5. doi:10.1016/j.jmr.2018.07.016
3. Judge PT, Sesti EL, Price LE, et al. Dynamic Nuclear Polarization with Electron Decoupling in Intact Human Cells and Cell Lysates. *J Phys Chem B*. 2020;124(12). doi:10.1021/acs.jpcb.9b10494
4. Gao C, Alaniva N, Saliba EP, et al. Frequency-chirped dynamic nuclear polarization with magic angle spinning using a frequency-agile gyrotron. *J Magn Reson*. 2019;308.

doi:10.1016/j.jmr.2019.106586

5. Judge PT, Sesti EL, Alaniva N, et al. Characterization of frequency-chirped dynamic nuclear polarization in rotating solids. *J Magn Reson*. 2020;313. doi:10.1016/j.jmr.2020.106702

6. Gao C, Judge PT, Sesti EL, et al. Four millimeter spherical rotors spinning at 28 kHz with double-saddle coils for cross polarization NMR. *J Magn Reson*. 2019;303. doi:10.1016/j.jmr.2019.03.006

7. Yao L, Grishaev A, Cornilescu G, el al. The Impact of Hydrogen bonding on Amide ^{1}H Chemical Shift Anisotropy Studies by Cross-Correlated RElaxation and LIquid Crystal NMR Spectroscopy. *JACS* 2010;132;10866 doi:10.1021/ja103629e